

## **General Disclaimer**

### **One or more of the Following Statements may affect this Document**

- This document has been reproduced from the best copy furnished by the organizational source. It is being released in the interest of making available as much information as possible.
- This document may contain data, which exceeds the sheet parameters. It was furnished in this condition by the organizational source and is the best copy available.
- This document may contain tone-on-tone or color graphs, charts and/or pictures, which have been reproduced in black and white.
- This document is paginated as submitted by the original source.
- Portions of this document are not fully legible due to the historical nature of some of the material. However, it is the best reproduction available from the original submission.

Final Report  
Mission Definition Study for a VLBI Station  
Utilizing the Space Shuttle

NAS-5-25543

Professor Bernard F. Burke    October 12, 1982

Final Report

on the

Mission Definition Study for a VLBI Station

Utilizing the Space Shuttle

under NAS-5-25543

Submitted by the

Center for Space Research  
Massachusetts Institute of Technology  
Cambridge, MA 02139

Professor B. Burke, Principal Investigator  
R. Doxsey  
D. Roberts  
L. Bannister  
J. Binsack

GSFC Technical Officer:  
Dr. T. Clark, Code 693

12 October 1982

Final Report

VLBI - UTILIZING THE SPACE SHUTTLE

NASA Contract NAS-5-25543

October 12, 1982

The uses of the Space Shuttle transportation system for orbiting Very-Long-Baseline Interferometry (OVLBI) have been examined, both with respect to technical feasibility and its scientific possibilities. The study consisted of a critical look at the adaptability of current technology to an orbiting environment, the suitability of current data reduction facilities for the new technique, and a review of the new science that is made possible by using the Space Shuttle as a moving platform for a VLBI terminal in space. The conclusions are positive in all respects: no technological deficiencies exist that would need remedy, the data processing problem can be handled easily by straightforward adaptations of existing systems, and there is a significant new research frontier to be explored, with the Space Shuttle providing the first step.

The VLBI technique utilizes the great frequency stability of modern atomic time standards, the power of integrated circuitry to perform real-time signal conditioning, and the ability of magnetic tape recorders to provide essentially error-free data recording, all of which combine to permit the realization of radio interferometry at arbitrarily large baselines. This has permitted ground-based radio observers to achieve angular resolution a thousand times greater than that achieved by Optical astronomy, and has revealed a wide variety of interesting phenomena. The size of the Earth is a fundamental limitation and the use of an orbiting radio telescope allows

one to pass beyond this barrier. Chapter II gives an overview of the method.

The specific advantages of VLBI in space are given in Chapter III. Simulations of OVLBI with various choices of near-Earth orbits are given in Chapter IV.

A single antenna in near-Earth orbit can be used in conjunction with ground-based radio telescopes in the simplest realization of OVLBI configurations. This is the mode in which the Space Shuttle would be used. There is, however, a strong impetus to place antennas in much larger orbits, and these possibilities are examined in Chapter V.

A critical examination of OVLBI must examine the effects of orbital perturbations, precession, and decay. These problems are examined in Chapter VI, in which it is shown that all such perturbations can be corrected for. The question of the best orbit for OVLBI applications can be formulated, and the results are discussed in Chapter VII. It turns out that the common shuttle orbit with an orbital inclination of  $57^\circ$  is close to the optimum choice.

The state of technical readiness of present VLBI data acquisition, handling, and processing systems is discussed in some detail in Chapter VIII. The conclusions are favorable: the requirements of OVLBI can be met by straightforward adaptations of existing systems.

The state of technical readiness, and the intense scientific interest of the potential subjects of research lead to the conclusion that the next phase of work should be the development of actual mission concepts. It is recommended, therefore, that mission concept studies be carried out for near-Earth orbiting VLBI experiments, including shuttle-based, space platform-based, and free-flying missions. The relative costs and benefits of the various concepts can guide the program development.

## II. A BRIEF DESCRIPTION OF VLBI TECHNIQUES

The technique of very long baseline radio interferometry (VLBI) affords astronomers their highest-resolution look at cosmic phenomena. The basic principle of VLBI is the same as that of connected-element radio interferometry - the synthesis of a large aperture by the combination of the outputs of two or more widely-separated antennas.

In connected-element interferometry the outputs of the antennas are brought together in real time, while in VLBI they are recorded on separate magnetic tapes at each station and played back together at a later time. This flexibility leads to vastly increased angular resolution for VLBI. Connected-element arrays are limited to tens of kilometers in size by the requirements of real-time data and time-standard transmission and by the constraints of geography. For example, the longest baseline at the Very Large Array of the National Radio Astronomy Observatory (The VLA) is  $B_{\max} \approx 36$  km, or  $\approx 610,000$  wavelengths at the typical wavelength of  $\lambda 6$  cm. This corresponds to resolution of  $\delta\theta \approx \lambda/B_{\max} \approx 0.35$  arc seconds. On the other hand, VLBI antennas may be separated by as much as an earth diameter, although considerably less is more typical. If we take  $B_{\max} \approx 2R_E \approx 12700$  km as an example at  $\lambda 6$  cm the baseline is  $\approx 220$  million wavelengths, corresponding to resolution of  $\approx 1$  milliarcsecond, 350 times better than the VLA.

In each kind of interferometry the basic measurement for a source in a direction  $\hat{s}$  is the correlated output of two antennas separated by an instantaneous baseline  $\vec{B}$ . This is called the visibility  $V$  of the source, and is a (complex) function of the source brightness distribution on the sky,  $B(\alpha, \delta)$ , and of the perpendicular component of the baseline,

$\vec{B}_\perp = \vec{B} - (\vec{B} \cdot \hat{s})\hat{s}$ .  $\vec{B}_\perp$  is usually resolved into components along the (projected-on-the-sky) east and north directions; in units of the wavelength of observation, these components are referred to as  $u$  and  $v$ . As the earth rotates with respect to the source so does the baseline, the projected baseline tracing out an elliptical path in  $(u,v)$  - space. The parameters of the  $u$ - $v$  track depend on the length and orientation of  $\vec{B}$ , on the coordinates  $(\alpha, \delta)$  of the source, and on the time included in the observation.

The relationship between the source brightness distribution  $B(\alpha, \delta)$  and the measured visibility  $V(u,v)$  is that of a Fourier transformation,

$$V(u,v) = \int_{-\infty}^{\infty} dx \int_{-\infty}^{\infty} dy B(x,y) \exp [2\pi i(ux+vy)],$$

where  $x$  is an eastward and  $y$  a northward angular displacement from the source center  $(\alpha, \delta)$ . Knowledge of the visibility at all  $(u,v)$  would enable us to reconstruct the source brightness from the inverse transform,

$$B(x,y) = \int_{-\infty}^{\infty} du \int_{-\infty}^{\infty} dv V(u,v) \exp [ -2\pi i (ux + vy)].$$

However, the visibility can be measured only at those  $(u,v)$  points which correspond to possible projected separations of the various antennas which are used. In connected-element arrays such as the VLA, the  $N$  antennas are so arranged that the coverage of the  $(u,v)$  plane which is afforded by the Earth's rotation of the  $\frac{N(N-1)}{2}$  baselines is very dense out to some maximum spacing  $B_{\max}/\lambda$ , and is zero beyond. As a result, a nearly-complete Fourier inversion of finite resolution is possible. The result  $M(x,y)$  (the "dirty map") is the convolution of the true source distribution  $B(x,y)$  with

the point response  $R(x,y)$  (the "dirty beam") of the observation, which is the Fourier inverse of the  $u$ - $v$  coverage, i.e.,

$$M(x,y) = B * R = \iint dx' dy' B(x', y') R(x-x', y-y')$$

$$R(x,y) = \int du \int dv \exp [-2\pi i (uv + vy)].$$

(Sampled points)

The beam  $R$  is a sharply-peaked function of angular width  $\delta\theta$  (the resolution) of

$$\delta\theta \approx \lambda / B_{\max},$$

which, because of the incompleteness of the  $u$ - $v$  coverage, possesses a low, non-zero sidelobe level.

The effect of the beam sidelobes is to mix the true source brightness at a given point with a fraction of the source brightness of nearby points. Because the Fourier inverse of the beam  $R$  has zeros (it is the  $u$ - $v$  coverage), a recovery of  $B$  using the Fourier convolution theorem is not possible, so an approximate deconvolution of the dirty map is performed in the map plane. This procedure, called "cleaning" the map, consists of successively subtracting point-source responses from the highest points in the dirty map, storing the amplitudes of these "components", and then reconstructing the map by convolving these point amplitudes with a "clean" beam having the same width as the central peak of the dirty beam, but no sidelobes (Högbom 1974). With a dirty beam of low sidelobe level this non-linear procedure works well, and it is possible to produce a "clean map" of a complicated source which has a dynamic range (the ratio of the brightest map feature to the weakest believable one) close to the limit imposed by the noise in the receivers. The dynamic range typically achieved with the VLA, where  $N = 27$  so the  $u$ - $v$  plane is very well sampled, is several hundred

to several thousand. However, in VLBI as currently practiced, the antennas are few in number ( $N \leq 7$ ) and somewhat arbitrarily located on the Earth, so the  $(u-v)$  plane can be sampled only sparsely. The "holes" which result in the  $(u-v)$  coverage have the consequence of a dirty beam with a high sidelobe level. Under these circumstances the map cleaning does not work very well, and the dynamic range of the clean map is severely limited, often ten or less. As we shall demonstrate in the next section, one of the important advantages of a Space-VLBI observation over current Earth-based VLBI is the tremendous improvement in the density of the  $(u-v)$  coverage which is obtainable for a given source, with the result of greatly-reduced sidelobe levels, and therefore significantly improved maps.

The second difference between connected-element interferometry and VLBI concerns the measurement of the phase of a visibility point  $V(u,v)$ . In connected-element interferometry a single clock keeps time for each of the antennas, so the phase visibility points for any one baseline is directly comparable to that obtained simultaneously on every other baseline. (Of course, the actual measured phase depends on time-dependent instrumental constants which must be removed by observation of suitable point sources, for which the visibility is independent of  $(u,v)$ , and for which the phase is defined to be zero). In contrast, in VLBI each station has a separate clock. These clocks are sufficiently stable that when the outputs of two stations are combined, a coherent cross-correlation may be obtained for a time long enough to reach a suitable signal-to-noise ratio for each separate visibility point  $V(u,v)$ . However, because of longer-term clock drifts, and other instrumental and atmospheric effects, it is not possible to directly compare the phases of visibility points obtained on different baselines at the same time, or on a single baseline

at widely separated times. Thus a direct Fourier inversion approach to map making is not very useful. The earliest VLBI observations were therefore confined to measurement of the amplitude of the visibility, and map making was reduced to modeling the amplitude of the visibility by the sum of a small number of elliptical gaussians.

Recently, more sophisticated VLBI data reduction techniques which do make use of the measured phases have been developed. When observations on any three baselines which form a closed loop (i.e., from the same three stations) are combined in a suitable way the net visibility phase around the loop is essentially free of instrumental effects. However, the resulting "closure phase" does depend on the structure of the source, and provides constraints in the source map which are in addition to those due to the amplitude information. When a reasonable number of antennas are involved, the closure phases contain almost all of the phase information that would be obtainable in connected-element interferometry (in an array of  $N$  antennas, we get all but  $2/N$  of the phase information). VLBI data reduction based on this idea is called "hybrid mapping", and has greatly improved the quality of VLBI maps. (Hybrid mapping is closely related to the "self-calibration" technique employed in phase-stable interferometry, in which an initial map of the source is used to generate a model visibility, which is in turn compared to the data and thereby used to correct the gains of the antennas. This procedure may be iterated several times, and works when there are many more baselines than antennas, so that the problem is well-constrained.) These techniques should be applicable to space-VLBI, but their use in the case of numerous baselines which are not simultaneously present has not been explored in detail. Of course, the use of closure phase will require the simultaneous use of a minimum of two ground stations in concert with a space VLBI terminal.

### III. ADVANTAGES OF A SPACE-VLBI STATION

We have studied the advantages of using one or more space VLBI stations in a variety of orbits to observe celestial objects at various positions in the sky. In this section we discuss the advantages of such a VLBI system compared to an Earth-bound system. One of the limitations of ground-based VLBI is the lack of large north-south antenna separations. This constraint, which arises because of the predominantly east-west distribution of habitable places on the earth, results in poor north-south resolution for celestial objects of low declination. A second limitation is that most of the large astronomical antennas are in the northern hemisphere, making the southern half of the sky effectively unobserved by VLBI. The use of a single space VLBI station immediately removes the first of these restrictions, and also opens up to VLBI all of the southern sky that can be seen from a single (or perhaps two) ground-based antenna. The existence of at least two large antennas in the southern hemisphere (Parkes 64-m and the JPL Deep Space Network 64-m in Australia) means that with space VLBI we can study objects anywhere in the sky. A third, fundamental, limitation of ground-based VLBI is the small number of antenna stations available. This results in a coarse and sporadic coverage of the Fourier transform ( $u-v$ ) space, since the spacing between various  $u-v$  tracks is dictated by the separations of the various antennas. Recent proposals for a dedicated VLBI array of approximately 10 antennas at sites chosen to "optimize" the  $u-v$  coverage go part of the way towards solving this problem, but the results are limited by the small number of stations that is economically feasible, and the difficulty of seeing a given source simultaneously from two ground stations which are far apart.

A single space VLBI station provides a continuously changing baseline to each ground station being used. Such a space terminal in a near-earth orbit circles the Earth about 8 times in a 12 hour period, and because the

ground stations are in different positions relative to the source for each orbit, a large number of u-v tracks result from each ground station. Figure III-1 shows the kind of u-v tracks generated by one orbit and by several consecutive orbits. As we demonstrate explicitly below, this results in u-v coverage which is decidedly superior to that obtainable with current ground-based antennas, and comparable in density and superior in resolution to that of the proposed dedicated VLBI arrays.

The fourth fundamental limitation of ground-based VLBI is that the longest baseline obtainable is the diameter of the Earth. In practice the maximum baseline is somewhat smaller than this because of the actual locations of Earth-based stations and of the requirement of simultaneous visibility of the source at both ends of a given baseline. The latter problem is exacerbated by the location of most large ground-based antennas at latitudes between 30 and 50 degrees north. The use of a single space station results in substantially increased usable baselines even for near-Earth spacecraft orbits. Larger orbits accessible to free-flying spacecraft result in dramatic increases in baseline, with concomitant increases in resolution.

#### Limits on Resolutions Due to Interstellar Scattering

The ultimate limit to the resolution of VLBI is set by interstellar scattering. Measurements at low frequencies have shown that a point source is broadened into a finite disk of size

$$\theta_s = 150 (\lambda/\lambda_0)^{\eta} \text{ milliarcseconds (mas)},$$

where  $\eta = \alpha/(\alpha - 2)$ ,  $\alpha$  is a poorly-known parameter, and  $\lambda_0 = 368$  cm corresponds to a frequency of 81.5 MHz (see Rickett 1977). Studies of the Crab pulsar have shown that  $\alpha \geq 3$ , so that  $\eta \leq 3$ ; a nominal value might be  $\eta = 2$ .

Figure III-1. Tracks in (u-v) space produced by one and by several consecutive orbits of a space VLB station and a single ground station.

ORIGINAL PAGE IS  
OF POOR QUALITY

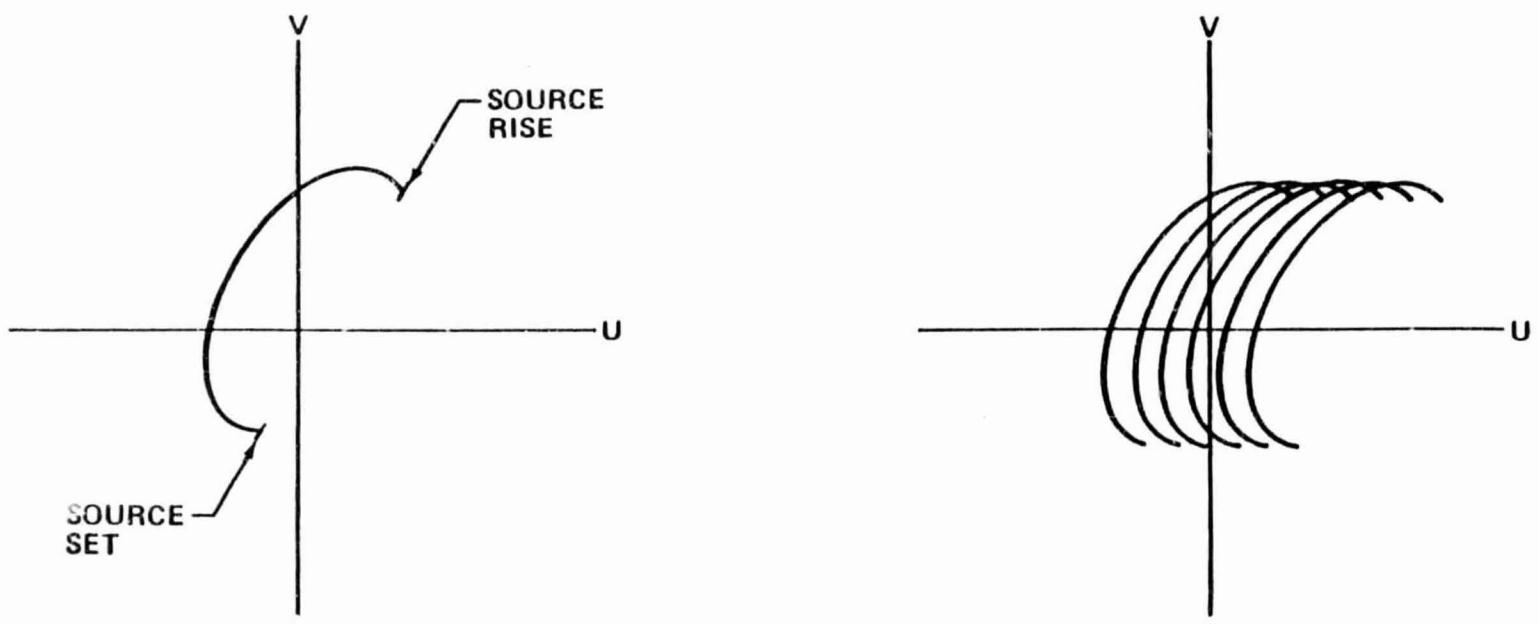


Figure III-1

The results below are quite sensitive to the exact value of  $\eta$  (because the VLBI frequencies are so far from 81.5 MHz), so we present results for  $\eta = 2$  and  $\eta = 3$ .

The longest useful baseline is the one for which the angular resolution of the experiment,

$$\theta_r \approx \frac{\lambda}{B} \approx 2 \times 10^3 \lambda_{\text{cm}} / B_{\text{km}} \text{ mas},$$

is equal to the scattering disk  $\theta_s$ . Since

$$\theta_s = \begin{cases} 1.1 \times 10^{-3} \lambda_{\text{cm}}^2 & \text{mas} & \eta = 2, \\ 3.0 \times 10^{-6} \lambda_{\text{cm}}^3 & \text{mas} & \eta = 3, \end{cases}$$

the maximum useful baseline, expressed in Earth radii, is about

$$B_{\text{max}} / R_E \approx \begin{cases} 300 \lambda_{\text{cm}}^{-1} & (\eta = 2), \\ 1.1 \times 10^5 \lambda_{\text{cm}}^{-2} & (\eta = 3). \end{cases}$$

In Table III-1 we present the maximum baseline, and resulting maximum angular resolution, as a function of observing wavelength, for the cases  $\eta = 2$  and  $\eta = 3$ , along with the resolution currently obtainable ( $\theta_{\text{GB}}$ ) from ground-based VLBI, assuming  $B_{\text{max}} = R_E$ . For the case  $\eta = 3$  ( $\alpha = 3$ ), it is clear that almost unlimited resolution is theoretically possible - interstellar scattering falls off with decreasing wavelength so fast ( $\theta_s \propto \lambda^3$ ) that at the higher frequencies used for VLBI the scattering is negligible for baselines which are tens of thousands of Earth radii. However, if  $\eta = 2$  ( $\alpha = 4$ ), the scattering disk remains a constraint for baselines of a few hundred Earth radii, and resolution would be limited to a few hundred times that currently available. It might be added that a determination of  $\alpha$  can only be made with long baselines and short wavelengths, so space VLBI will lead to important new

TABLE III-1

Maximum Useful Baseline and Resulting Resolution

	$\lambda$ (cm)	50	18	6	2.8	2.0	1.35
	$\theta$ (mas) GB	17	5.9	2.0	0.92	0.66	0.45
= 2	$\left\{ \begin{array}{l} \theta \text{ (mas)} \\ B_{\text{max}} (R_E) \end{array} \right.$	2.8	0.36	0.040	0.0086	0.0044	0.0020
		6.0	17.	50.	110.	150.	220.
= 3	$\left\{ \begin{array}{l} \theta \text{ (mas)} \\ B_{\text{max}} (R_E) \end{array} \right.$	0.38	0.017	$6.5 \times 10^{-4}$	$6.6 \times 10^{-5}$	$2.4 \times 10^{-5}$	$7.4 \times 10^{-6}$
		44.	340.	3100.	$1.4 \times 10^4$	$2.8 \times 10^4$	$6.0 \times 10^4$

information about the interstellar medium.

In the next section we begin our detailed examination of the properties of space VLBI with a discussion of the spacecraft orbits involved.

### Specification of the Orbit

The orbit of a satellite about the Earth is specified by six elements, three which give the size and shape of the orbit and the satellites' initial position in the orbit, and three which specify the orbit's orientation in space. The semi-major axis  $a$  and eccentricity  $e$  specify the size and shape of an elliptical orbit. The satellite's position in the orbit at an initial time  $t_0$  may be specified by the initial mean anomaly

$$\bar{M}_0 = \frac{2\pi}{T} (t_0 - t_p), \text{ [modulus } 2\pi],$$

where  $T$  is the orbital period and  $t_p$  is the time of perigee passage. The period of the orbit is related to its semi-major axis by Kepler's third law,

$$T^2 = \frac{4\pi^2 a^3}{G M_E},$$

where  $G = 6.67 \times 10^{-8}$  cgs is Newton's constant of gravity and  $M_E = 5.98 \times 10^{27}$  g is the mass of the Earth. Numerically,

$$T(\text{minutes}) = 1.659 \times 10^{-4} \cdot a^{3/2} \text{ (km)}$$

$$a(\text{km}) = 331.3 T^{2/3} \text{ (min)}.$$

The standard circular orbits available from the Space Shuttle will have altitude  $h$  in the range  $270 \leq h \leq 400$  km, so since the mean radius of the Earth is  $R_E = 6371$  km, these have periods in the range  $89.8 \leq T \leq 92.4$  min. An Earth-synchronous orbit of period 24 hours has  $a \approx 42200$  km, so  $h \approx 35800$  km. A highly eccentric orbit with  $a=100,000$  km and  $e = 0.90$ , corresponding to altitudes  $3630 \text{ km} \leq h \leq 184000 \text{ km}$  has  $T \approx 5240 \text{ minutes} = 3^d 15^h 20^m$ .

The orientation of the orbit is described by two angles which specify the plane in which it lies and by one which specifies a direction in that plane. For orbits around the Earth it is convenient to refer the orbital plane to the plane containing the Earth's center and equator, and whose intersection with the celestial sphere is the celestial equator, and to choose the fiducial direction in that plane to be toward the Vernal Equinox  $\gamma$  (origin of right ascension,  $\alpha = 0^h$ ). The longitude of the ascending node  $\Omega$  is the angular distance along the celestial equator between  $\gamma$  and the ascending node of the orbit,  $N_A$ , the point at which the plane of the orbit intersects the equatorial plane and at which the projected motion of the satellite is from the southern into the northern hemisphere. The inclination of the orbit  $i$  is the angle ( $0 \leq i \leq \pi$ ) between the orbital plane and the equatorial plane; orbits are called prograde if  $i < \frac{\pi}{2}$  and retrograde if  $i > \frac{\pi}{2}$ , corresponding to satellite revolution in the same direction and the direction opposite the Earth's rotation, respectively.

The sixth orbital element is the longitude of perigee  $\omega$ , which specifies the location of the perigee of the orbit with respect to the Celestial Equator. It is the angular distance along the projection of the orbit onto the celestial sphere from the ascending node to the point of perigee passage, and satisfies  $0 \leq \omega \leq 2\pi$ . When  $\omega = 0$  or  $\omega = \pi$ , the major axis of the orbit lies in the celestial plane of the celestial equator, while when  $\omega = \frac{\pi}{2}$  or  $\omega = \frac{3\pi}{2}$  the minor axis is parallel to this plane. The geometry of orbital orientation in space is illustrated in Figure III-2.

The velocity  $v$  of the satellite in its orbit is

$$v(\text{km/s}) = 7.91 \left( \frac{2R_E}{r} - \frac{R_E}{a} \right)^{1/2},$$

Figure III-2. Geometry of the orbital elements for a spacecraft in orbit about the Earth.



where  $r$  is the length of the radius vector between the instantaneous position of the satellite and the center of the Earth. The maximum velocity occurs at perigee, where  $r$  is a minimum,

$$r_{\min} = a(1-e),$$

and is

$$v_{\max} = \left( \frac{GM_E}{a} \right)^{1/2} \left( \frac{1+e}{1-e} \right)^{1/2} = 7.91 \left( \frac{R_E}{a} \right)^{1/2} \left( \frac{1+e}{1-e} \right)^{1/2} \text{ km/s},$$

while the minimum velocity occurs at apogee,

$$r_{\max} = a(1+e),$$

and is

$$v_{\min} = v_{\max} \frac{(1+e)}{(1+e)} = 7.91 \left( \frac{R_E}{a} \right)^{1/2} \left( \frac{1-e}{1+e} \right)^{1/2} \text{ km/s}.$$

Thus the circular shuttle orbits have  $v \approx 7.7$  km/s, a large elliptical orbit ( $a = 100,000$  km,  $e = 0.9$ ) has  $v_{\max} = 8.7$  km/s,  $v_{\min} \approx 0.5$  km/s, and a geostationary orbit has  $v \approx 3.1$  km/s. By way of comparison, the velocity of a ground-based station at latitude  $\phi$  is that of the rotating earth,

$$v_g = 0.46 \cos \phi \text{ (km/s)}.$$

As we demonstrate below, the fact that the station velocities appropriate to space VLBI are one order of magnitude larger than those encountered in ground-based observations necessitates only minor changes in the data processing, but enormous improvements in the possible u-v coverage.

#### IV. SIMULATIONS OF SPAC<sup>F</sup>-VLBI OBSERVATIONS - - NEAR-EARTH ORBITS

In order to better understand the properties-- advantages and restrictions-- of VLBI with one or more antennas in orbit we have performed simulations of such observations, varying the source position, spacecraft orbital elements, and the number and locations of the ground stations involved. In this section we present the results for simulations involving a single space-borne antenna in near-Earth orbit.

The dependence of the resulting u-v tracks on the relative source-orbit orientation is demonstrated by the examples in Figures IV-1a through IV-1d (summarized in Table IV-2). In each case the source is at  $\alpha = 0^h$ ,  $\delta = +30^\circ$ ; referring to Figure III-2, the source has right ascension corresponding to the direction of the Vernal Equinox ( $\gamma$ ), and is located  $30^\circ$  above the plane of the celestial equator. The orbit is chosen to be circular and to have inclination  $i = 60^\circ$ ; the longitude of the ascending node ( $\Omega$ ) is varied from  $0^\circ$  to  $270^\circ$  in steps of  $90^\circ$ . As a result the orbit is "side-on" (Figure IV-1a), "face-on" (IV-1b), "side-on" (IV-1c), and "back-on" (IV-1d) to the source directions, respectively. The u-v tracks which result from a 24-hour observation with a single ground antenna demonstrate how these geometrical relationships translate into u-v coverage. It is clear that an orbit which is exactly "face-on" to a source with coordinates  $(\alpha, \delta)$  has elements

$$i_{\text{opt}} = 90^\circ - \delta$$

$$\Omega_{\text{opt}} = \alpha + 90^\circ;$$

such an orbit results in u-v tracks with the maximal extent both N-S and E-W.

TABLE IV-1

Four Orbits Projected on the u-v Plane for a Source at  $\alpha = 0^h$ ,  $\delta = +30^\circ$

<u>Figure</u>	<u>Ground Stations</u>	<u>Space VLB Terminal*</u>	
		<u>1</u>	<u>2</u>
la	Goldstone	60°	0°
lb	Goldstone	60°	90°
lc	Goldstone	60°	180°
ld	Goldstone	60°	270°

\*In all cases the space antenna is in a circular orbit at an altitude of 370 km.

Figure IV-1: Fourier (u-v) coverage and resulting synthesized beam from simulations of VLBI observations of a single source ( $\alpha = 0^{\text{h}}$ ,  $\delta = +30^{\circ}$ ) from four different orbits ( $i = 60^{\circ}$ ;  $\Omega = 0^{\circ}, 90^{\circ}, 180^{\circ}, \text{ and } 270^{\circ}$ ). The angular scale assumes that the observing wavelength was 18 cm ( $\nu = 1.665$  GHz).

ORIGINAL PAGE IS  
OF POOR QUALITY

$\alpha = 0^h, \delta = +30^\circ$   
GDSTN  
SHUTTLE ( $i = 60^\circ; \Omega = 0^\circ$ )

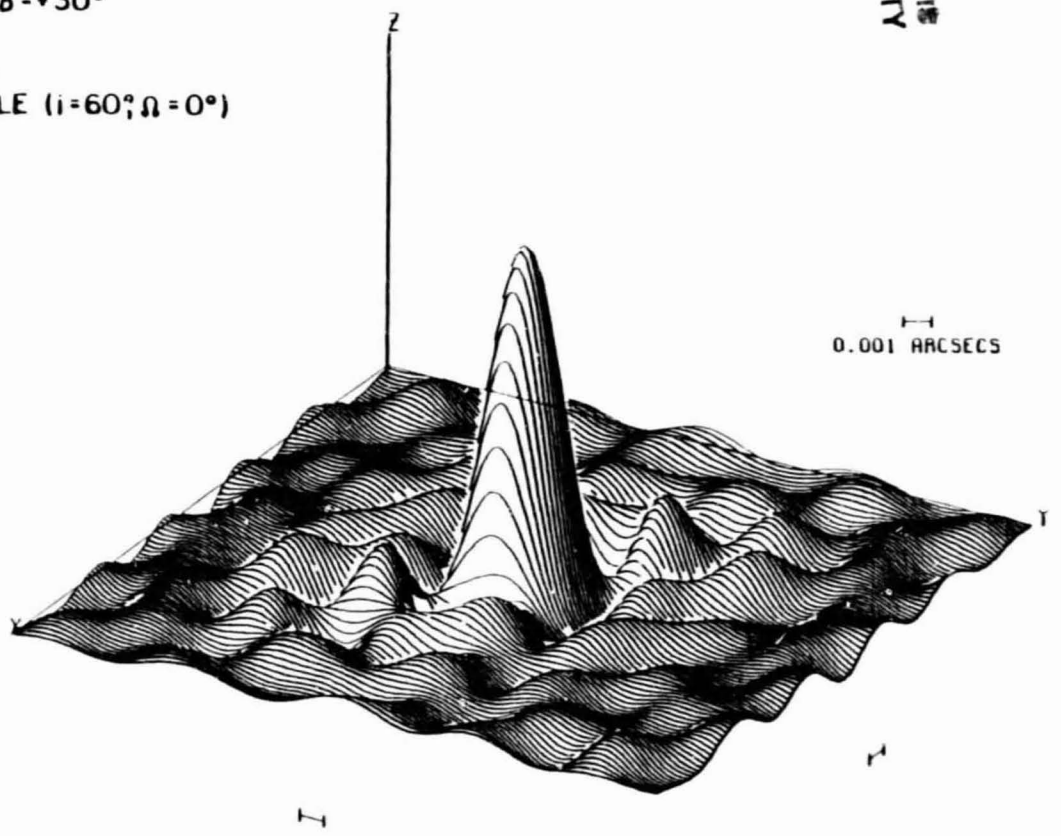
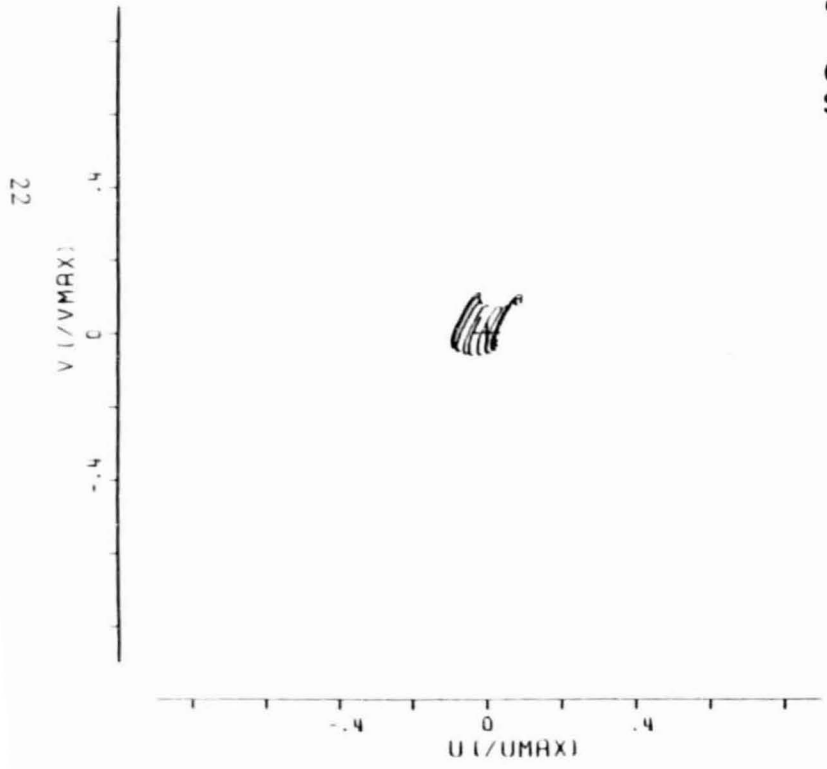
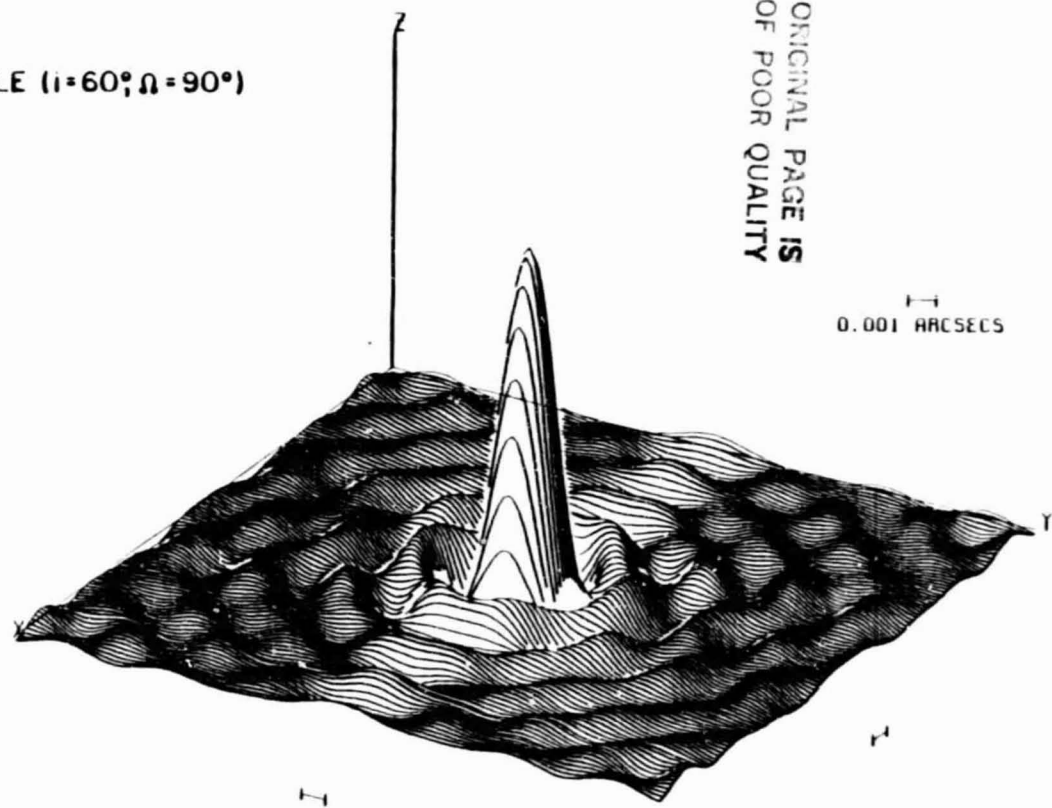
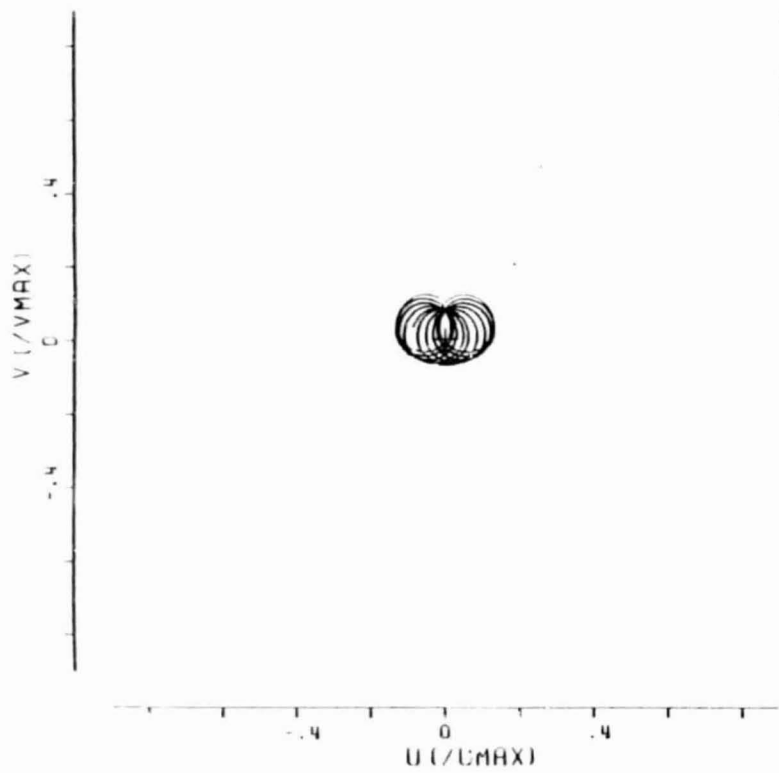


Figure IV-1a

$\alpha = 0^h, \delta = +30^\circ$ 

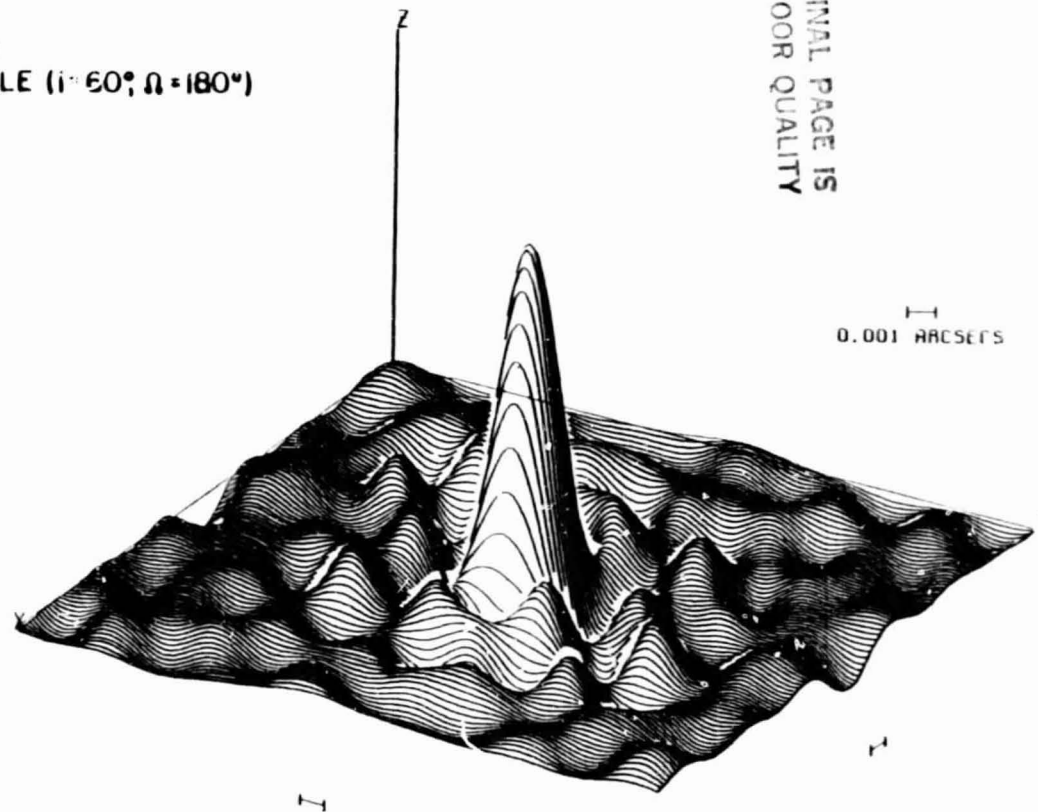
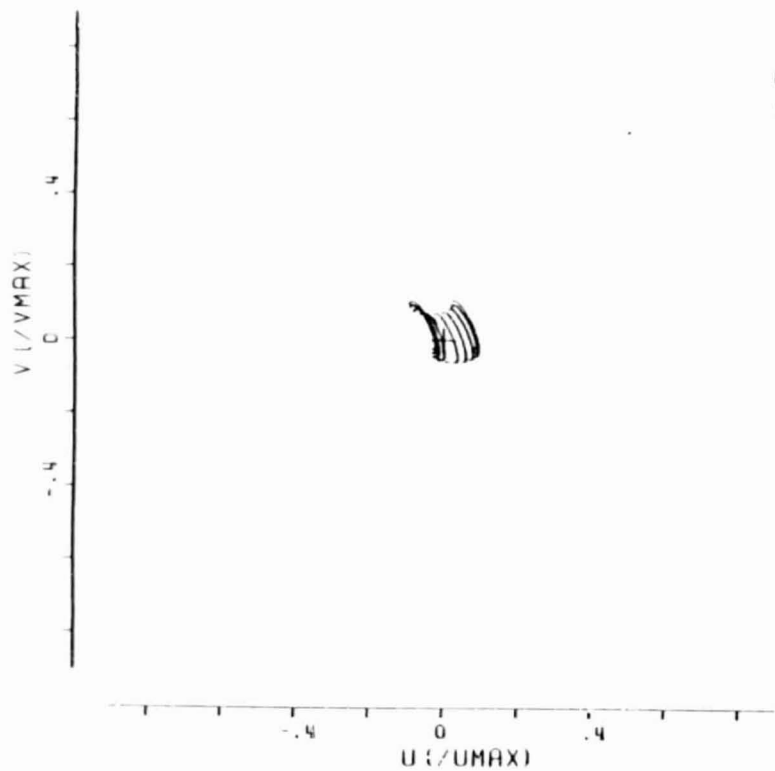
 GDSTN  
 SHUTTLE ( $i=60^\circ; \Omega=90^\circ$ )

 ORIGINAL PAGE IS  
 OF POOR QUALITY

 $0.001$  ARCSECS

Figure IV-1b

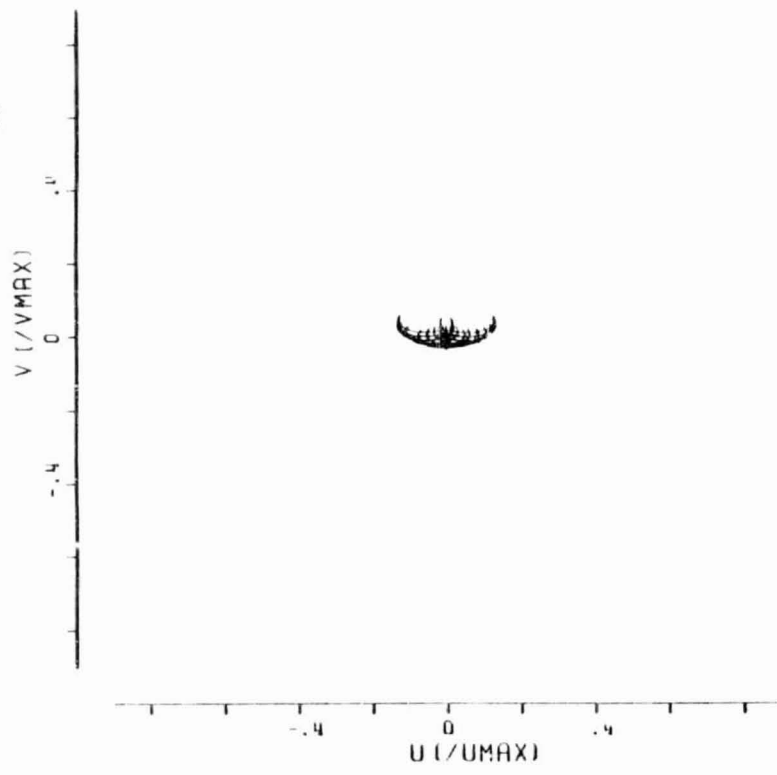
$\alpha = 0^\circ, \beta = +30^\circ$

GDSTN  
SHUTTLE ( $i = 60^\circ, \Omega = 180^\circ$ )



ORIGINAL PAGE IS  
OF POOR QUALITY

Figure IV-1c



$\alpha = 0^h, \delta = +30^\circ$   
GDSTN  
SHUTTLE ( $i = 60^\circ, \Omega = 270^\circ$ )

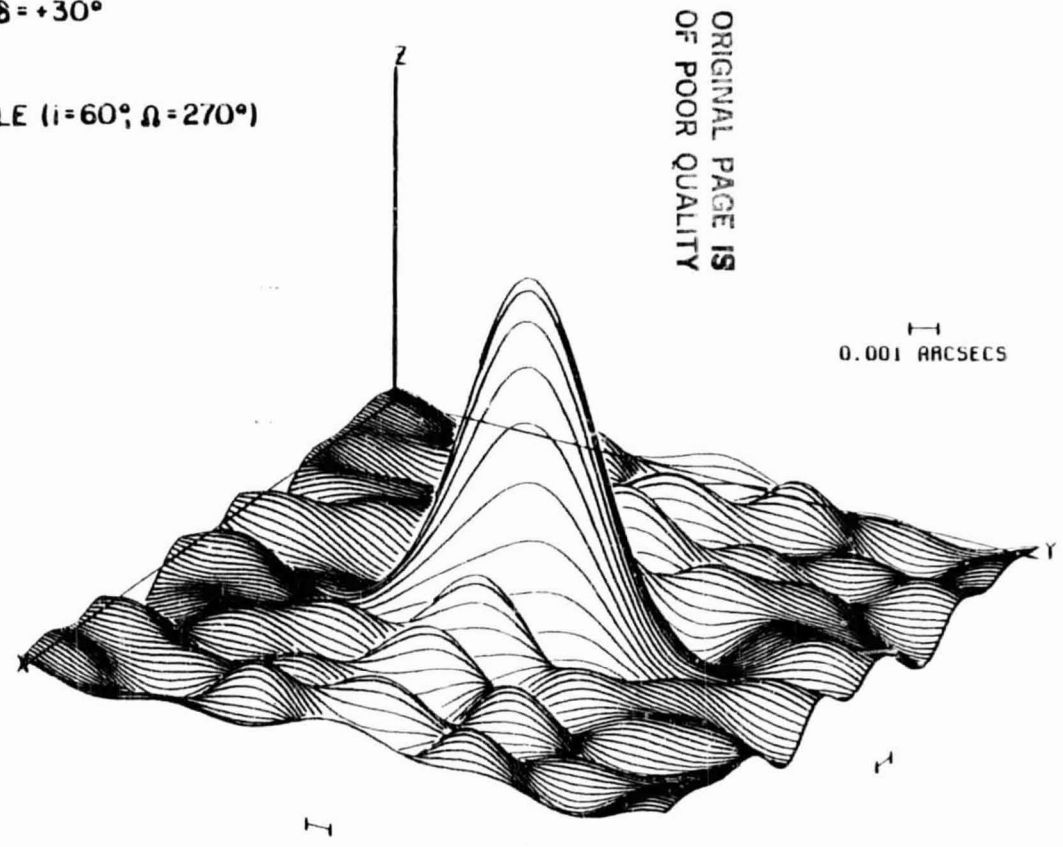


Figure IV-1d

On the right hand side of each figure is a "three-dimensional" plot of the dirty beam (point response) corresponding to the u-v coverage shown on the left. In these plots the x-axis is East-West, the y-axis is North-South, and the z-axis is the amplitude of the response. The angular scale for the beam plot will depend on the wavelength used in the particular simulations, and can easily be scaled for any desired value. For Figures IV-1 the wavelength used was 18 cm; for the rest of the simulations the figure captions contain this information.

#### A. Simulations for Three Real Sources

Several simulations of observations of real astronomical sources are summarized in Table IV-2. In each case a series of several ground antenna combinations has been used, followed by a spacecraft simulation employing three ground stations. The spacecraft orbit was fixed, and the results illustrate the various morphologies of u-v tracks which can result.

For the source 3C84, a high-declination radio galaxy, ground-based VLBI produces rather good u-v tracks, even with only three US-based stations (Figure IV-2a). Inclusion of a midwest station (North Liberty, Iowa; Figure IV-2b) helps to fill in the "holes", and addition of a European station (Bonn; Figure IV-2c) approximately doubles the extent of the u-v coverage. However, use of a single space-based antenna, illustrated in Figure IV-2d, clearly improves both the extent and density of the u-v coverage.

TABLE IV-2

Three Real Sources Observed with Various Combinations  
of Ground Stations and Space Stations

Figure	Name	Source		Ground Stations*	Space VLB Terminal**	
		$\alpha$	$\delta$		i	$\Omega$
2a	3C84	3 <sup>h</sup> 16 <sup>m</sup>	+41° 20'	HSTK,GB,OVRO	-	-
2b	3C84	3 <sup>h</sup> 16 <sup>m</sup>	+41° 20'	HSTK,GB,OVRO,NLRO	-	-
2c	3C84	3 <sup>h</sup> 16 <sup>m</sup>	+41° 20'	HSTK,GB,OVRO,BONN	-	-
2d	3C84	3 <sup>h</sup> 16 <sup>m</sup>	+41° 20'	HSTK,GB,OVRO	57°	90°
3a	3C273	12 <sup>h</sup> 27 <sup>m</sup>	+ 2° 19'	HSTK,GB,OVRO	-	-
3b	3C273	12 <sup>h</sup> 27 <sup>m</sup>	+ 2° 19'	HSTK,GB,OVRO,NLRO	-	-
3c	3C273	12 <sup>h</sup> 27 <sup>m</sup>	+ 2° 19'	HSTK,GB,OVRO,BONN	-	-
3d	3C273	12 <sup>h</sup> 27 <sup>m</sup>	+ 2° 19'	HSTK,GB,OVRO	57°	90°
4a	W49	19 <sup>h</sup> 08 <sup>m</sup>	+ 9° 01'	HSTK,GB,OVRO	-	-
4b	W49	19 <sup>h</sup> 08 <sup>m</sup>	+ 9° 01'	HSTK,GB,OVRO,NLRO	-	-
4c	W49	19 <sup>h</sup> 08 <sup>m</sup>	+ 9° 01'	HSTK,GB,OVRO,BONN	-	-
4d	W49	19 <sup>h</sup> 08 <sup>m</sup>	+ 9° 01'	HSTK,GB,OVRO	57°	90°

\* HSTK = Haystack Observatory, Westford, MA.

GB = NRAO, Green Bank, W.VA.

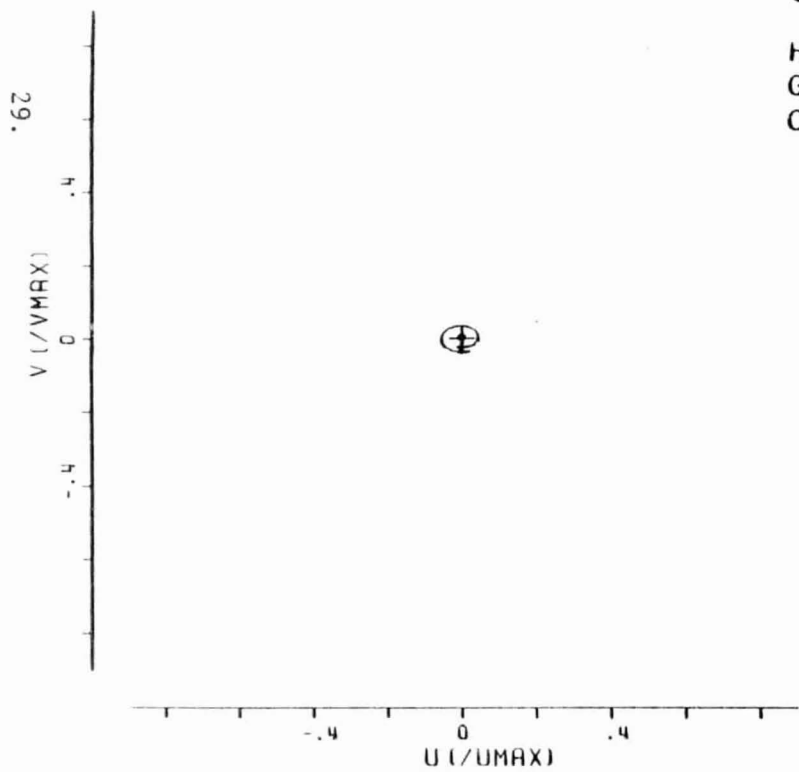
OVRO = Owens Valley Radio Observatory, Big Pine, CA.

NLRO = North Liberty Radio Observatory, North Liberty, IW.

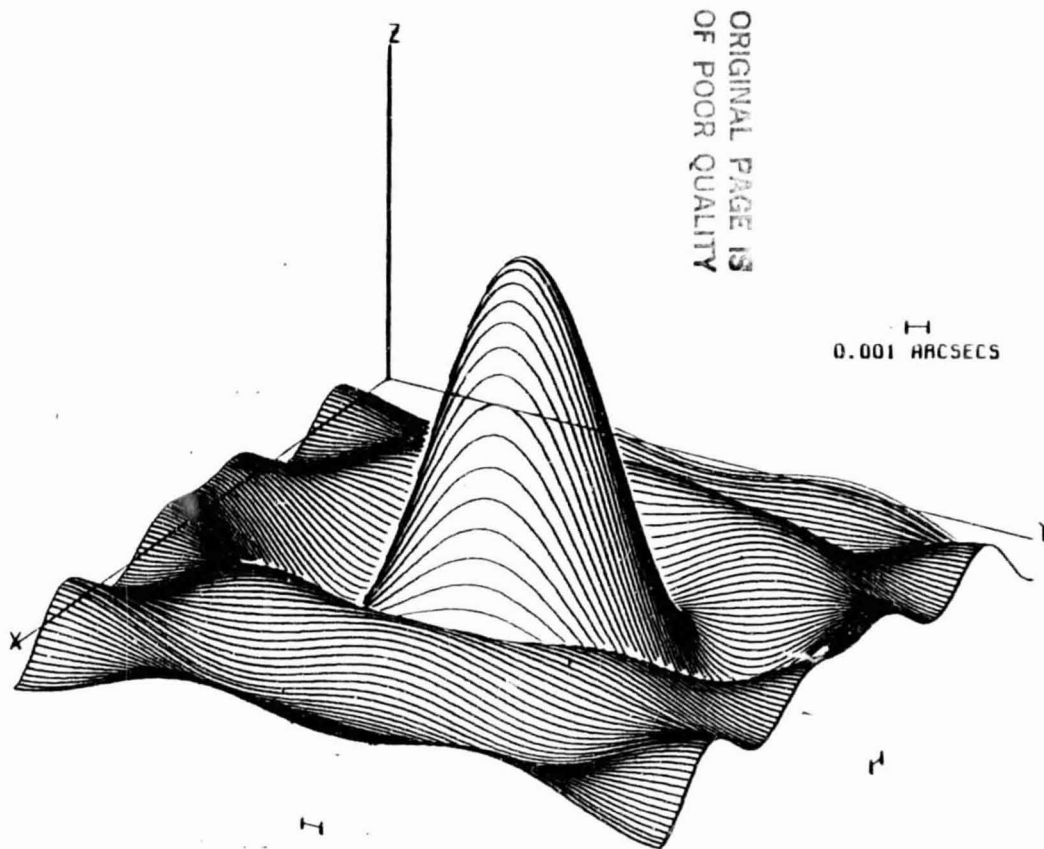
BONN = MPIfR, Bonn, West Germany

\*\*In all cases the space antenna is in a circular orbit at an altitude of 370 km.

Figure IV-2. Fourier coverage and resulting synthesized beam from simulated VLB observations of the source 3C84. The angular scale assumes that the observing wavelength was 18 cm.



3C84  
HSTK  
GB  
OVRO



ORIGINAL PAGE IS  
OF POOR QUALITY

Figure IV-2a

ORIGINAL PAGE IS  
OF POOR QUALITY

1  
0.001 ARCSECS

3C84

HSTK  
GB  
NLRO  
OVRO

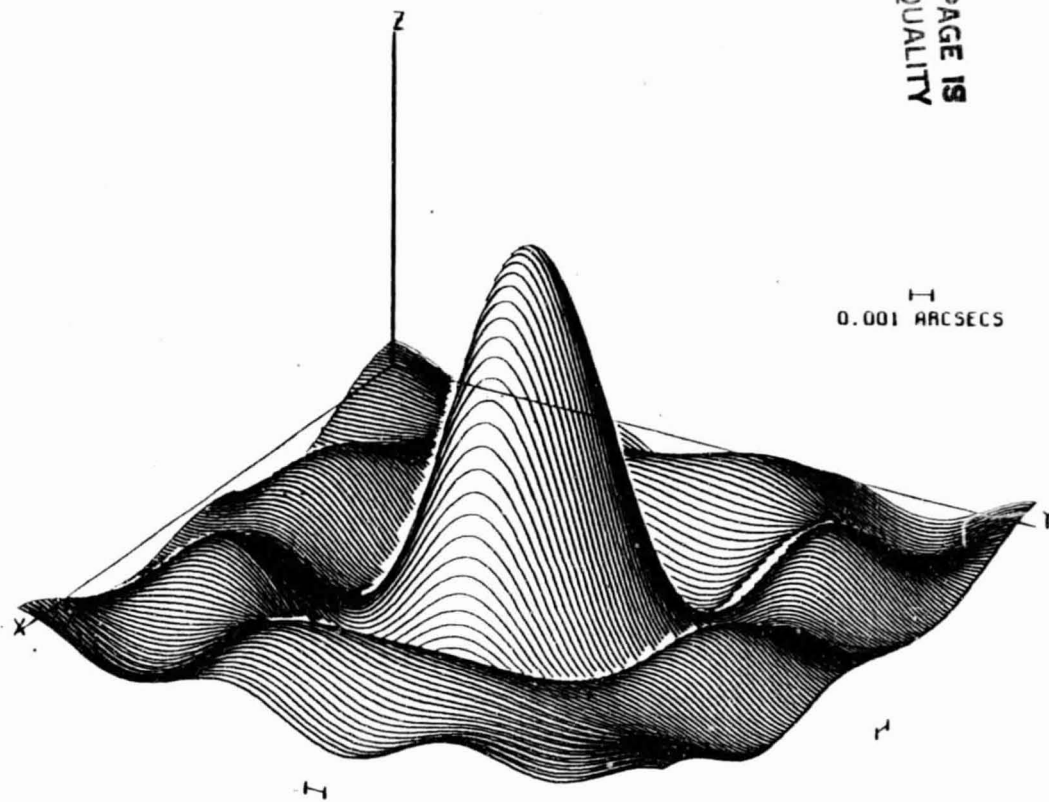
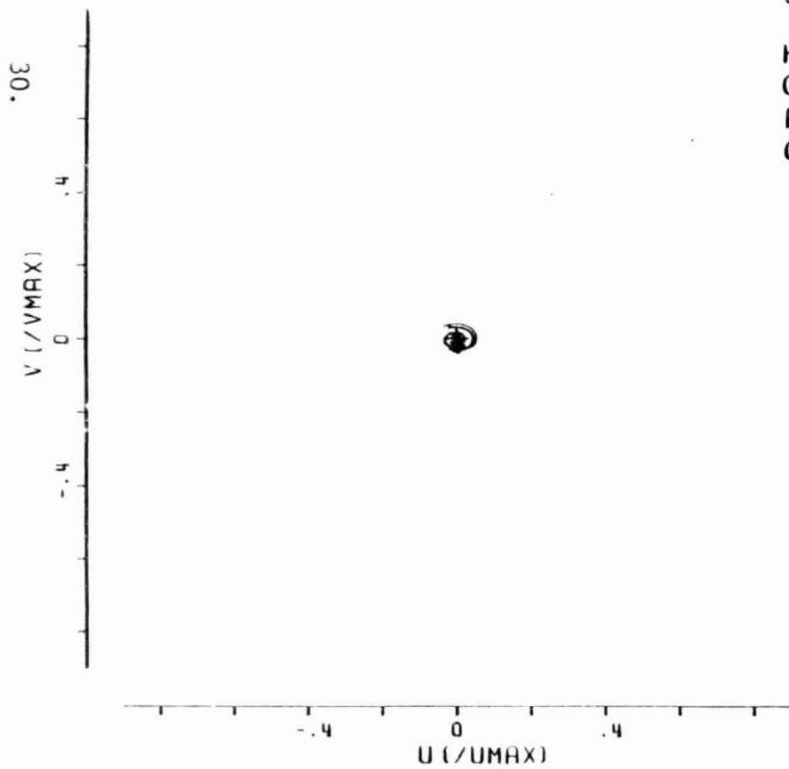
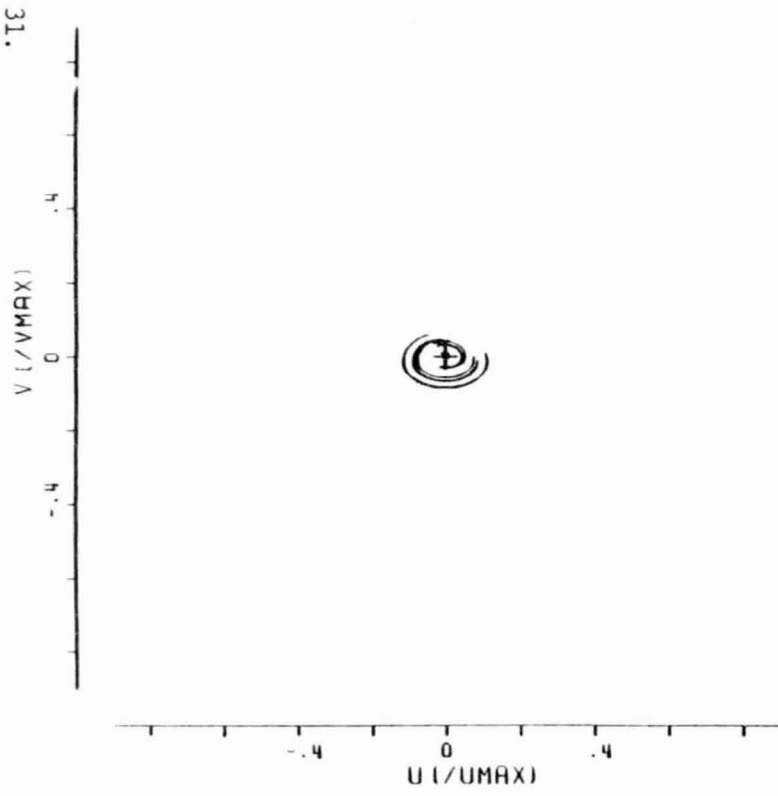
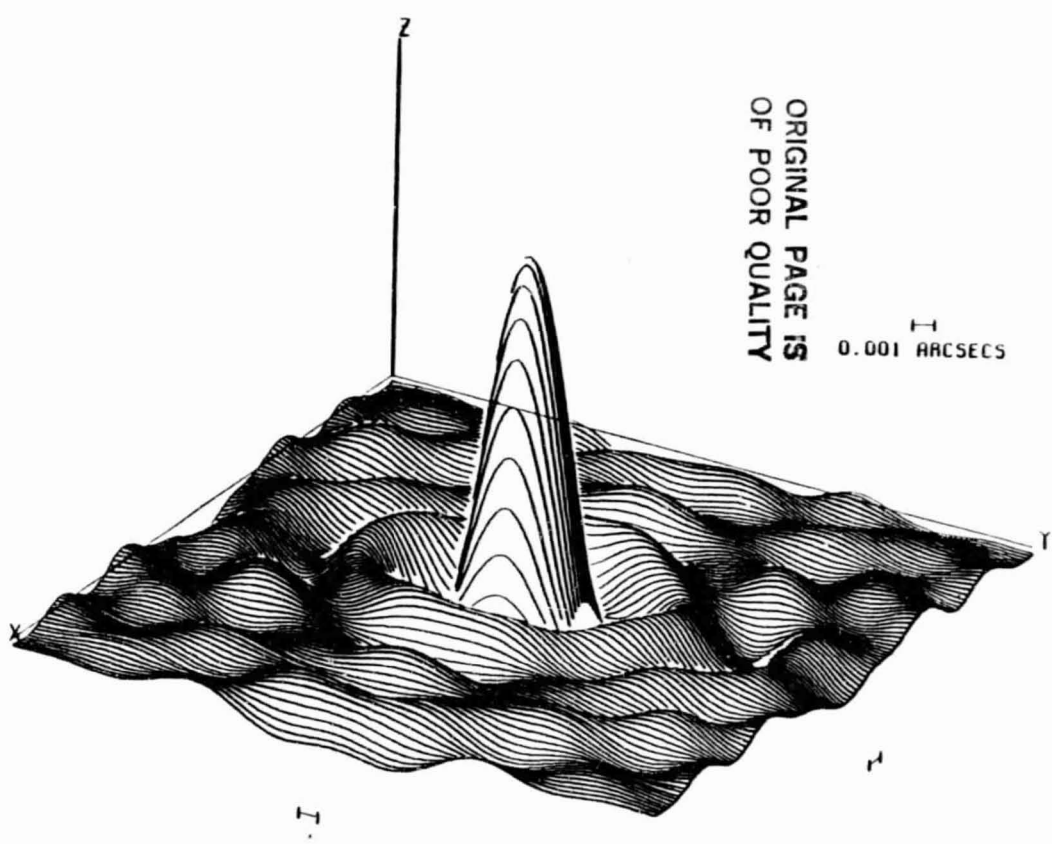


Figure IV-2b



3C84  
 HSTK  
 GB  
 OVRO  
 BONN



ORIGINAL PAGE IS  
 OF POOR QUALITY

0.001 ARCSECS

Figure IV-2c

ORIGINAL PAGE IS  
OF POOR QUALITY

3C84  
HSTK  
GB  
OVRO  
SHUTTLE ( $i=57^\circ$ ;  $\Omega=90^\circ$ )

0.001 ARCSECS

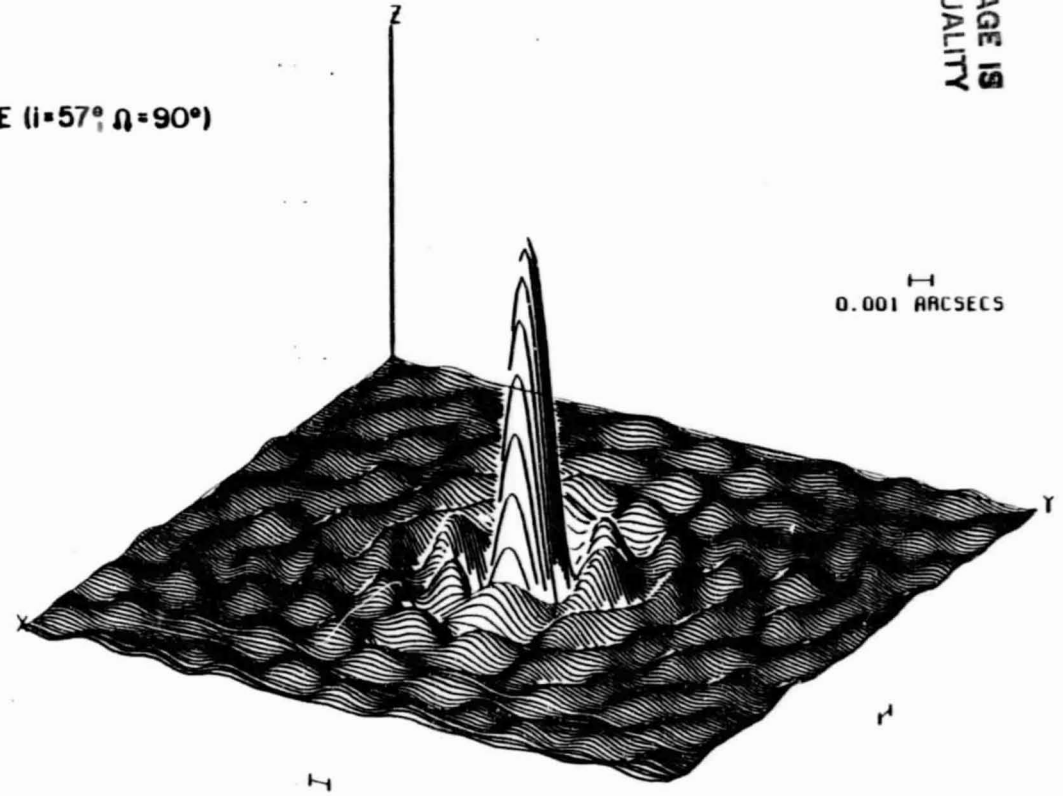
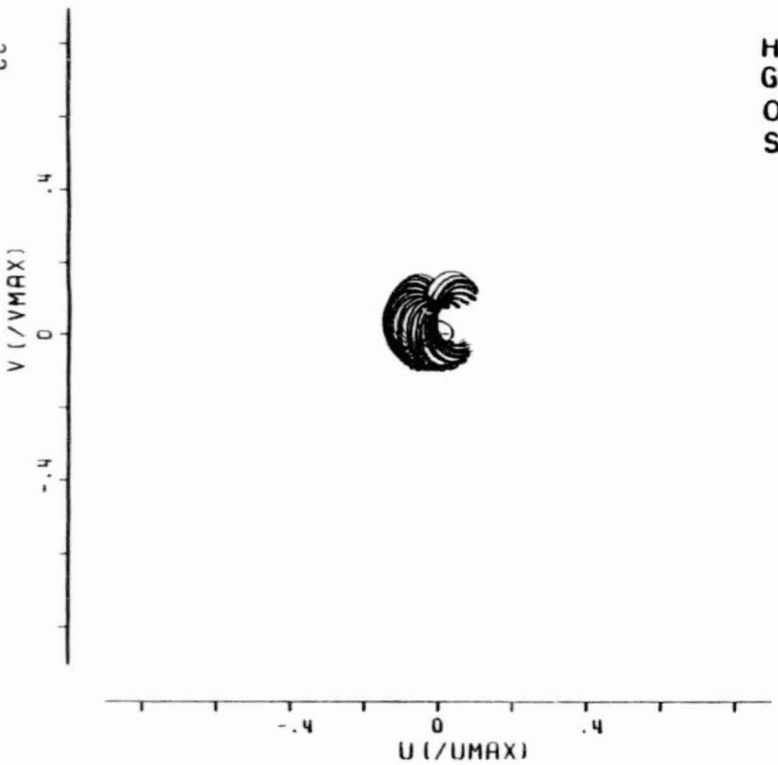
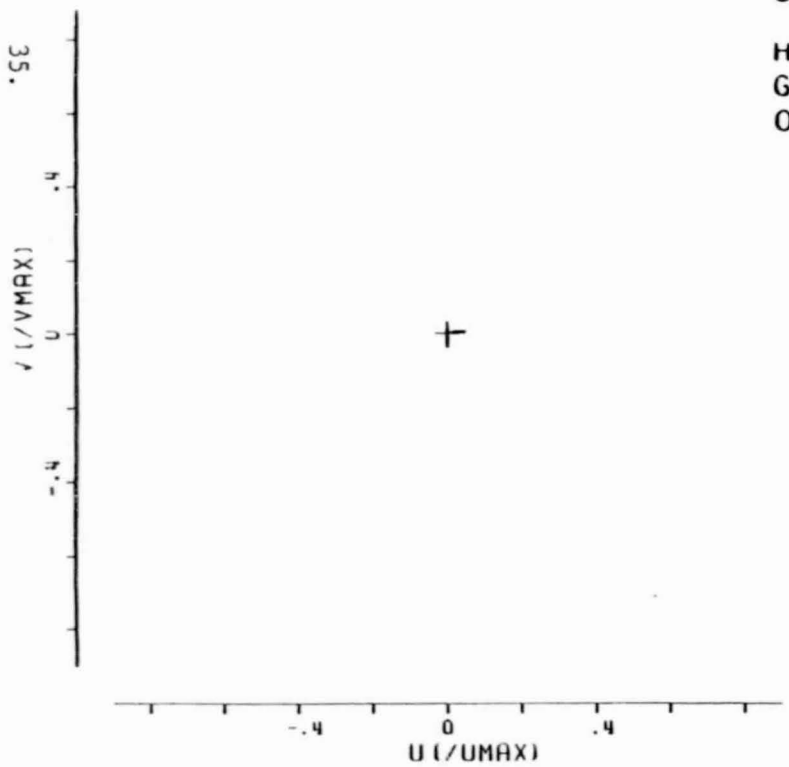


Figure IV-2d

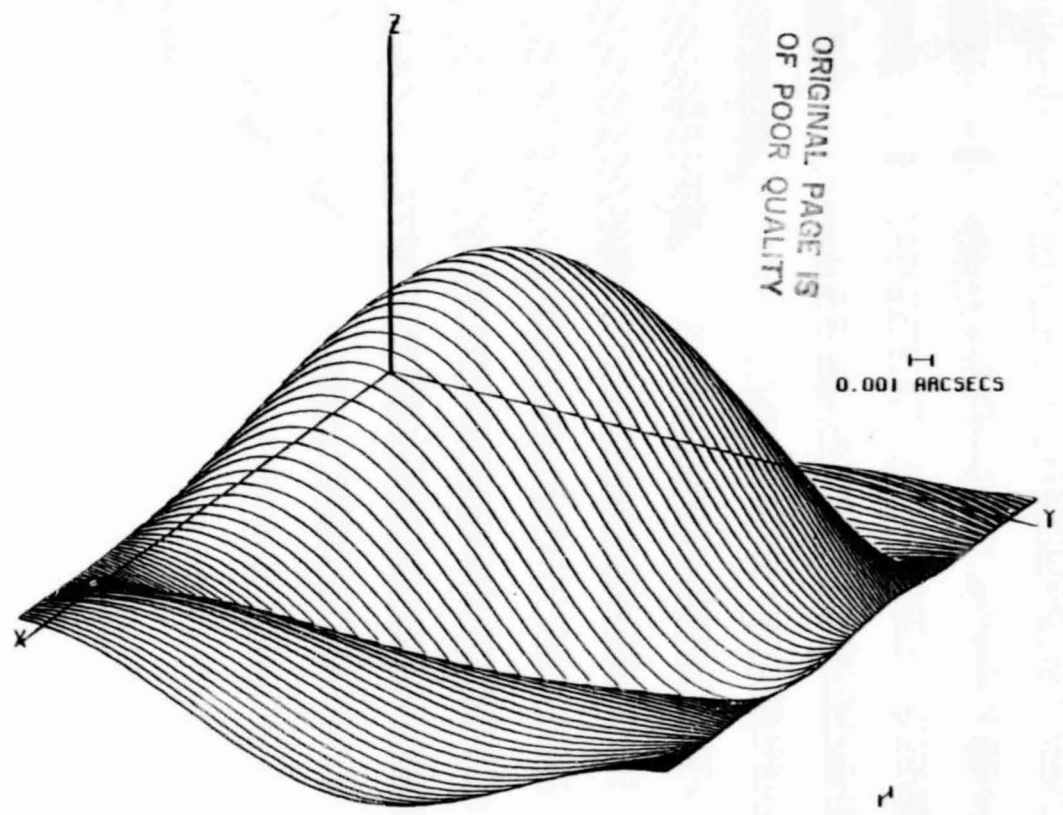
Figures IV-3 are the results of simulations for the low-declination quasar 3C273. As summarized in Table IV-2, the antennas involved in IV-3a through IV-3d are identical to those used for 3C84 above. Examination shows the dramatic effect of changing the source declination from  $\delta = 41^\circ$  to  $\delta = 2^\circ$ : ground-ground baselines involving the usual existing stations have almost no North-South baseline projection ( $v$ ). As a result, the  $u$ - $v$  coverage degenerates into East-West lines, and there is essentially no North-South ( $y$ ) resolution of the source. This is reflected in the extremely broad beams in Figures IV-3a through IV-3c. However, just as in the case with the high-declination source 3C84, use of the same single space antenna produces excellent  $u$ - $v$  coverage (Figure IV-3d). [In this case, even though the source right ascension ( $\alpha = 12^{\text{h}} 27^{\text{m}} \approx 187^\circ$ ) corresponds to a nearly "back-on" view of the orbit ( $\Omega = 90^\circ$ ), the  $u$ - $v$  coverage is good because the difference between "face-on" and "back-on" disappears for sources at very low declinations.]

Finally, in Figures IV-4 we present the results of simulations for the interstellar maser source W49. This also lies at low declination ( $\delta = 9^\circ$ ), but is about  $90^\circ$  away from 3C273 in right ascension. Figures IV-4a through c show that, for a ground-based array, poor North-South resolution occurs for  $\delta = 9^\circ$ , although it is not as poor as for 3C273. Figure IV-4d shows once again that, even for low-declination sources, inclusion of a single spaceborne antenna results in a dramatic improvement in the density and extent of the  $u$ - $v$  coverage. Comparison of Figures IV-1c ( $\alpha = 0^{\text{h}}$  and  $\Omega = 180^\circ$ ) and IV-4d shows that in this case (for W49) we have the same sense of "edge-on" orbits. This is in fact the case; W49 has  $\alpha = 19^{\text{h}} 08^{\text{m}} = 287^\circ$  and  $\Omega = 90^\circ$ , so  $\alpha - \Omega = 197^\circ$ , while the example of Figure IV-1c had  $\alpha - \Omega = -180^\circ = 180^\circ$ . Further comparison of Figures IV-1c and IV-4d shows how the additional ground stations of the latter case result in denser  $u$ - $v$  coverage, and thus in a lower sidelobe level than in the case of a single ground station.

Figure IV-3. Fourier coverage and resulting synthesized beam from simulated VLB observations of the source 3C273. The angular scale assumes that the observing wavelength was 18 cm.

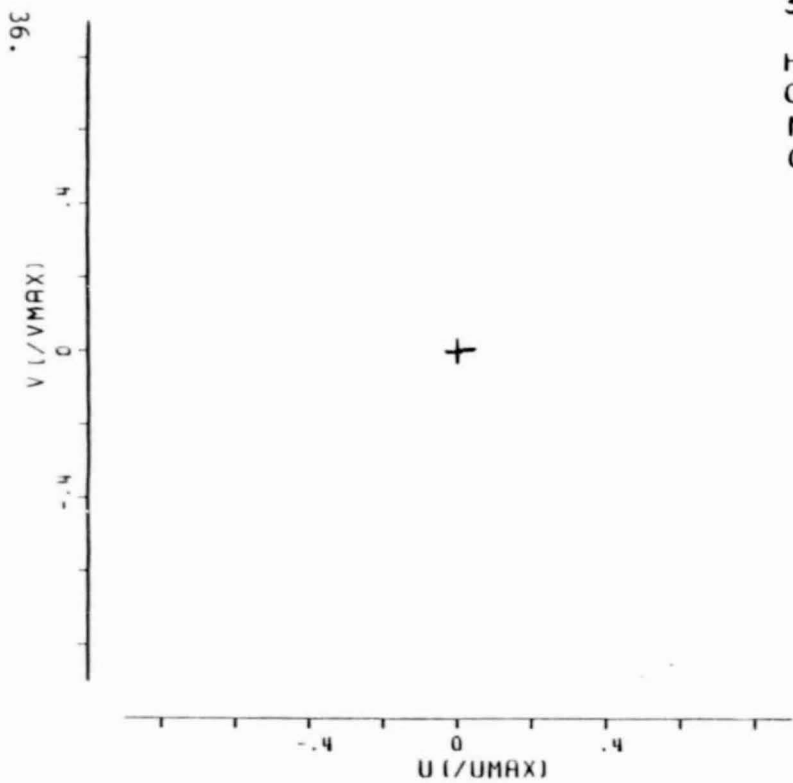


3C273  
 HSTK  
 GB  
 OVRO

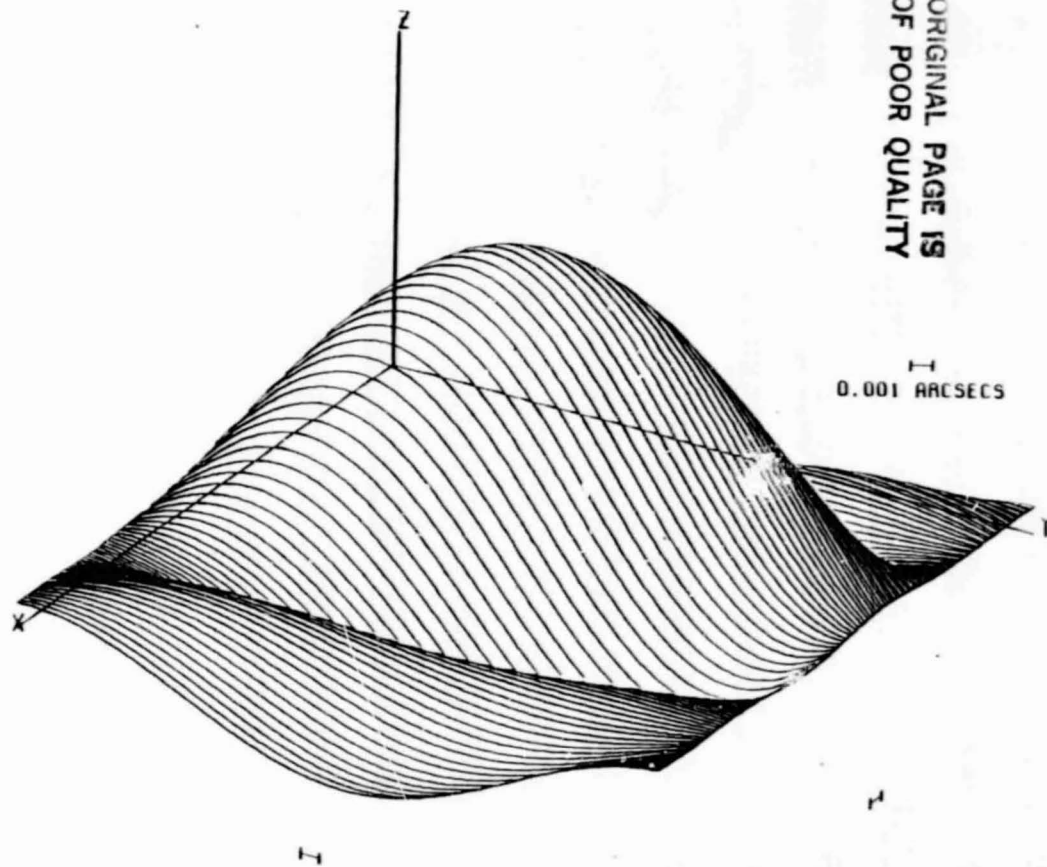


ORIGINAL PAGE IS  
 OF POOR QUALITY

Figure IV-3a



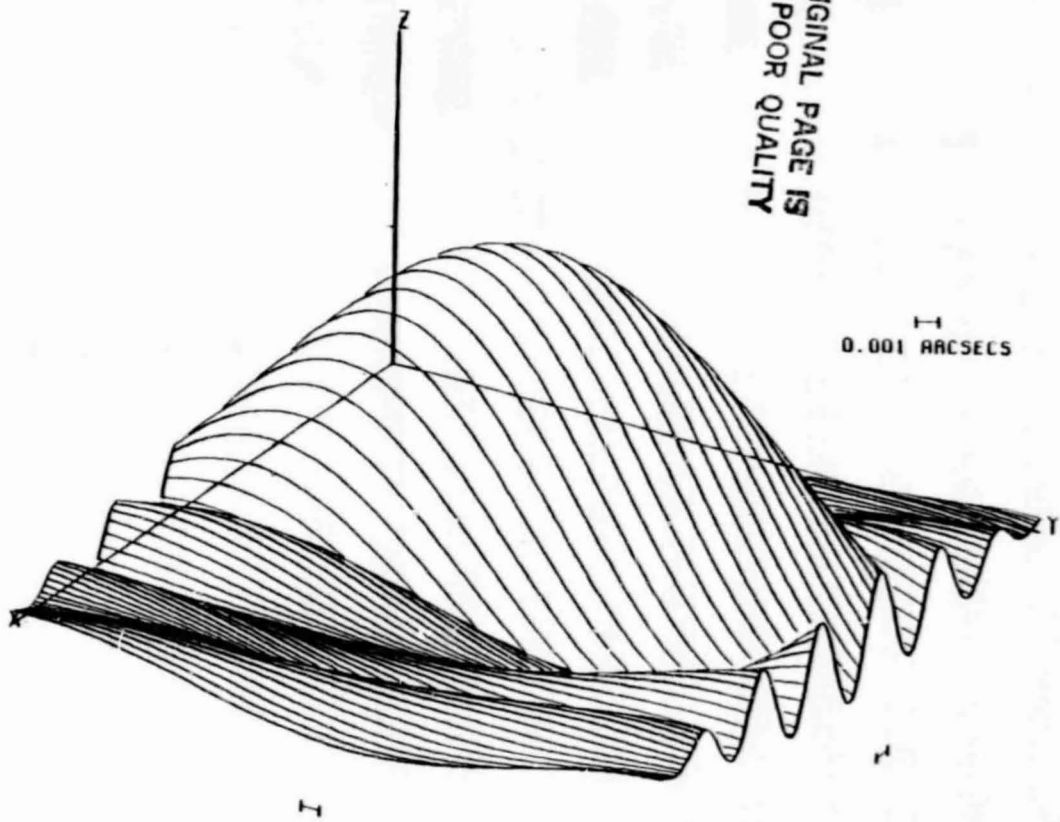
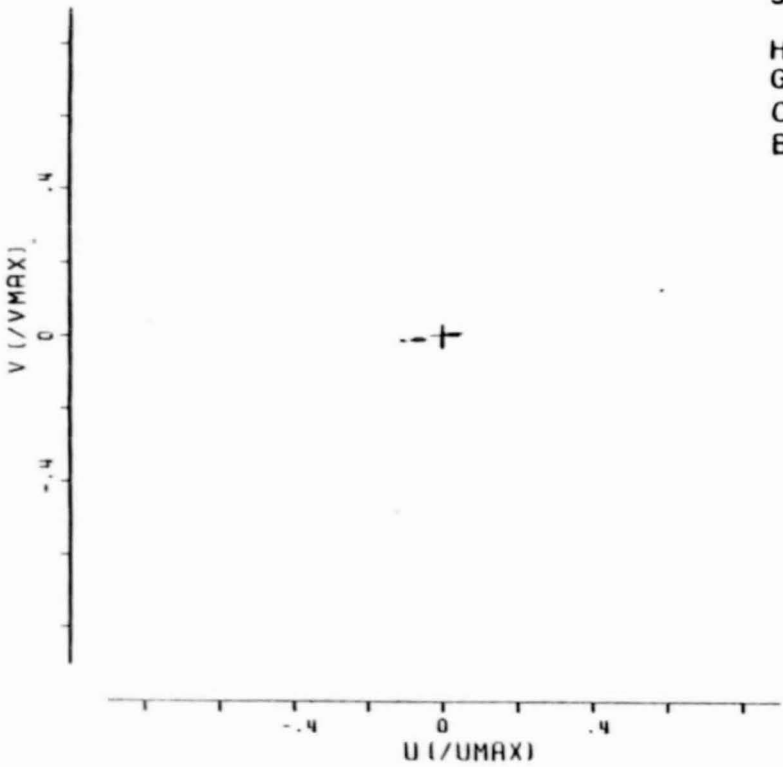
3C273  
 HSTK  
 GB  
 NLRO  
 OVRO



ORIGINAL PAGE IS  
 OF POOR QUALITY

Figure IV-3b

3C273  
HSTK  
GB  
OVRO  
BONN

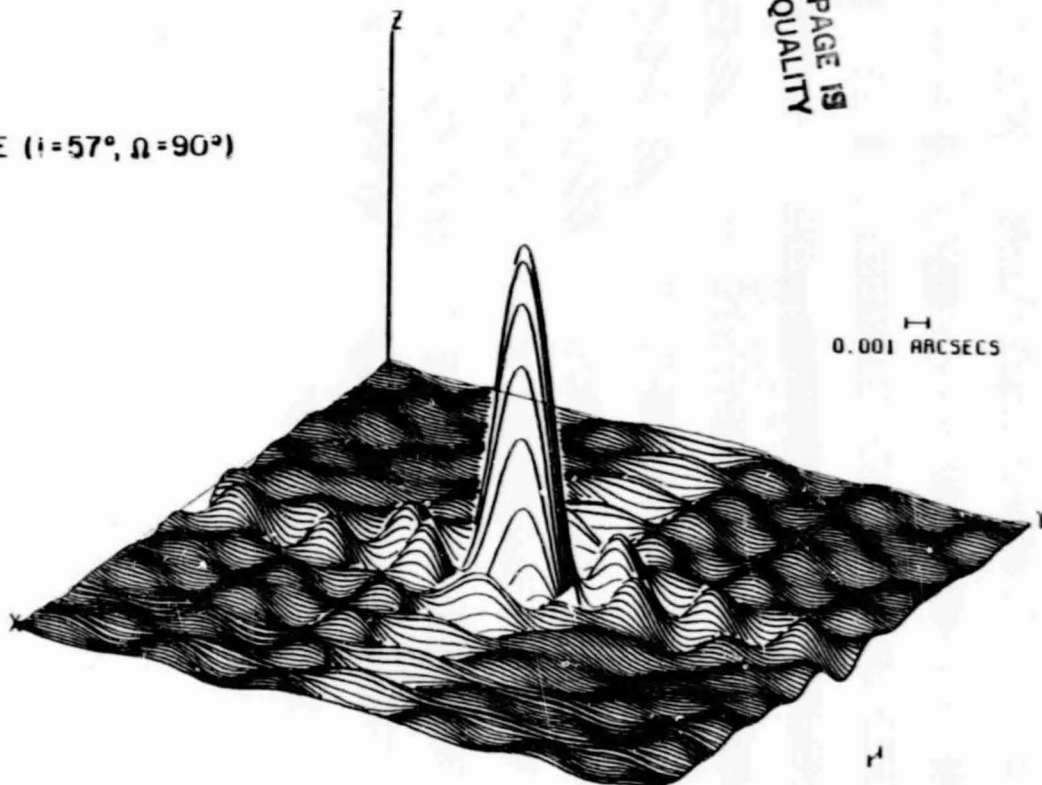
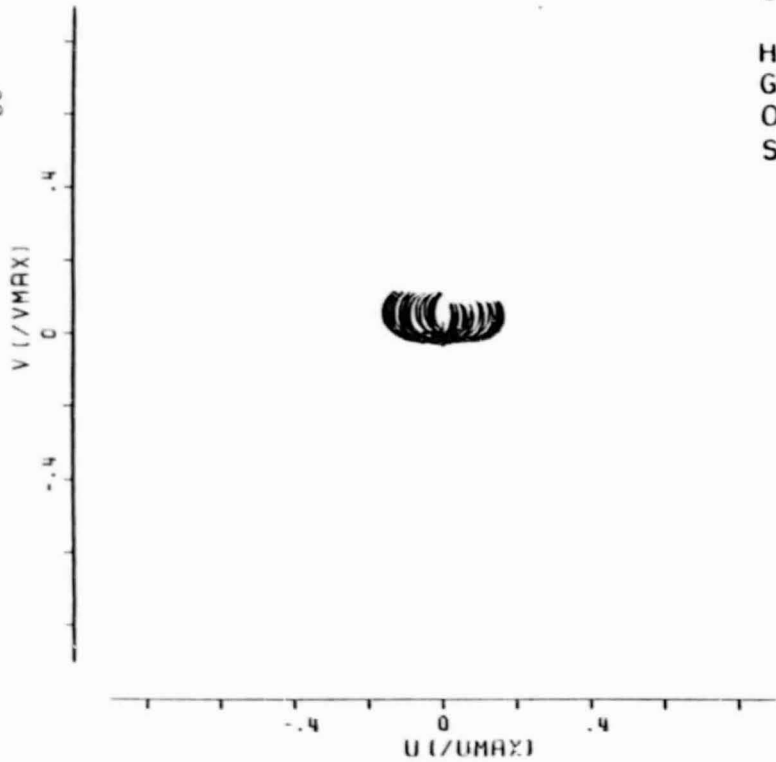


ORIGINAL PAGE IS  
OF POOR QUALITY

Figure IV-3c

3C273

HSTK  
GB  
OVRO  
SHUTTLE ( $i=57^\circ, \Omega=90^\circ$ )



ORIGINAL PAGE IS  
OF POOR QUALITY

Figure 1Y-3d

Figure IV-4. Fourier coverage and resulting synthesized beam from simulated VLB observations of the source W49. The angular scale assumes that the observing wavelength was 13 cm.

ORIGINAL PAGE IS  
OF POOR QUALITY

W49  
HSTK  
GB  
OVRO

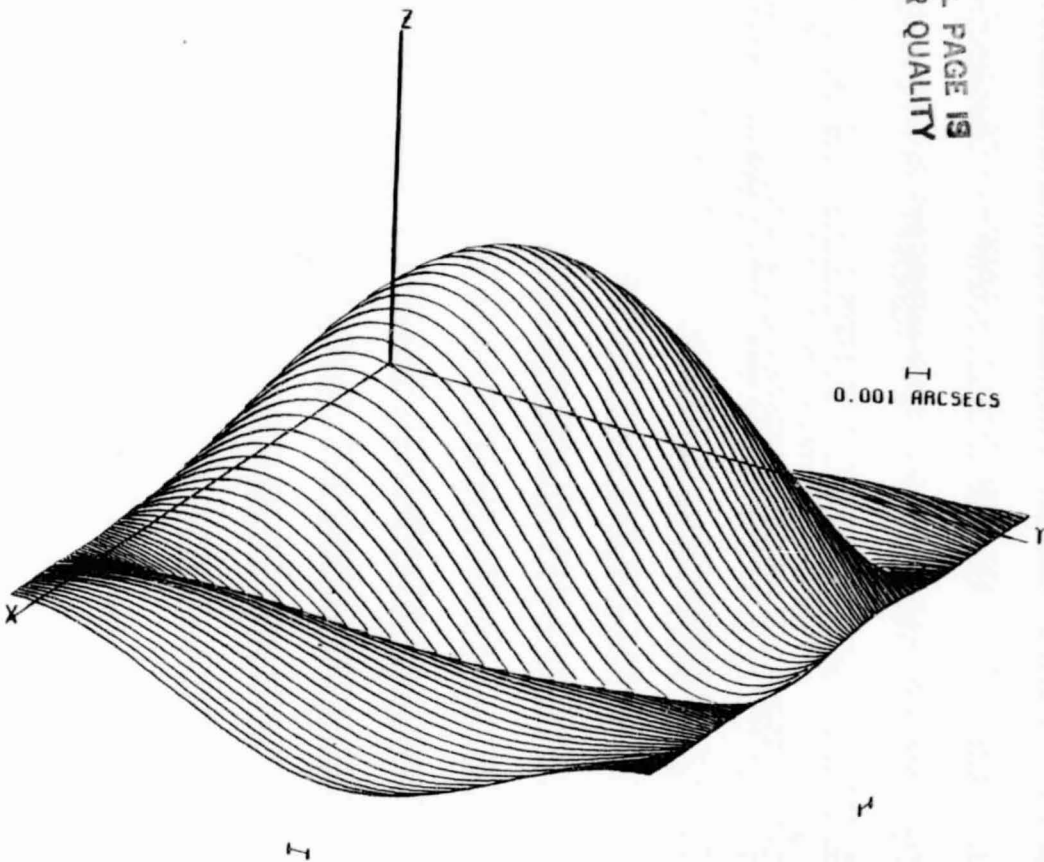
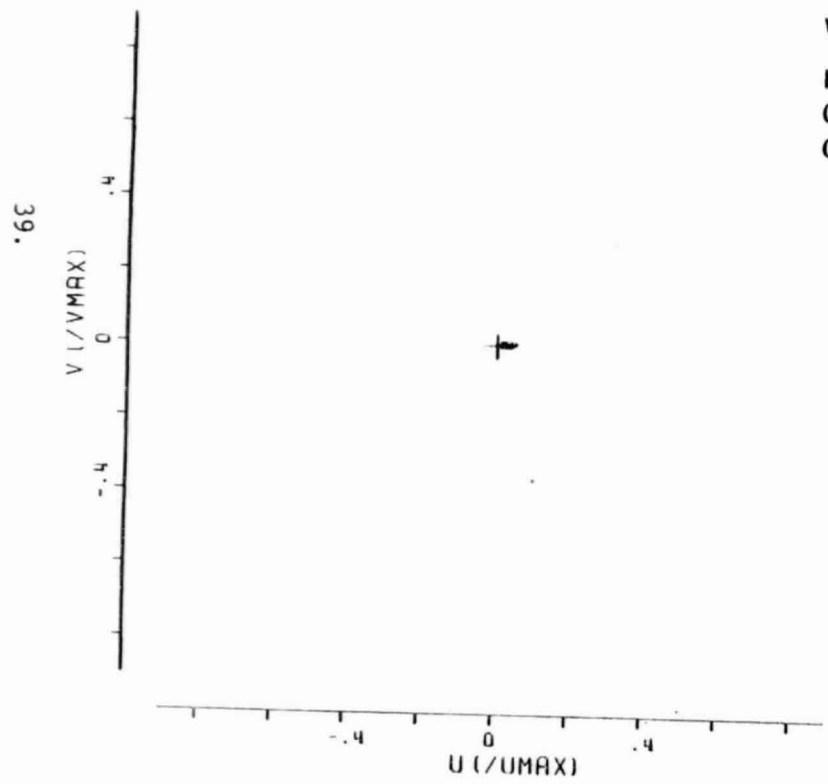
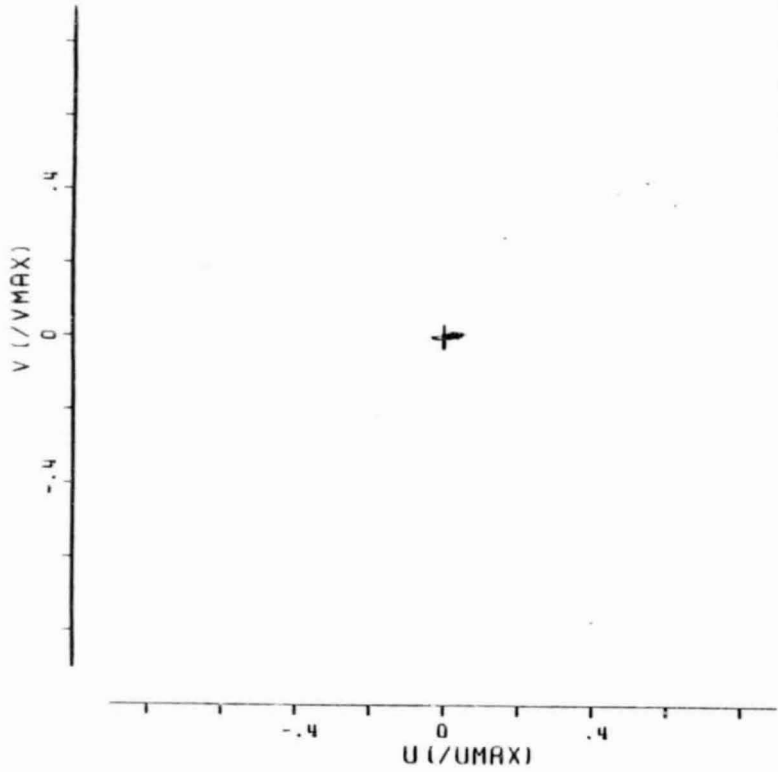
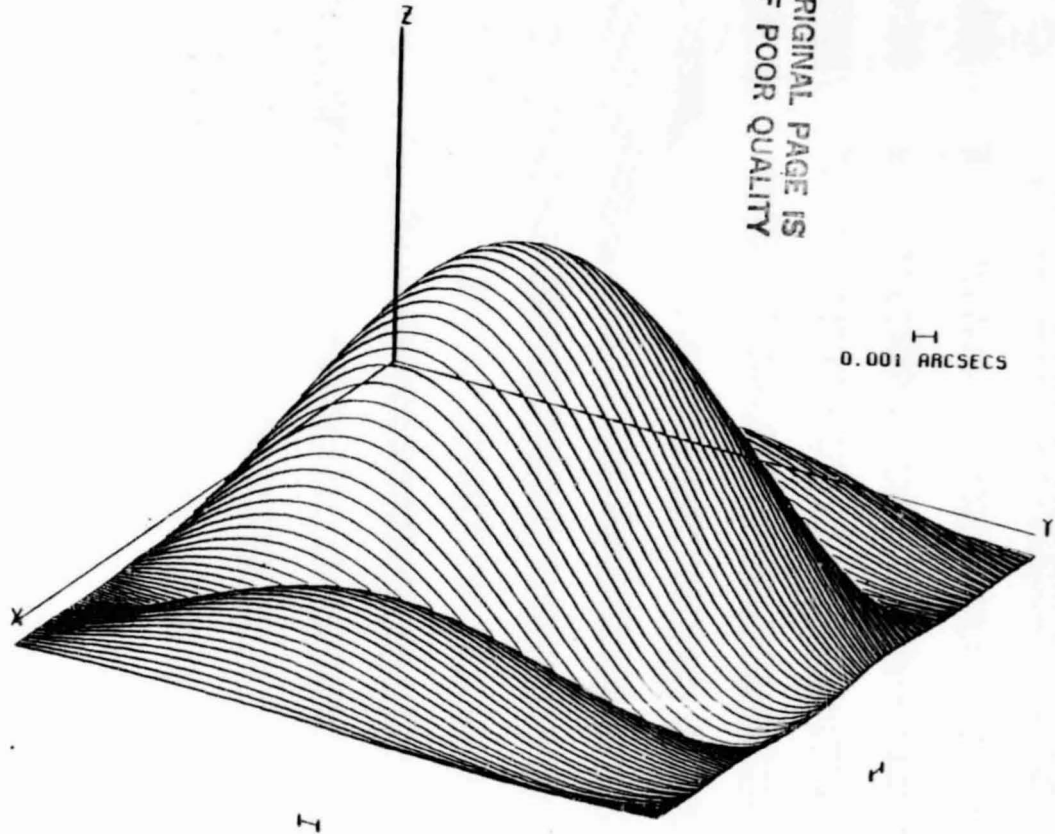


Figure IV-4a

40.



W49  
HSTK  
GB  
NLRO  
OVRO



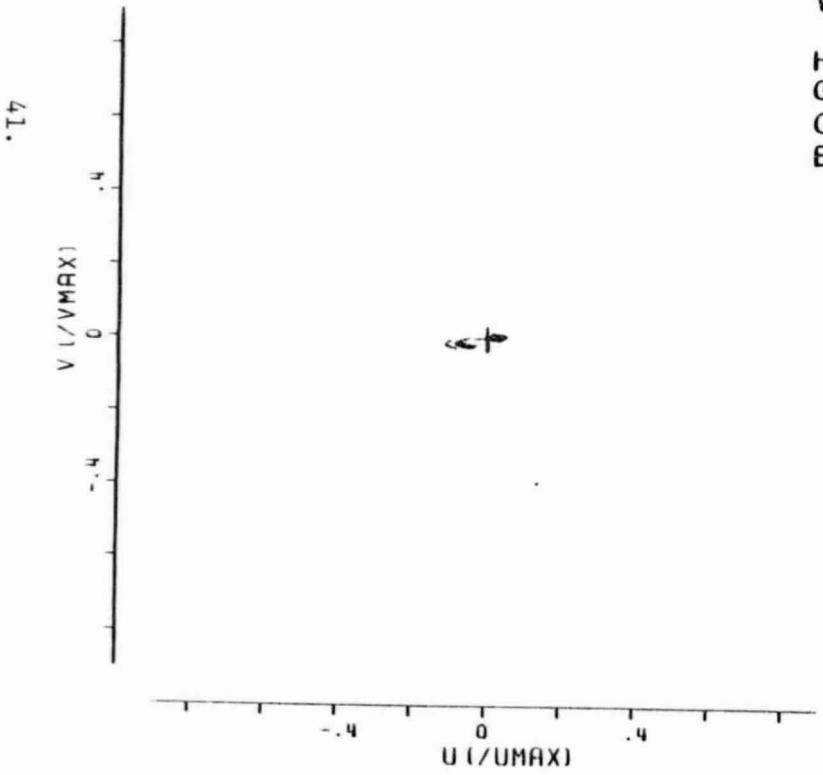
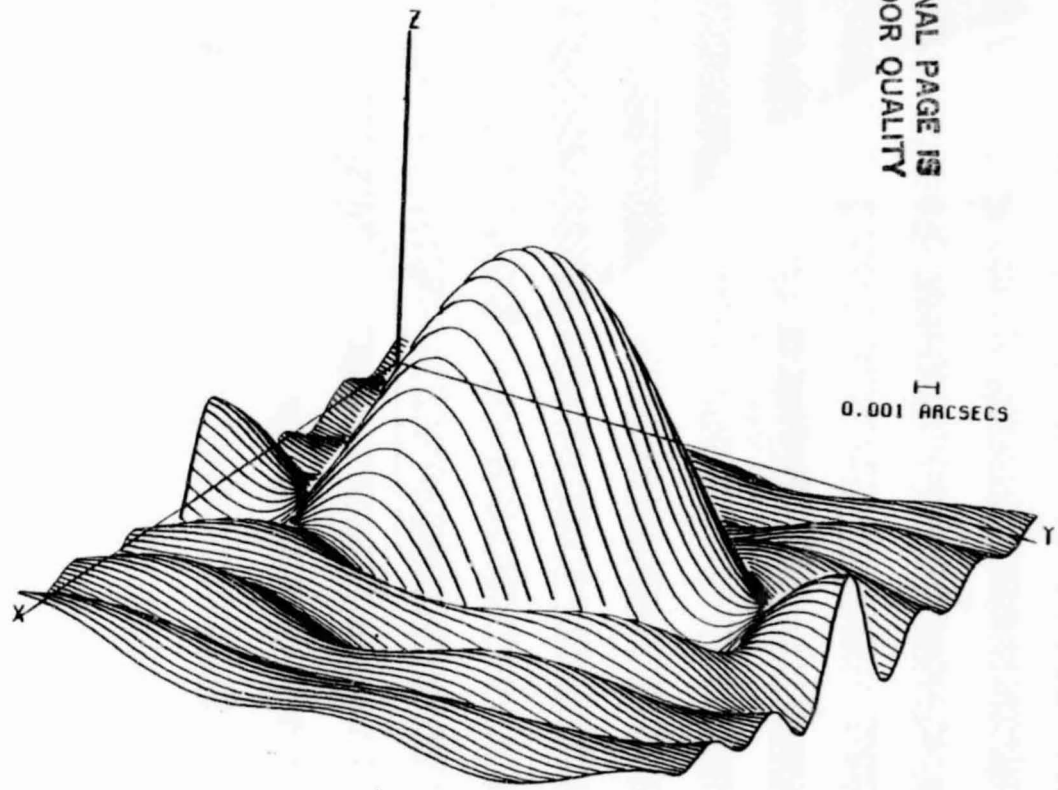
ORIGINAL PAGE IS  
OF POOR QUALITY

Figure IV-4b

ORIGINAL PAGE IS  
OF POOR QUALITY

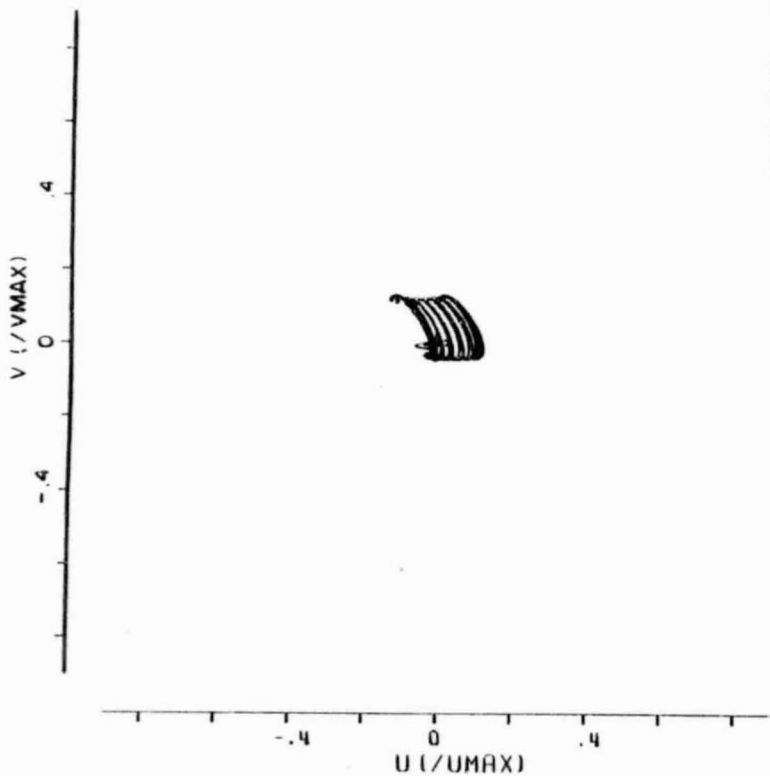
W49  
HSTK  
GB  
OVRO  
BONN

1  
0.001 ARCSECS

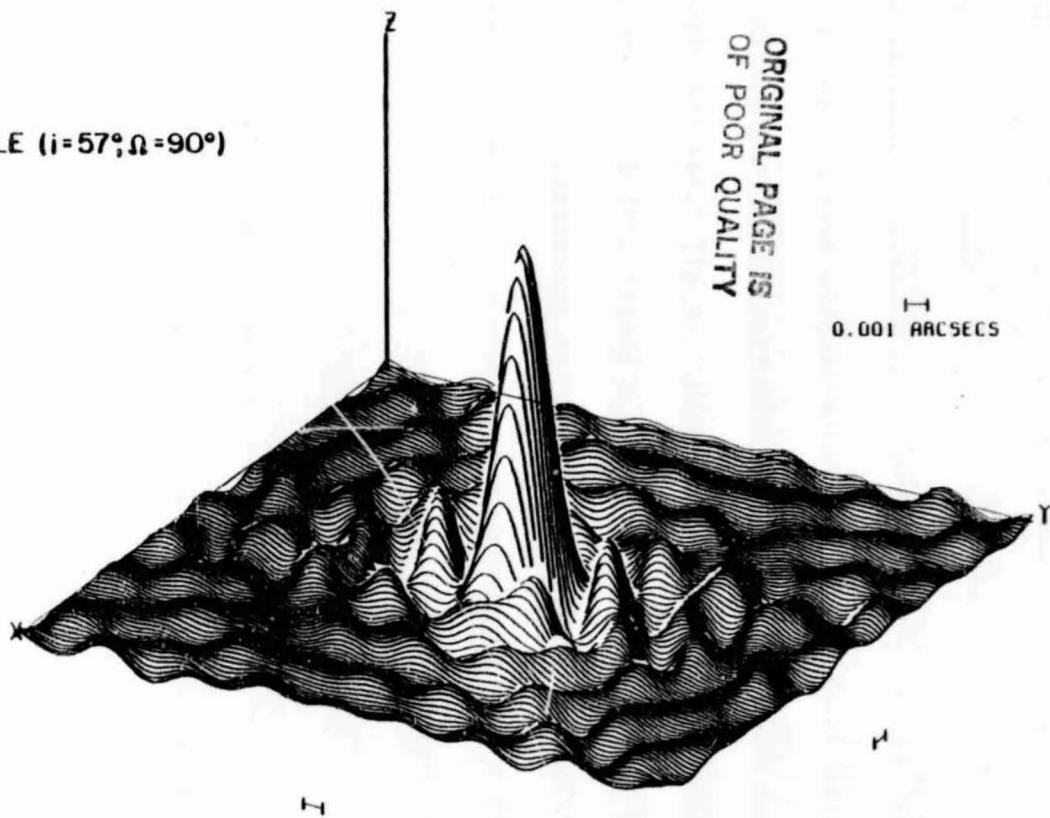


41.

Figure IV-4c



W49  
 HSTK  
 GB  
 OVRO  
 SHUTTLE ( $i=57^\circ; \Omega=90^\circ$ )



ORIGINAL PAGE IS  
 OF POOR QUALITY

Figure IV-4d

Summarizing this section, we conclude that the use of a single space antenna, in a high-inclination ( $i \approx 57^\circ$ ) but otherwise arbitrarily oriented ("Ω doesn't matter much") orbit results in dramatic improvement in the North-South resolution for low-declination sources, and in some increase the East-West resolution, and in a significant improvement in the density of the u-v coverage for all declinations. In all cases the simulations ran for one period of 24 hours. Had we chosen a longer period, the ground-ground tracks would be unchanged. However, because the spacecraft orbital period and a sidereal day are surely incommensurate, a second day would produce space-ground u-v tracks which differ from those produced the day before. The density of the u-v coverage can, in principle, be made as complete as desired in this way. This is a significant advantage over ground-based VLBI, and is independent of the number of ground antennas involved in a ground-ground synthesis. Orbital precession, considered more fully in Ch. VI, is only a small effect in these examples.

#### B. Comparison and Combination with a Dedicated Ground Array.

The idea of an array of about ten telescopes, at carefully chosen locations, dedicated to VLBI, (a Very Long Baseline Array, or VLBA), has been discussed by groups at NRAO (1981) and at Caltech (Cohen 1980). A proposal to build such a VLBA has been made to the NSF by NRAO. In this section we compare the properties of such a dedicated array with those of space VLBI. Because these two approaches to improving the current abilities of VLBI turn out to be quite complementary, we also discuss the combination of a VLBA with a space-borne antenna.

In Table IV-3 we summarize the simulations we have performed using a dedicated VLB array and various space stations. Fictitious sources at three declinations, corresponding to three equal-area sections of the Northern celestial hemisphere ( $\delta = 64^\circ, 30^\circ, \text{ and } 6^\circ$ ), were assigned  $\alpha = 12^{\text{h}}$  -- these choices were made to facilitate direct comparison with the Caltech study. Each source was "observed" for 24 hours with a set of ten ground stations - -

TABLE IV-3

Simulations with a Dedicated VLB Ground Array  
and Various Space VLBI Stations

<u>Figure</u>	$\delta$ <u>Source (<math>\alpha=12^h</math>)</u>	<u>Ground Stations*</u>	<u>Space VLB Terminal**</u>	
			<u>i</u>	<u><math>\Omega</math></u>
5a	+64°	Network #13	-	-
5b	+64°	HSTK, GB, OVRO	57°	0°
5c	+64°	HSTK, GB, OVRO	57°	270°+
5d	+64°	HSTK, GB, OVRO	26°+	270°+
5e	+64°	Network #13	57°	0°
5f	+64°	Network #13	57°	270°+
6a	+30°	Network #13	-	-
6b	+30°	HSTK, GB, OVRO	57°++	0°
6c	+30°	HSTK, GB, OVRO	57°++	270°+
6d	+30°	Network #13	57°++	0°
6e	+30°	Network #13	57°++	270°+
7a	+ 6°	Network #13	-	-
7b	+ 6°	HSTK, GB, OVRO	57°	0°
7c	+ 6°	HSTK, GB, OVRO	57°	270°+
7d	+ 6°	Network #13	57°	0°
7e	+ 6°	Network #13	57°	270°+

\*In all cases the space antenna is in a circular orbit at an altitude of 370 km.

\*\*HSTK = Haystack Observatory, Westford, MA

GB = NRAO, Green Bank, W. VA.

OVRO = Owens Valley Radio Observatory, Big Pine, CA.

Network #13 = VLB Array #13 (Cohen 1980).

+ = optimum value for this parameter.

++ = near-optimum value.

the "Network 13" chosen as roughly optimal in the Caltech study -- as well as with various combinations of space antenna orbits and ground stations. The resulting u-v coverage and synthesized beams are presented in Figures IV-5, IV-6, and IV-7. In all cases the observing wavelength was chosen to be that of the Caltech study,  $\lambda$  2.8 cm.

The high declination source ( $\alpha = 12^h$ ,  $\delta = +64^\circ$ ), observed by the dedicated array "Network 13", results in the u-v coverage and beam shown in Figure IV-5a. It is clear that the array functions exactly as designed -- the coverage is very dense, and the North-South and East-West resolutions are comparable, as expected for a high-declination source. In Figure IV-5b we contrast this with the results of a three-ground-station, single-space-station observation, with the orbit chosen to be "edge-on". Comparison with the previous Figure shows one advantage of space VLBI -- the maximum baseline is about 50% larger than that obtained with a VLBA. In Figure IV-5c and IV-5d we change the spacecraft orbit to have, first, the optimal  $\Omega$ , and second, the optimal  $\Omega$  and the optimal  $i$ . Comparison of these two Figures with the previous one shows that a considerable decrease in sidelobe level is possible if the spacecraft orbit is chosen "properly". However, comparison with Figure IV-5a shows that the density of the u-v coverage afforded by an array of ten ground antennas cannot be achieved by three ground antennas and a single space antenna (at least not in a single 24 hour observation).

In order to make use of the large baselines available from space and the density of u-v coverage afforded by a dedicated ground array, we have simply combined the two. For an "edge-on" orbit, the results are shown in Figure IV-5e, and for an optimal  $\Omega$  (but not optimal  $i$ ) orbit they are shown in Figure IV-5f. The best features of each approach are realized in their combination -- the

Figure IV-5. Fourier coverage and synthesized beam from simulated VLB observations of a source at  $\alpha = 12^{\text{h}}$ ,  $\delta = +64^{\circ}$ . The angular scale corresponds to an observing wavelength of 2.8 cm. ( $\nu = 10.665$  GHz).

ORIGINAL PAGE IS  
OF POOR QUALITY

$\alpha = 12^h, \delta = +64^\circ$   
NTWK #13

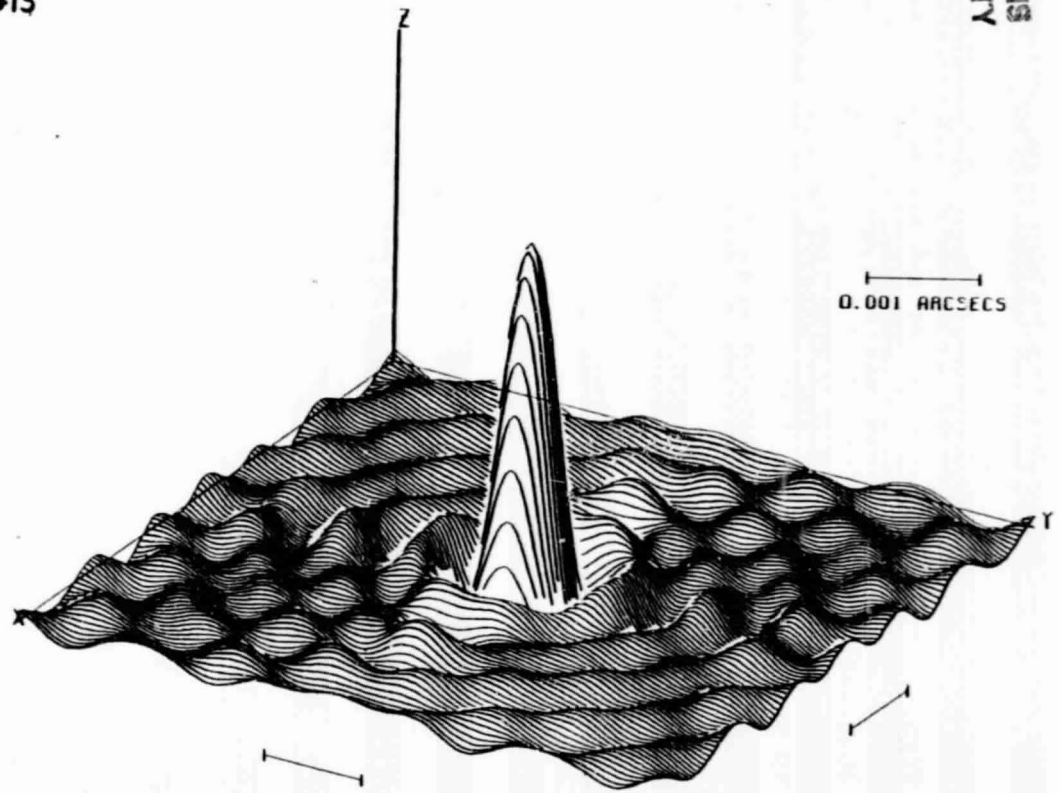
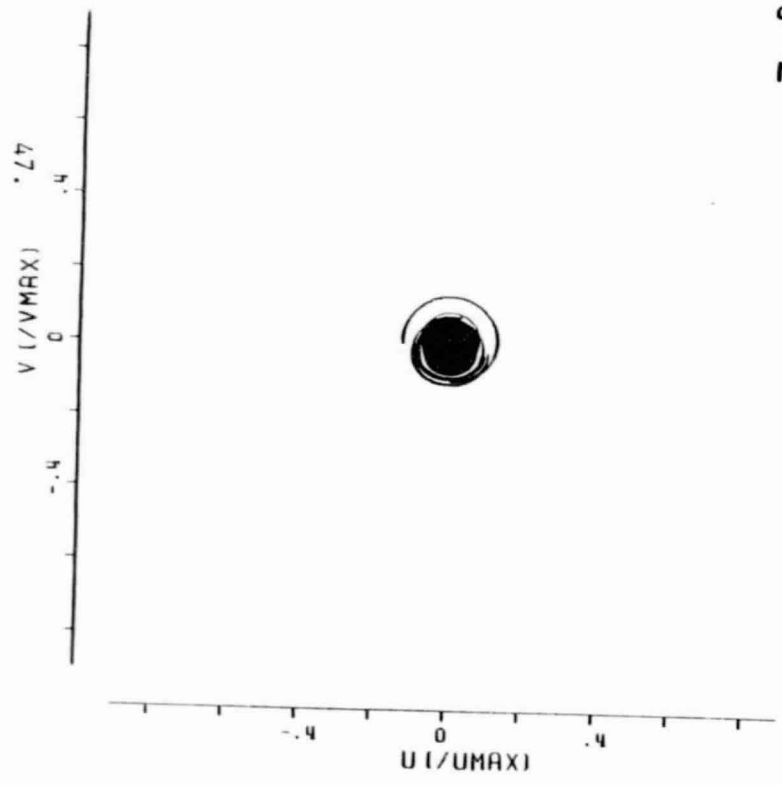
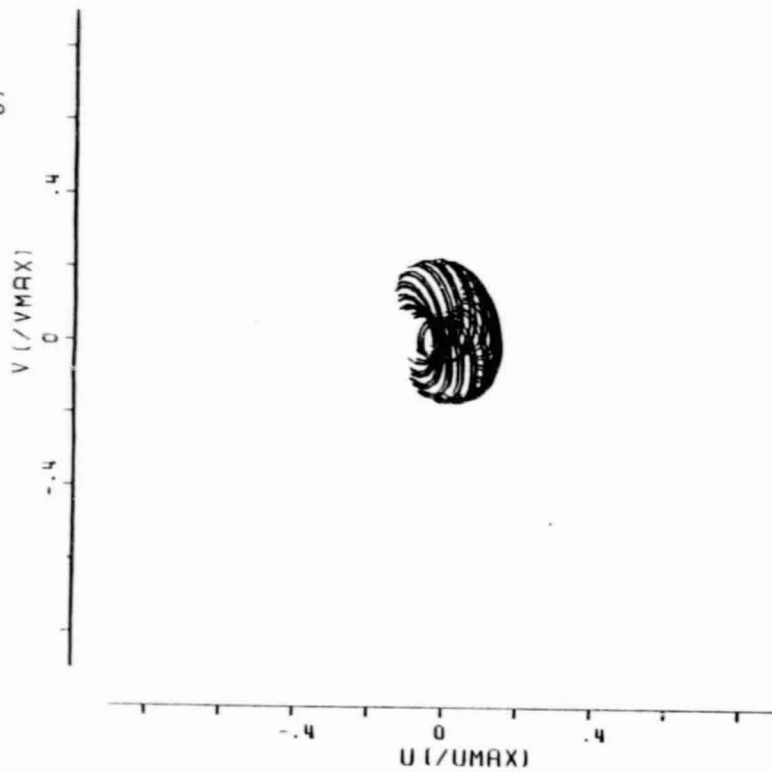
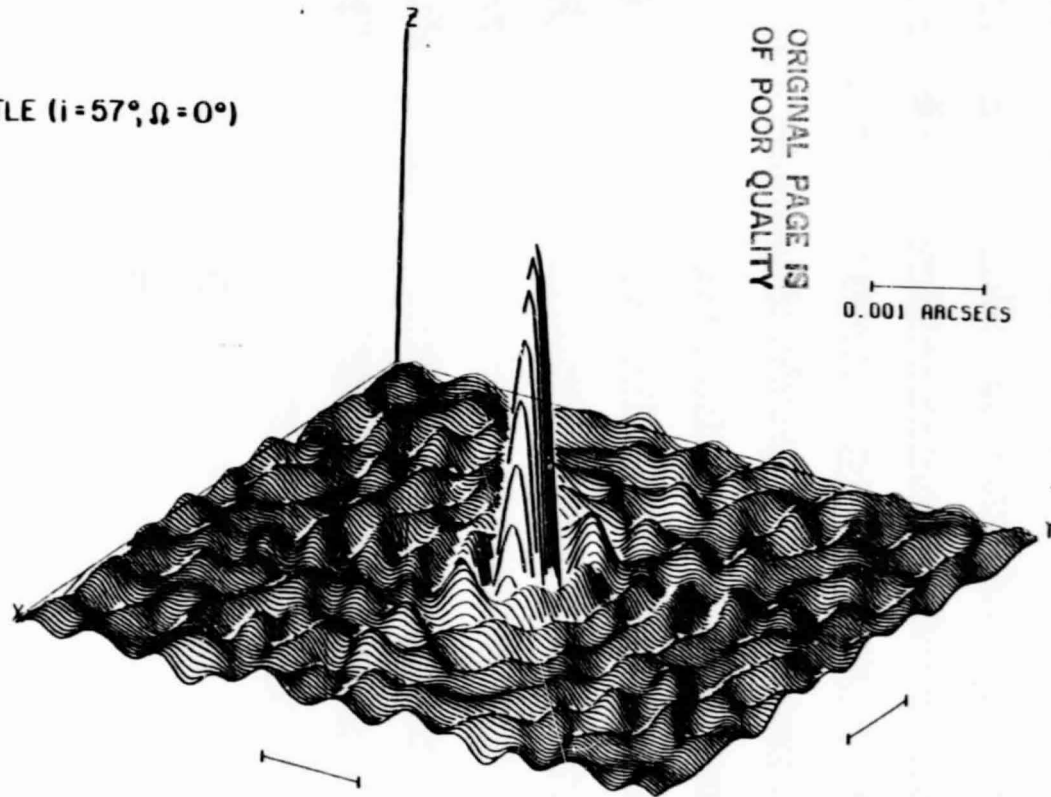


Figure IV-5a



$$\alpha = 12^h, \delta = +64^\circ$$

HSTK  
GB  
OVRO  
SHUTTLE ( $i = 57^\circ, \Omega = 0^\circ$ )

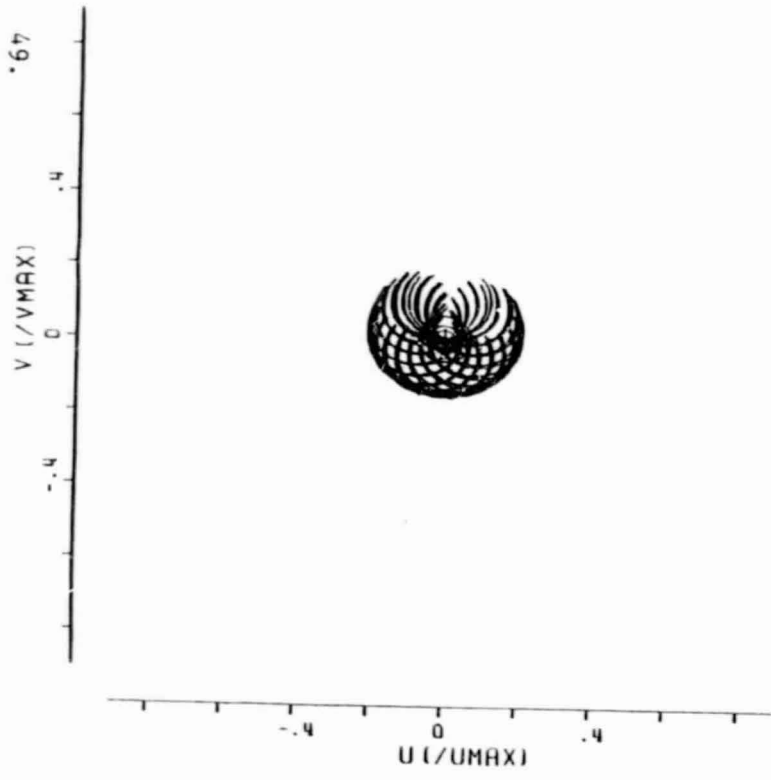


ORIGINAL PAGE IS  
OF POOR QUALITY

0.001 ARCSECS

Figure IV-5b

ORIGINAL PAGE IS  
OF POOR QUALITY



$\alpha = 12^h, \delta = +64^\circ$   
HSTK  
GB  
OVRO  
SHUTTLE ( $i = 57^\circ, \Omega = 270^\circ$ )

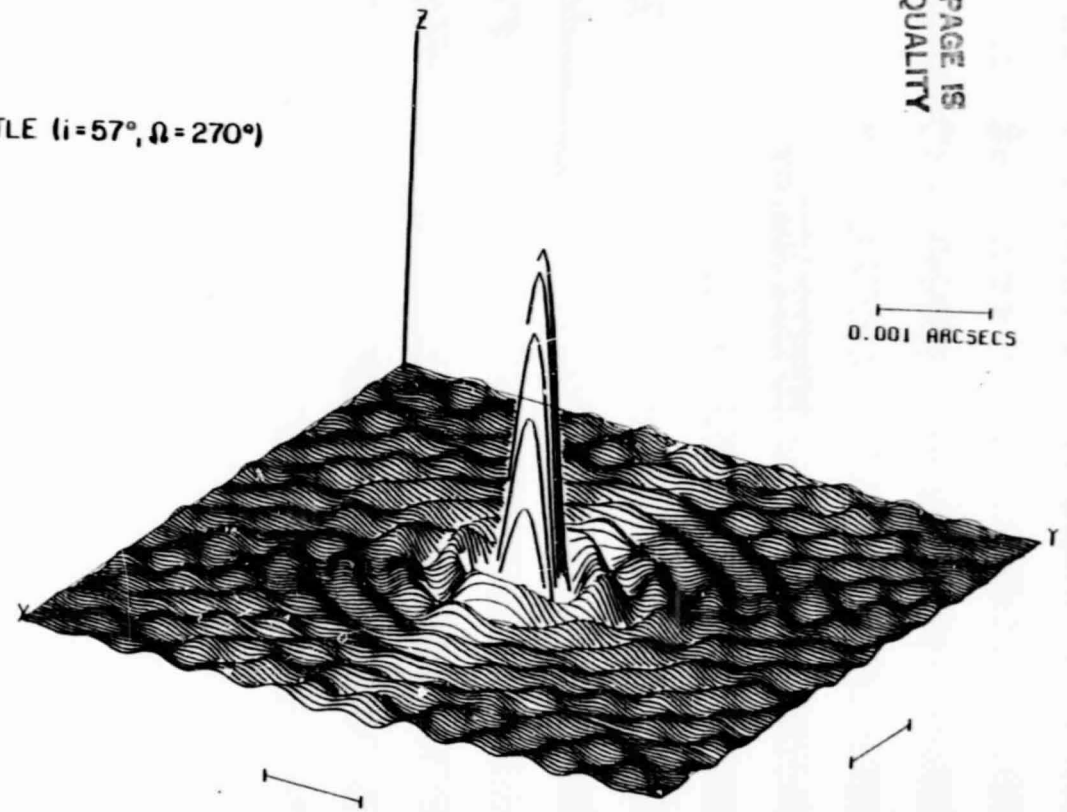
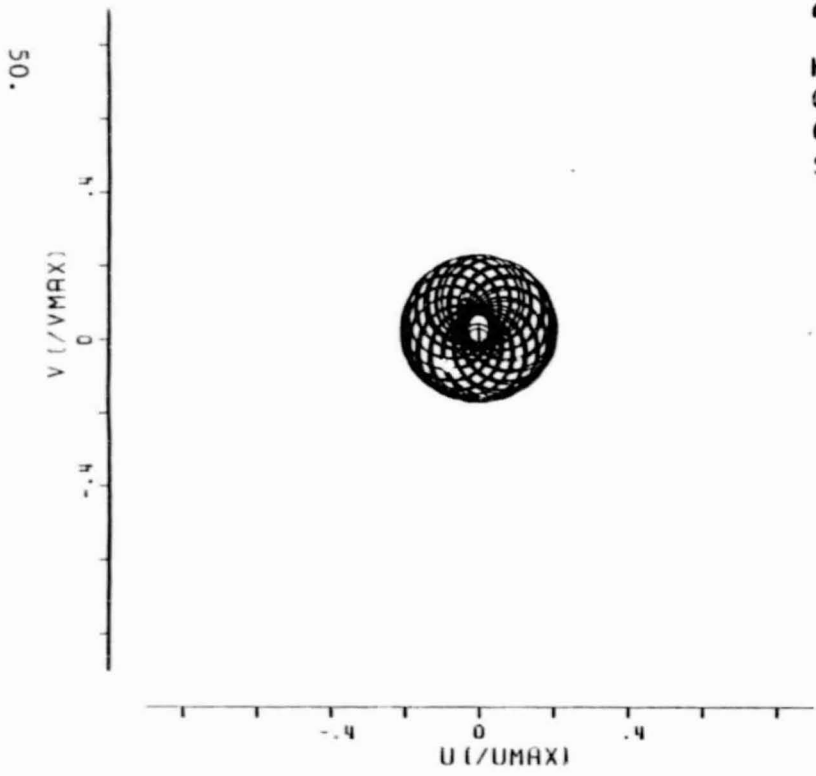


Figure IV-5c



$\alpha = 12^h, \delta = +64^\circ$

HSTK  
 GB  
 OVRO  
 SHUTTLE ( $i = 26^\circ, \Omega = 270^\circ$ )

ORIGINAL PAGE IS  
 OF POOR QUALITY

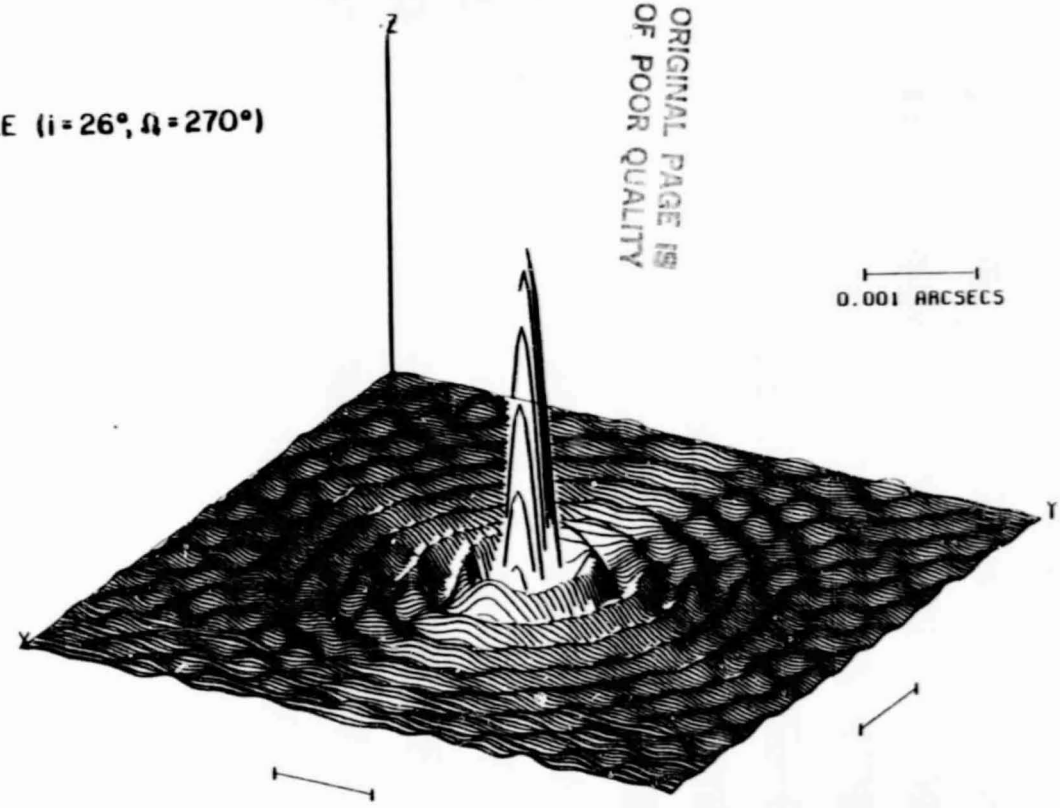
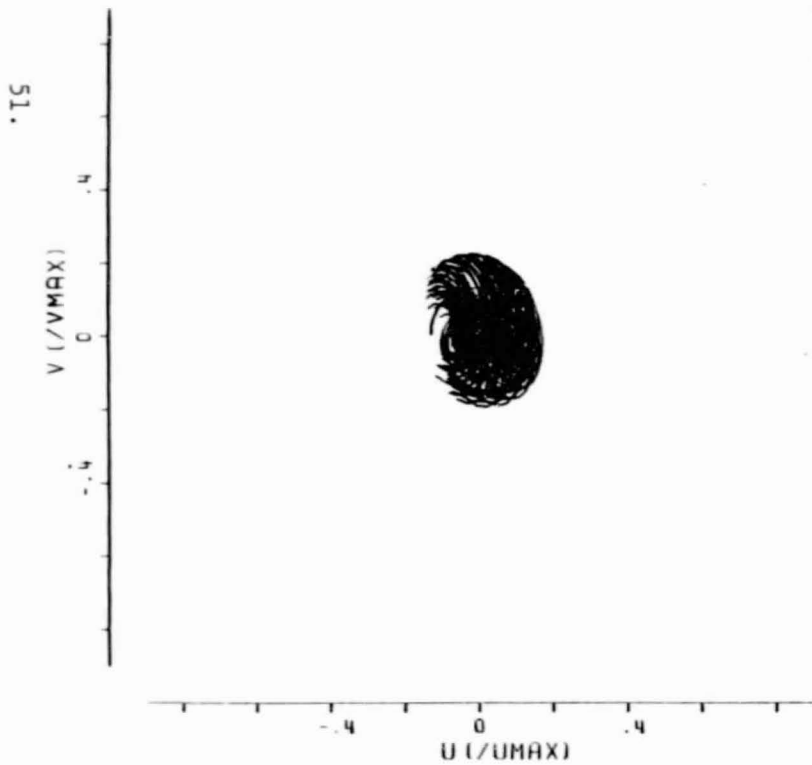


Figure IV-5d



$\alpha = 12^\circ, \beta = +64^\circ$   
 NTWK #13  
 SHUTTLE ( $i = 57^\circ, \Omega = 0^\circ$ )

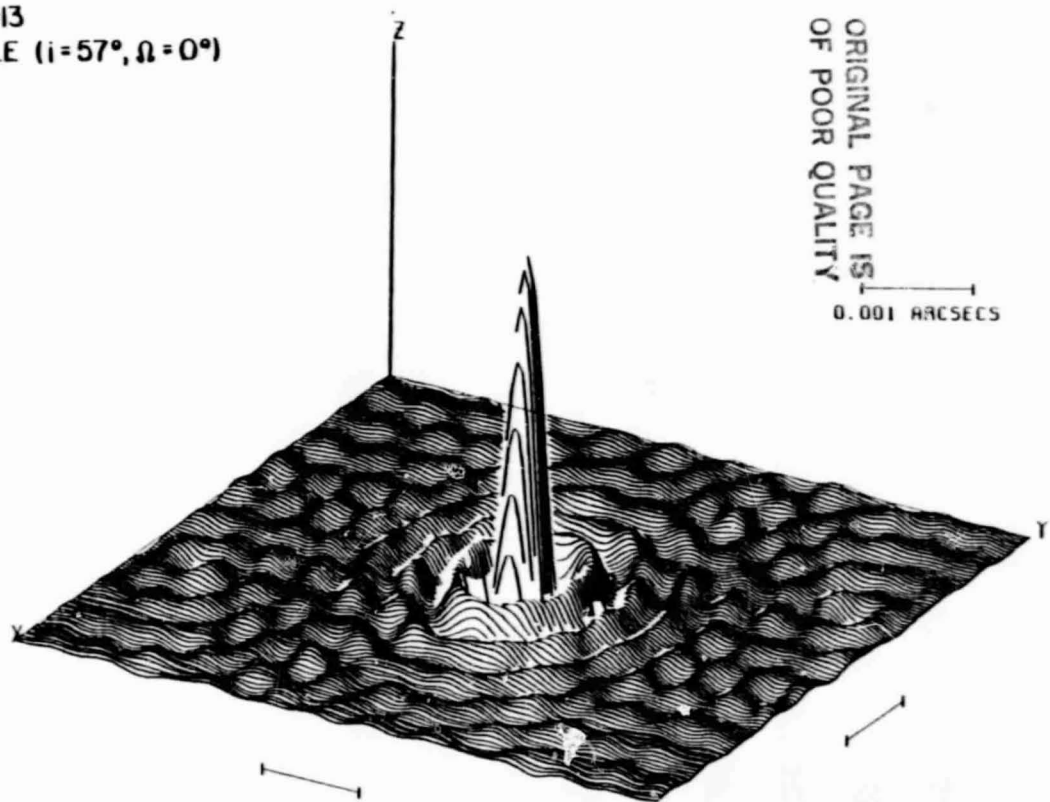
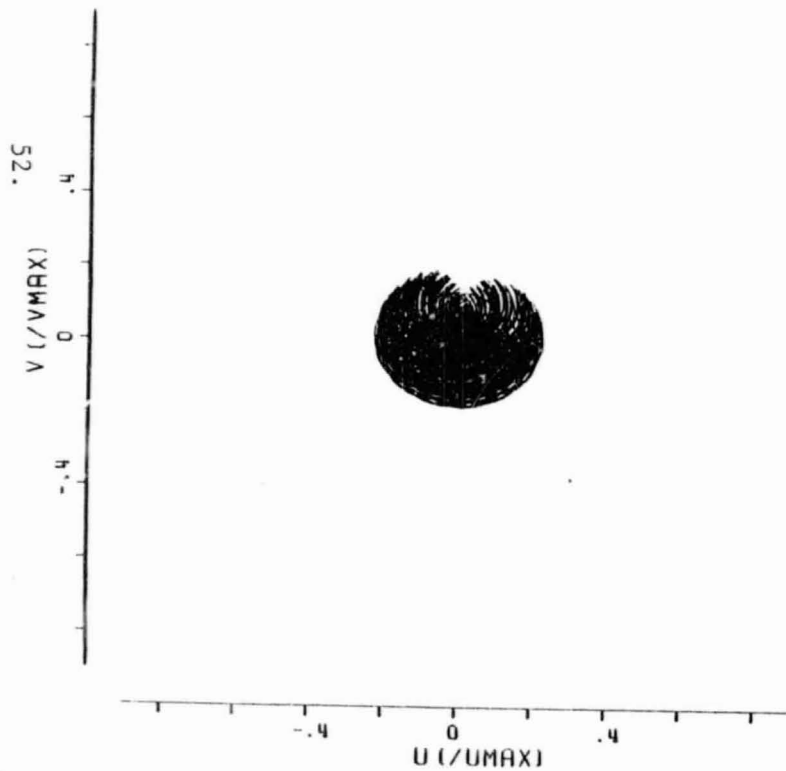


Figure IV-5e



$\alpha = 12^{\circ}, \delta = +64^{\circ}$   
 NTWK #13  
 SHUTTLE ( $i = 57^{\circ}, \Omega = 270^{\circ}$ )

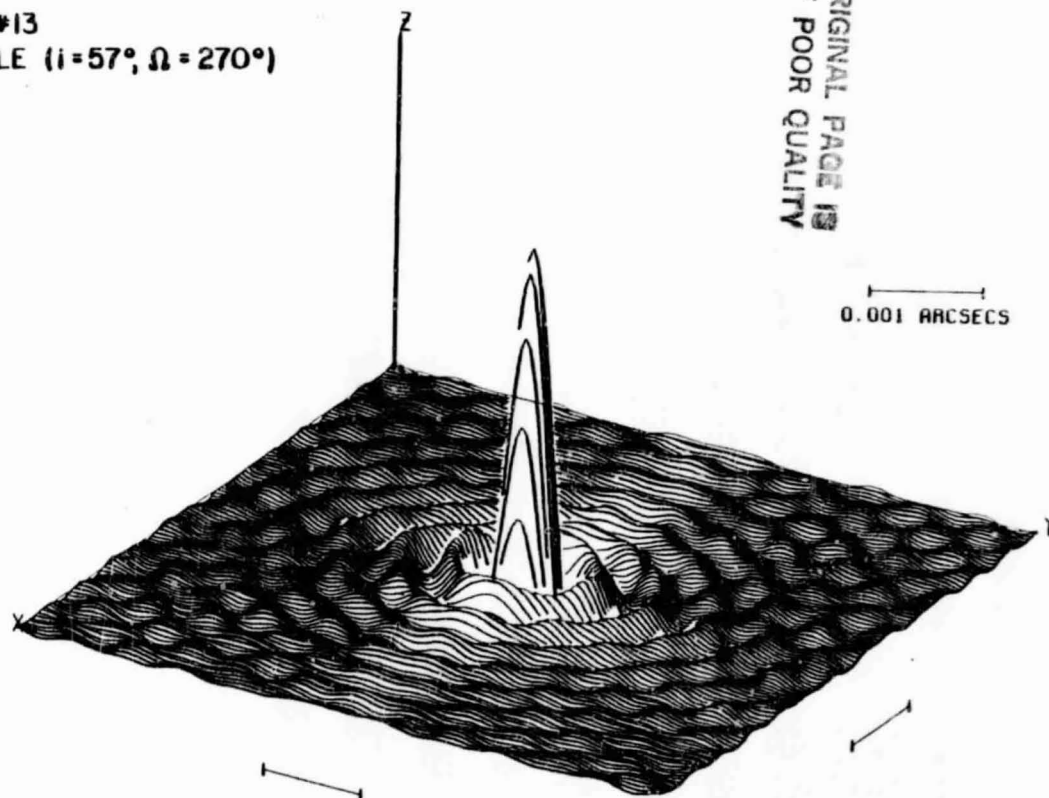
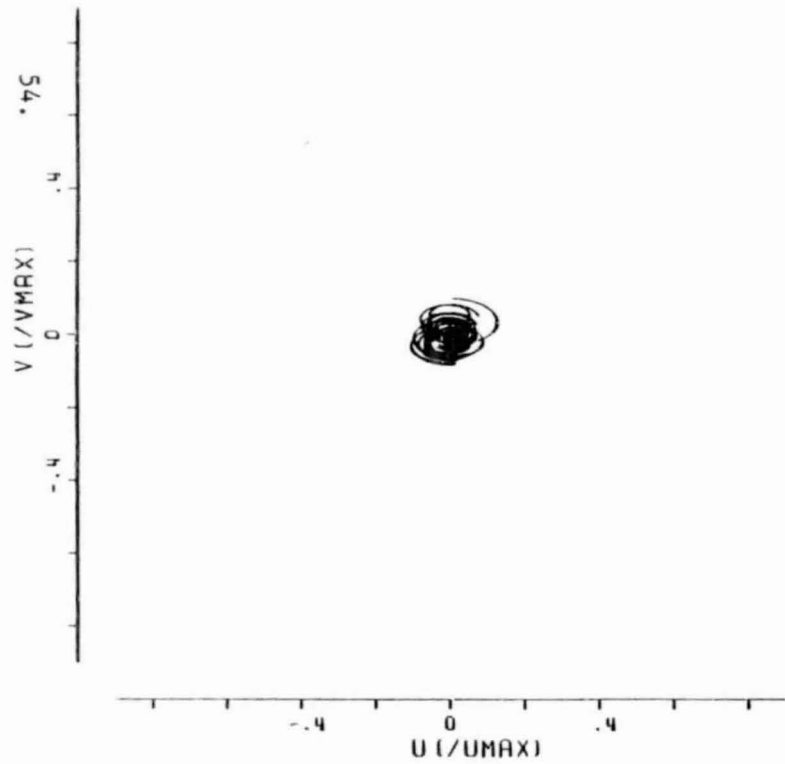


Figure IV-5f

Figure IV-6. Fourier coverage and synthesized beam from simulated VLB observations of a source at  $\alpha = 12^{\text{h}}$ ,  $\delta = + 30^{\circ}$ . The angular scale corresponds to an observing wavelength of 2.8 cm.



$\alpha = 12^h, \delta = +30^\circ$

NTWK #13

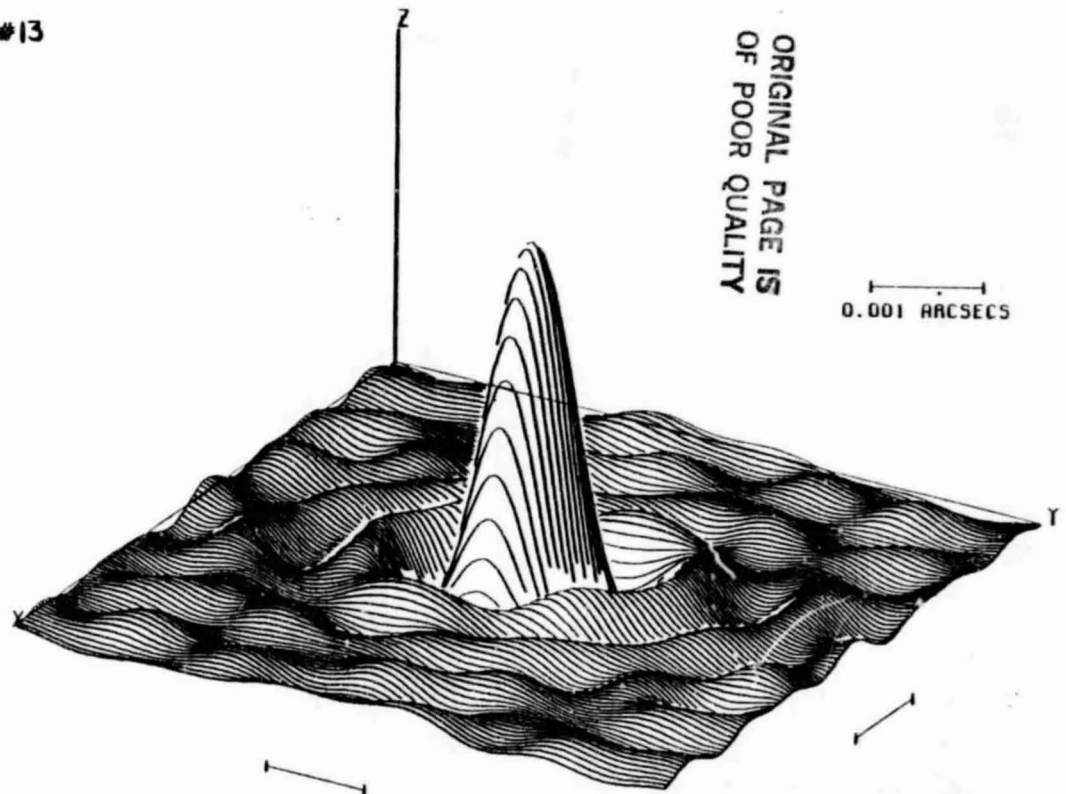
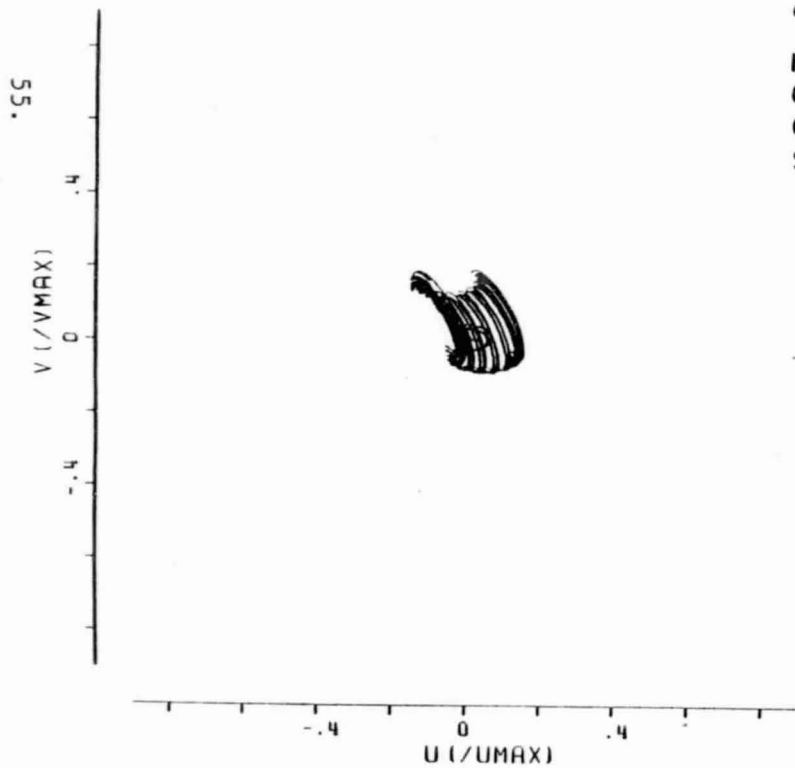


Figure IV-6a



$\alpha = 12^h, \delta = +30^\circ$   
 HSTK  
 GB  
 OVRO  
 SHUTTLE ( $i = 57^\circ, \Omega = 0^\circ$ )

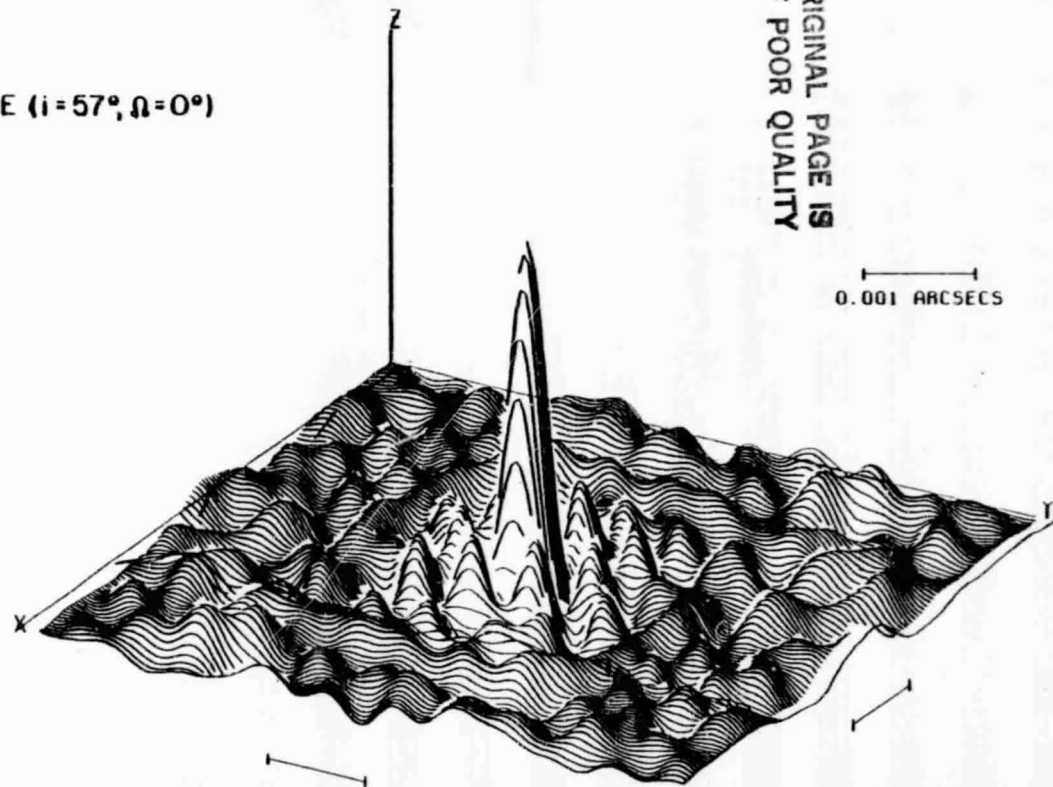
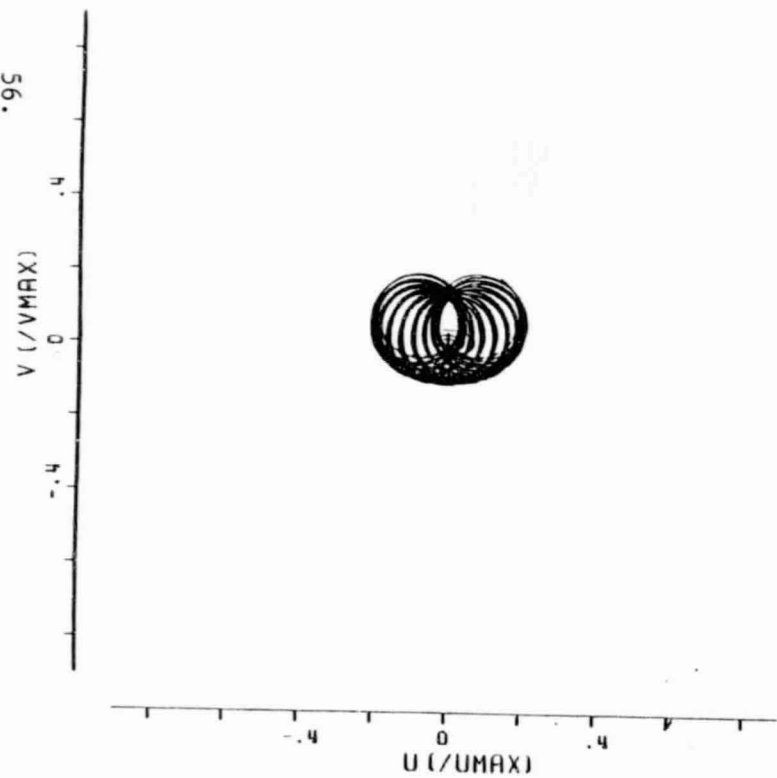
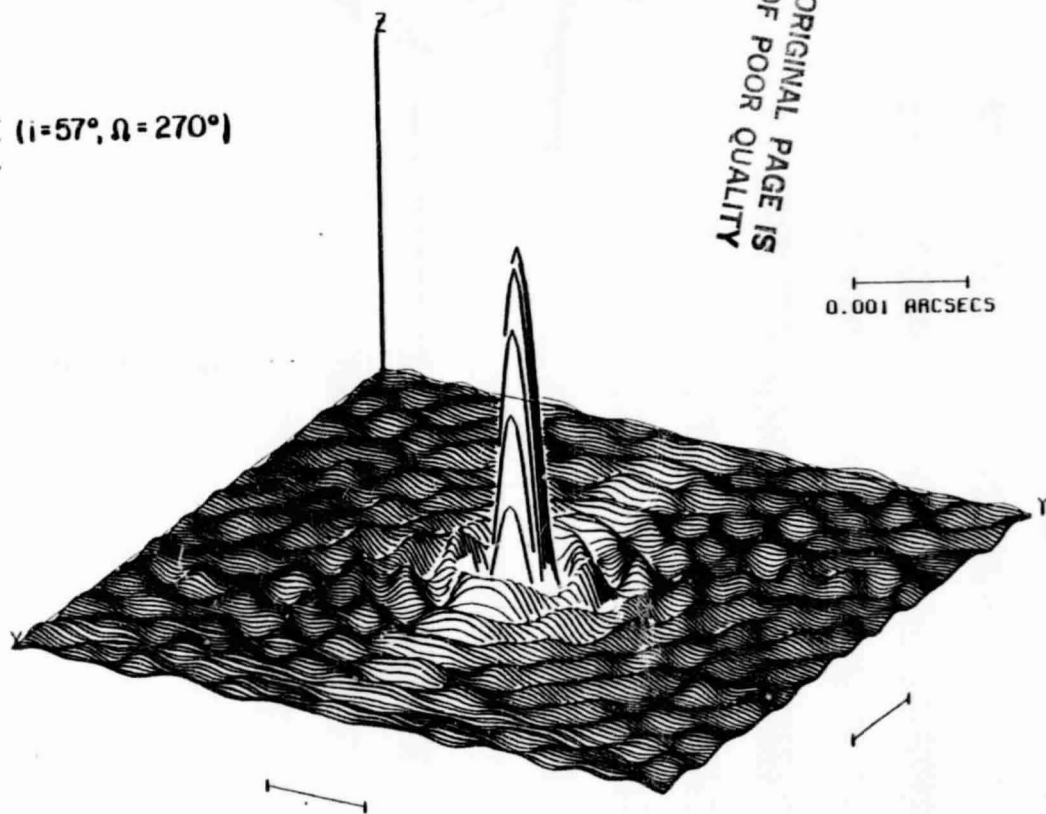


Figure IV-6b



$$\alpha = 12^h, \delta = +30^\circ$$

HSTK  
GB  
OVRO  
SHUTTLE ( $i=57^\circ, \Omega=270^\circ$ )



ORIGINAL PAGE IS  
OF POOR  
QUALITY

0.001 ARCSECS

Figure IV-6c

$\alpha = 12^h, +30^\circ$   
NTWK #13  
SHUTTLE ( $\delta = 57^\circ, \Omega = 0^\circ$ )

ORIGINAL PAGE IS  
OF POOR QUALITY

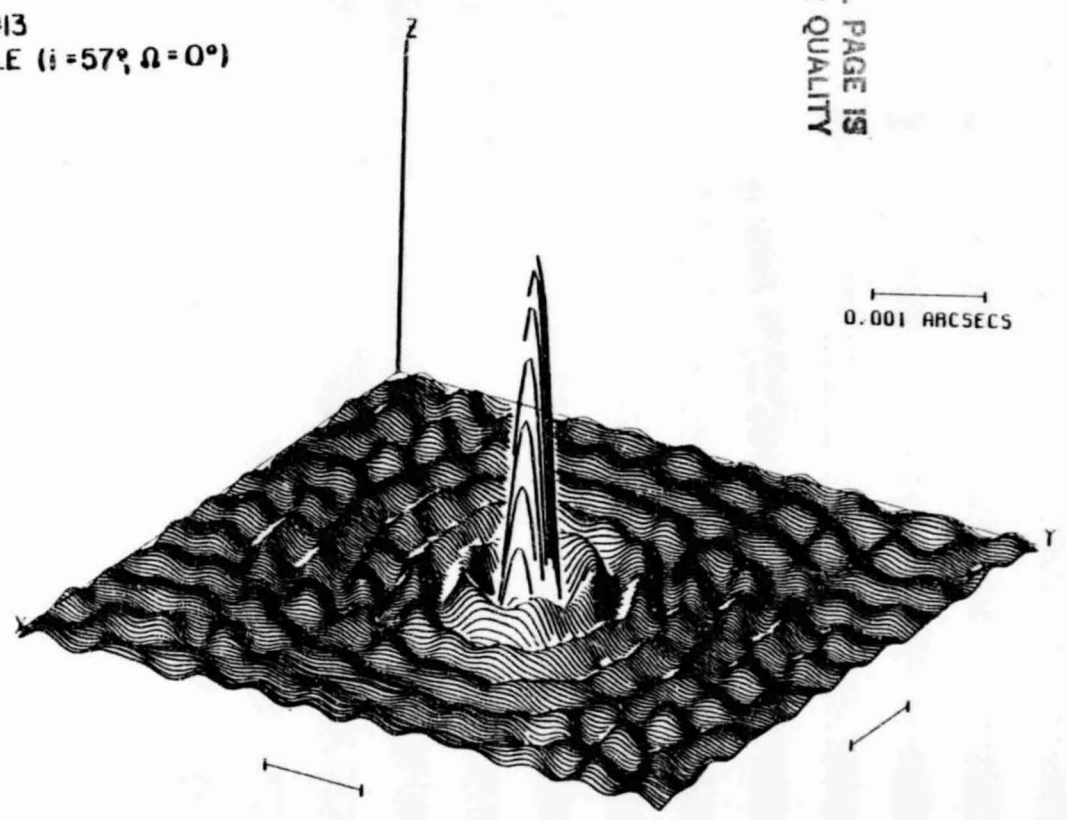
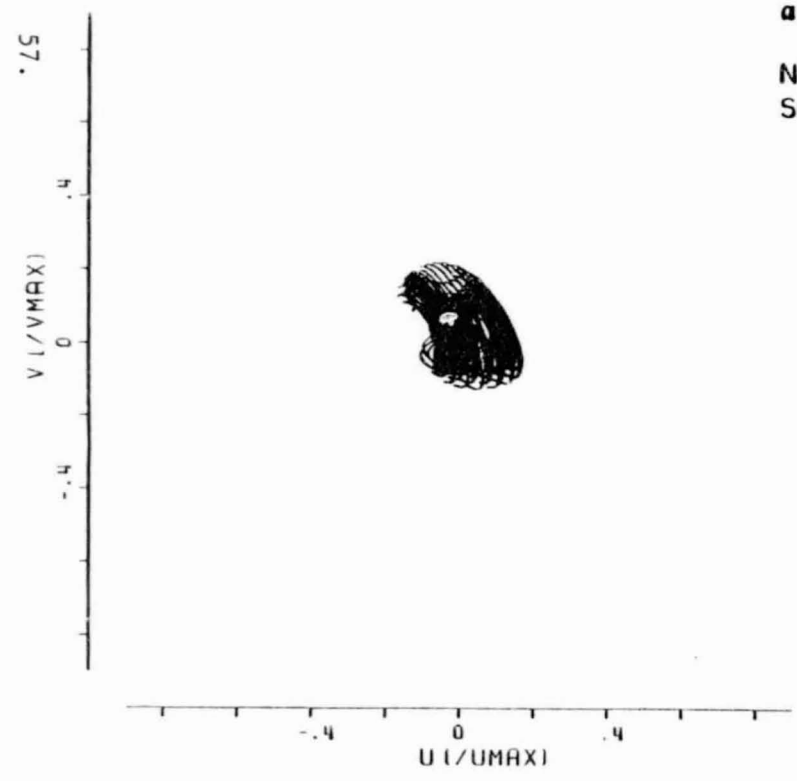
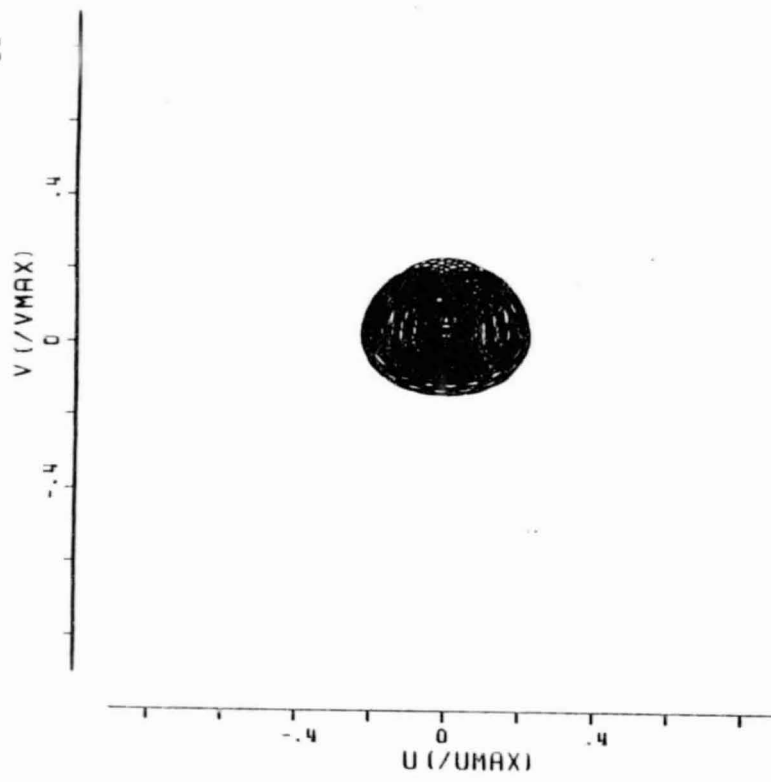
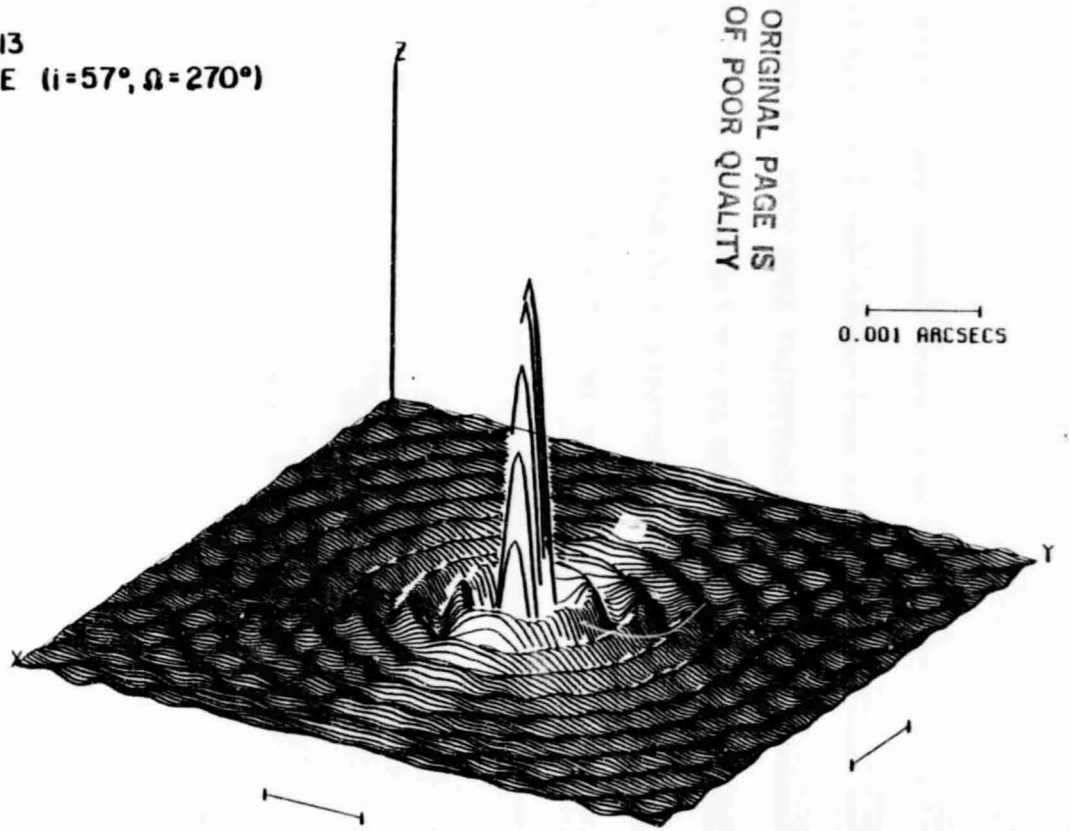


Figure IV-6d



$\alpha = 12^\circ, \beta = +30^\circ$   
NTWK #13  
SHUTTLE ( $i = 57^\circ, \Omega = 270^\circ$ )



ORIGINAL PAGE IS  
OF POOR QUALITY

0.001 ARCSECS

Figure IV-6e

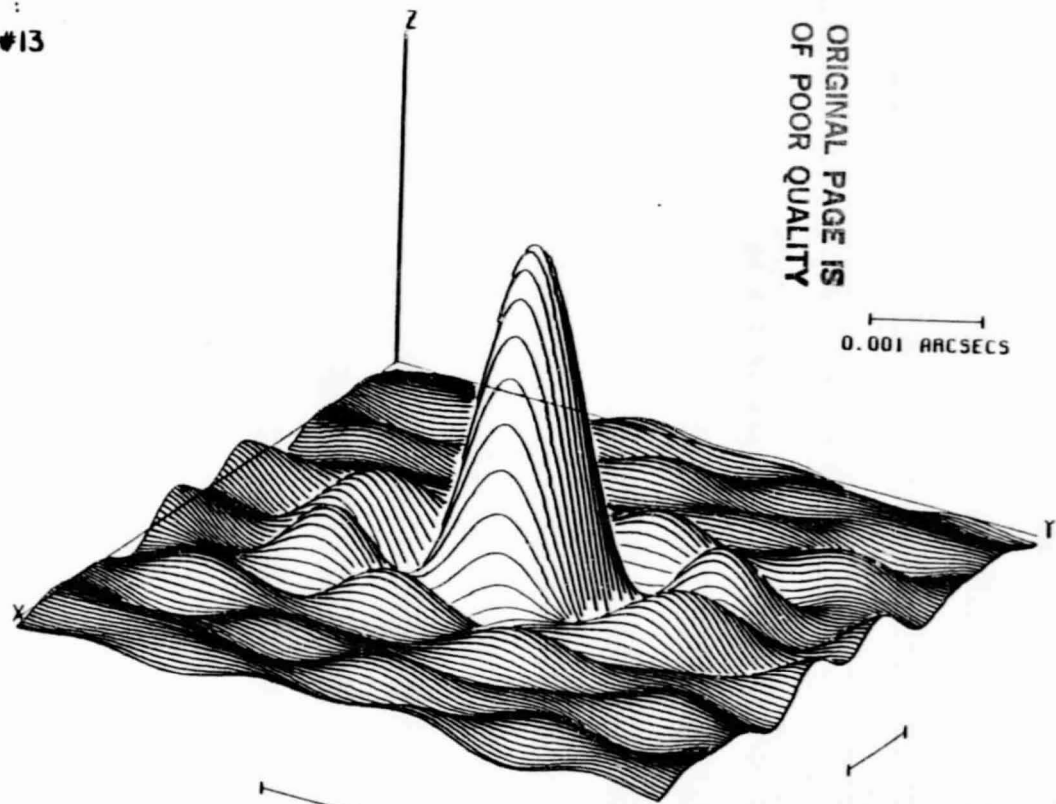
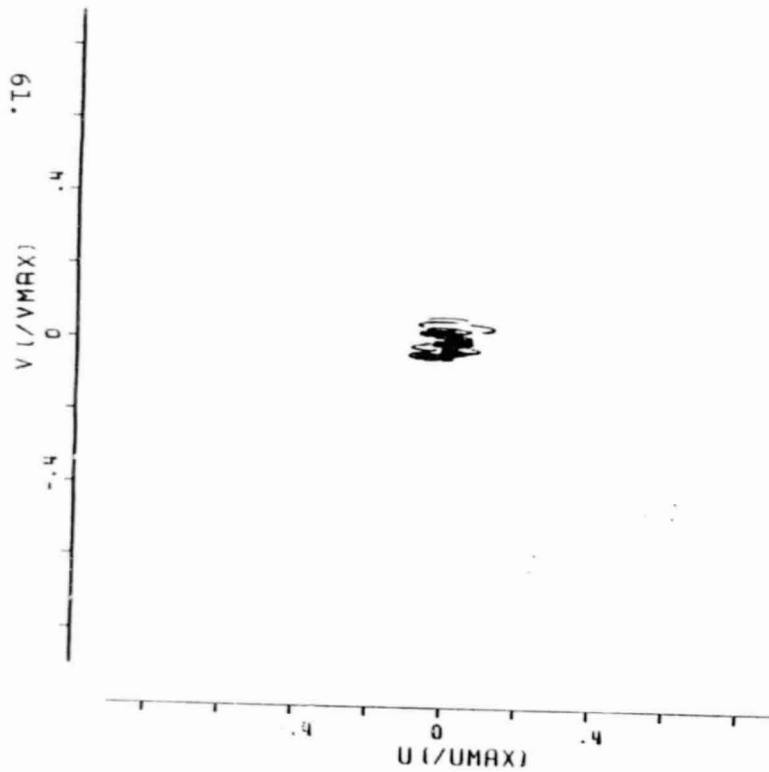
maximum baseline is considerably longer than for the dedicated array alone, and the u-v coverage is much denser than for a spacecraft plus a few existing ground stations. An observation made with u-v coverage like that in Figure IV-5f would be comparable in u-v density to that obtained with the VLA, but with the resolution appropriate to an Earth-sized antenna!

For a source at lower declination ( $\delta = 30^\circ$ ), the dedicated array does not function quite as well (Figure IV-6a). The North-South extent of the u-v tracks is lessened (by  $\sin \delta$ ) and the length of each u-v track is decreased (by the shortened mutual visibility time of a source of lower  $\delta$ ). By comparison, space-borne observations with "edge-on" and "face-on" orbits have considerably greater North-South u-v extent and longer tracks, as evidenced in Figures IV-6b and c. Once again, with only a few ground stations there are large "holes", and the beam patterns have larger sidelobe levels than one would desire. However, combination of the dedicated array and a space antenna yields excellent u-v coverage, for either an "edge-on" (Figure IV-6d) or "face-on" (Figure IV-6e) orbit. In fact, it works every bit as well at  $\delta = 30^\circ$  as it does at  $\delta = 64^\circ$ .

When the source is moved into the third section of the sky,  $\delta = 6^\circ$ , the problems with a purely ground-based become severe (Figure IV-7a). Although the antenna locations were chosen to yield significant North-South baselines, in particular by putting an antenna in Alaska, the v-extent of the coverage is quite limited. And at this  $\delta$  the lengths of the u-v tracks are highly restricted by the short mutual visibility times for two antennas with a large East-West separation. Comparison with Figures IV-5a and IV-6a shows that a significant degradation in both resolution and coverage completeness occurs when a VLBA is used at low declination. However, as illustrated in Figures IV-7b and IV-7c, the resolution obtained from space VLBI is not highly degraded

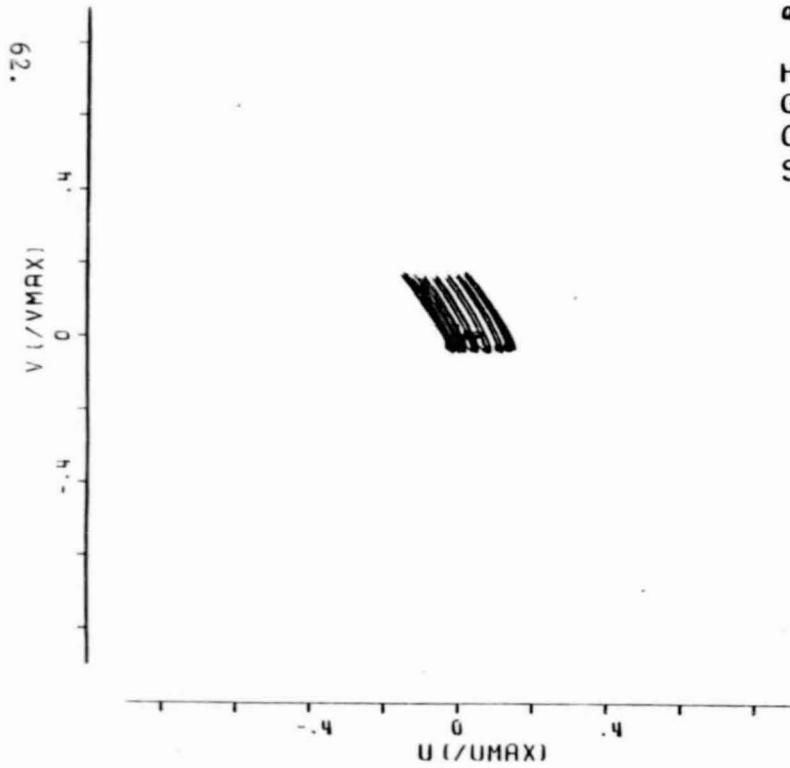
Figure IV-7. Fourier coverage and synthesized beam from simulated VLB observations of a source at  $\alpha = 12^{\text{h}}$ ,  $\delta = +6^{\circ}$ . The angular scale corresponds to an observing wavelength of 2.8 cm.

$\alpha = 12^h, \delta = +6^\circ$   
NTWK #13



ORIGINAL PAGE IS  
OF POOR QUALITY

Figure IV-7a



$$\alpha = 12^h, \delta = +6^\circ$$

HSTK  
 GB  
 OVRO  
 SHUTTLE ( $i = 57^\circ, \Omega = 0^\circ$ )

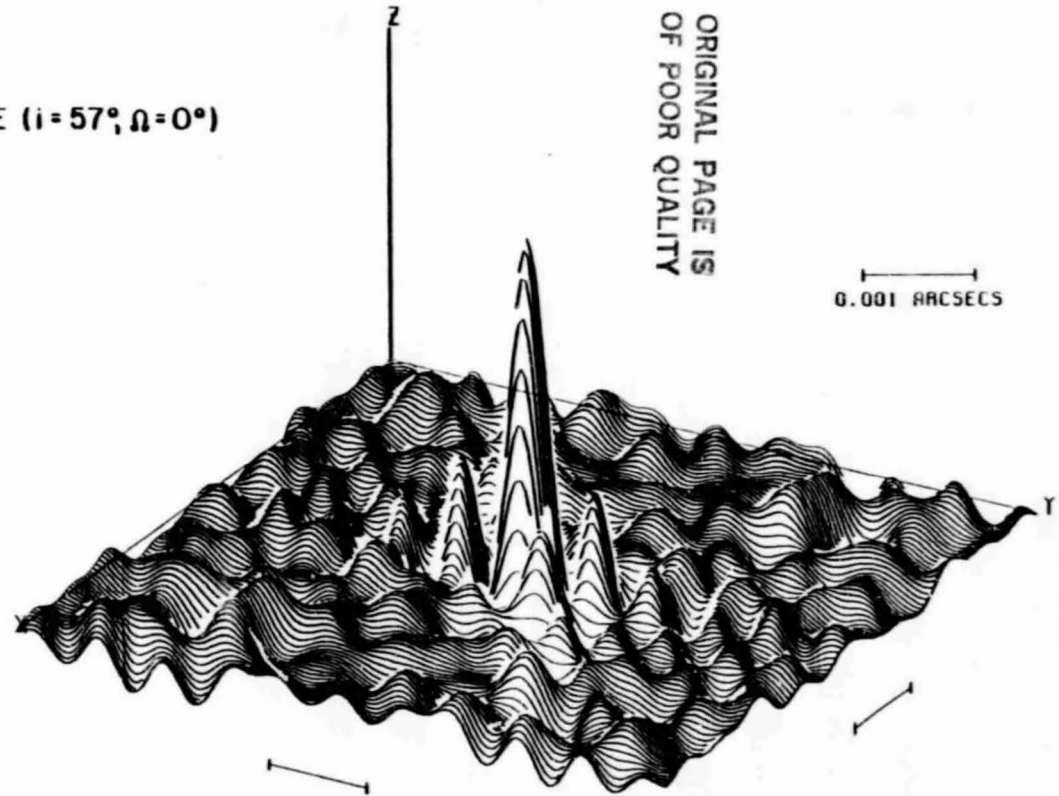
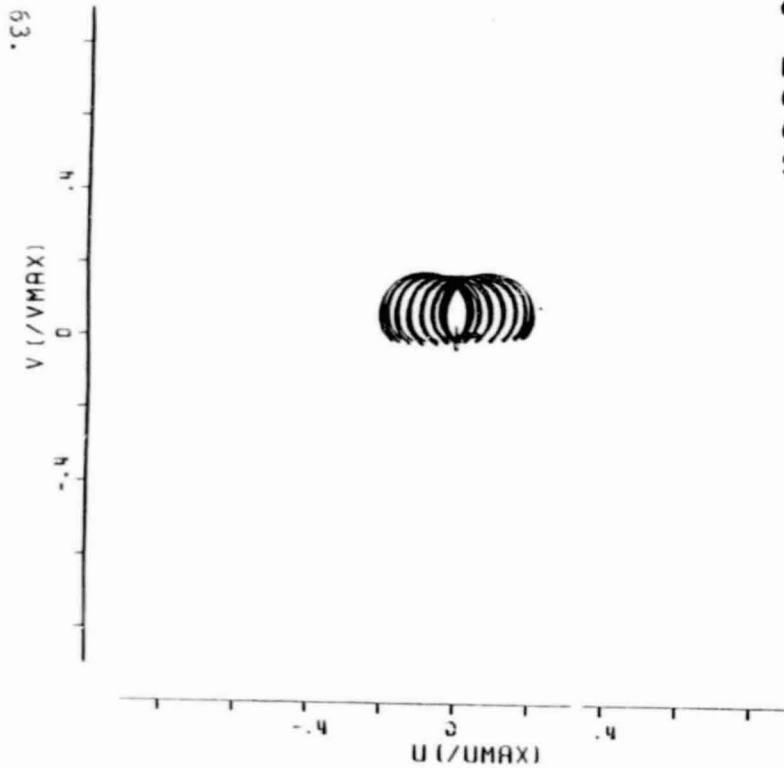
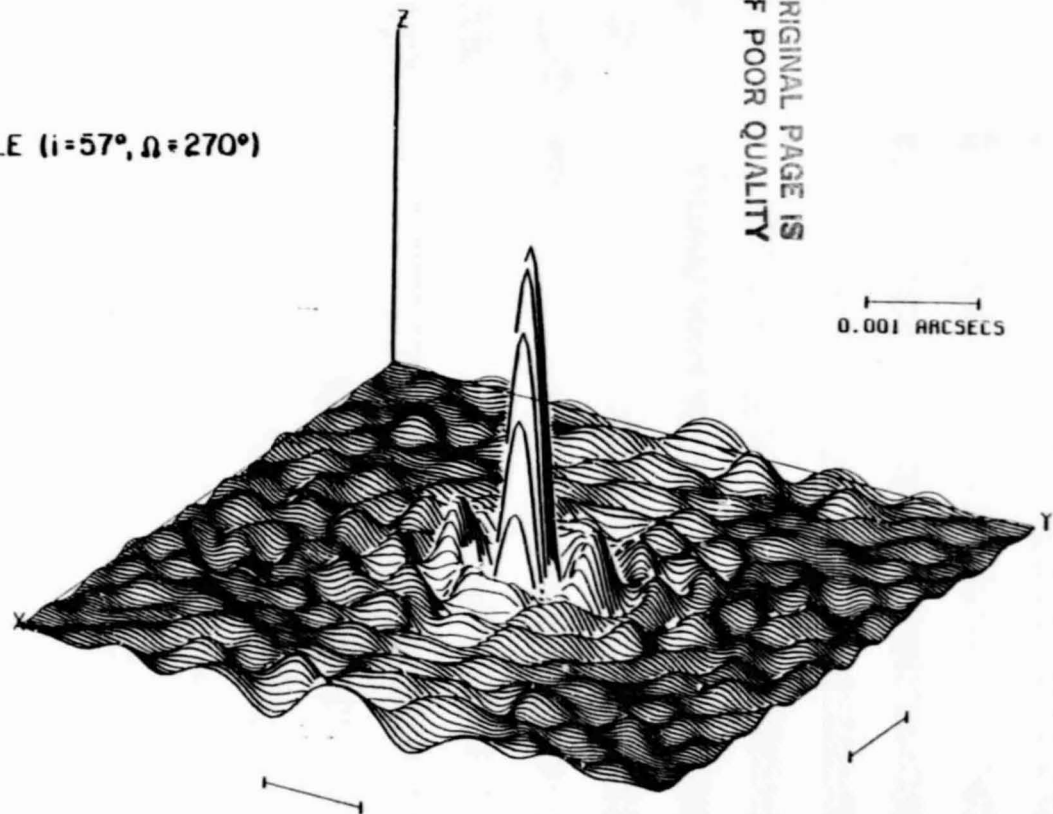


Figure IV-7b



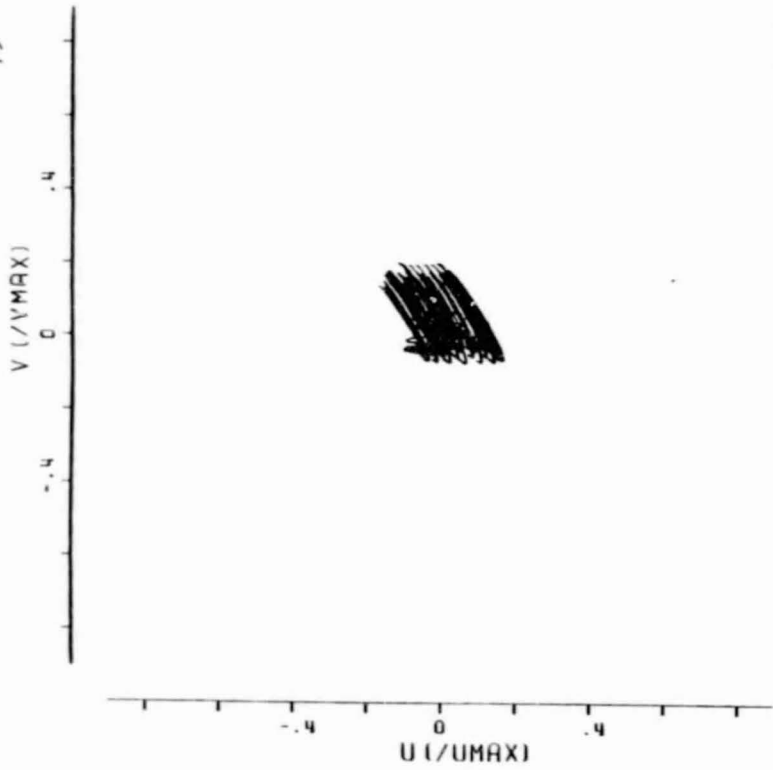
$$\alpha = 12^h, \delta = +6^\circ$$

HSTK  
 GB  
 OVRO  
 SHUTTLE ( $i = 57^\circ, \Omega = 270^\circ$ )

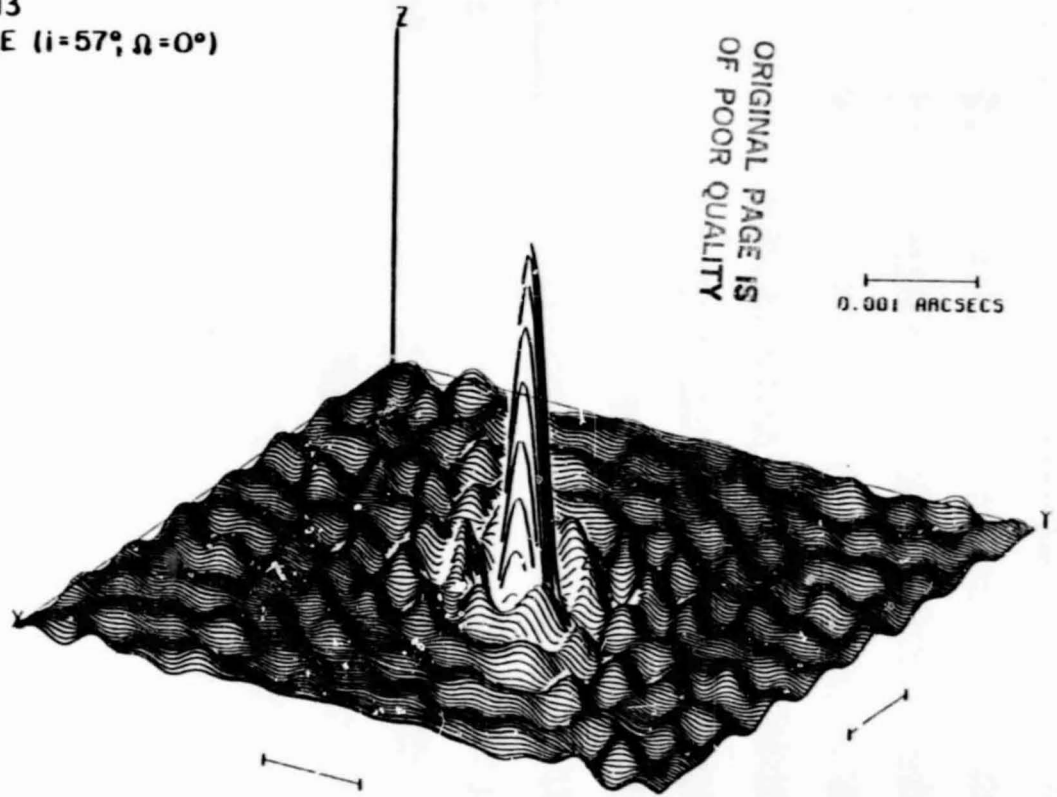


ORIGINAL PAGE IS  
 OF POOR QUALITY

Figure IV-7c

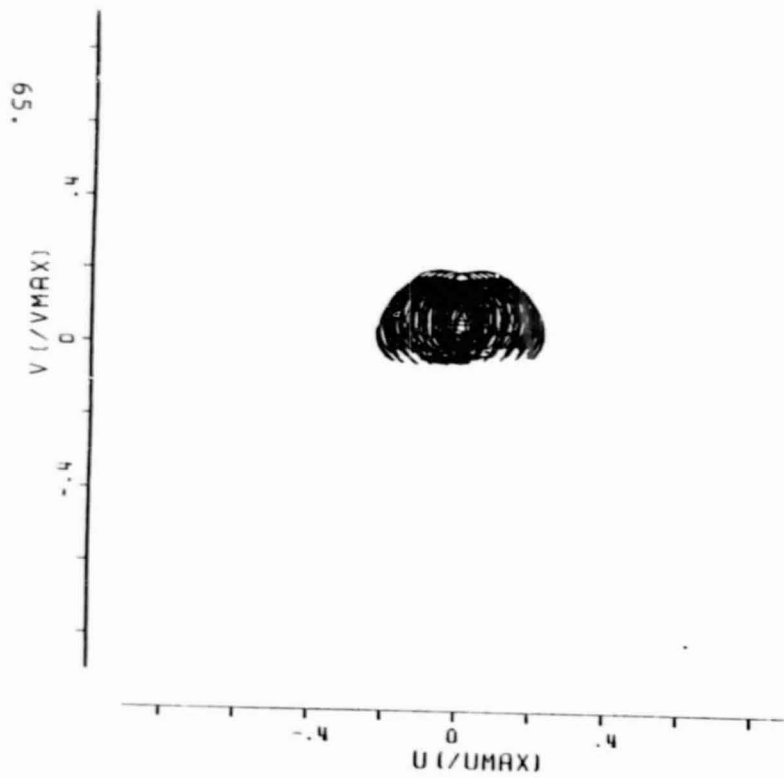


$\theta = 12^h \delta = +6^\circ$   
NTWK#13  
SHUTTLE ( $i = 57^\circ, \Omega = 0^\circ$ )



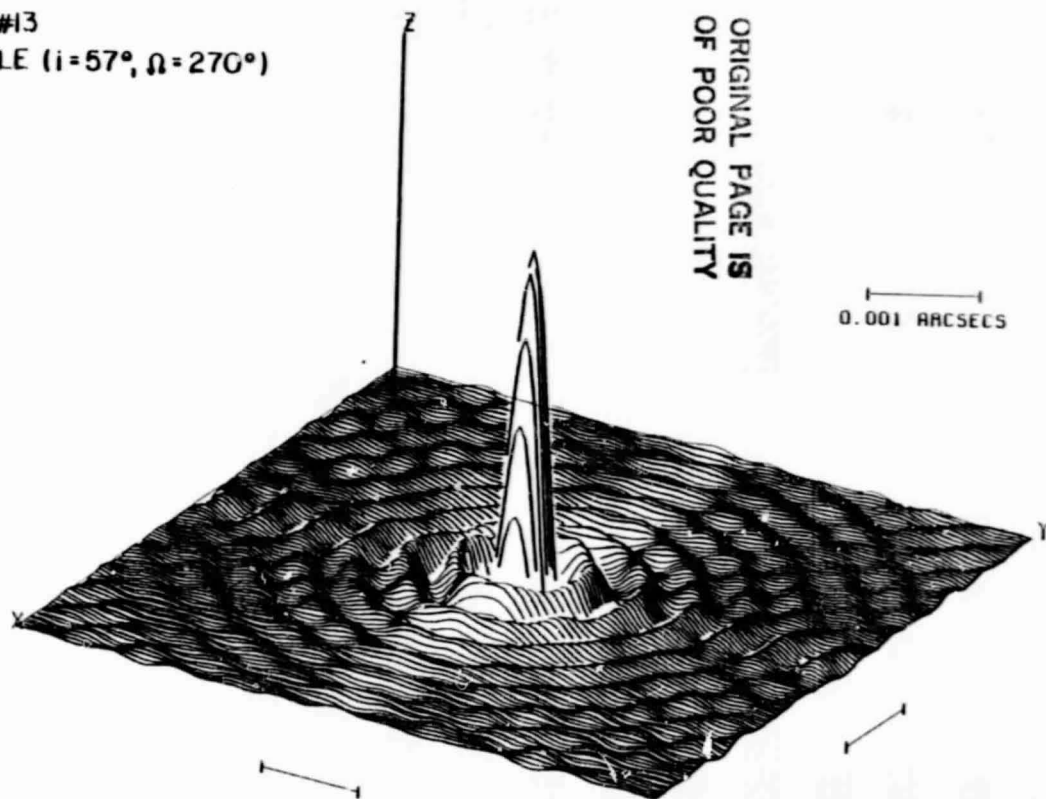
ORIGINAL PAGE IS  
OF POOR QUALITY

Figure IV-7d



$$\alpha = 12^h, \delta = +6^\circ$$

NTWK #13  
SHUTTLE ( $i = 57^\circ, \Omega = 270^\circ$ )



ORIGINAL PAGE IS  
OF POOR QUALITY

Figure IV-7e

for low  $\delta$ . This is because the spacecraft orbit is chosen to be highly inclined to the celestial equator, yielding a significant North-South space antenna--ground-antenna separations even for a source on the celestial equator. (In Section VIII below we discuss the choice of a single "best" orbit for space VLBI. A tentative answer,  $i \approx 57^\circ$ , is the basis for our choice of orbital inclination in this section, and is compatible with the orbits obtainable with the Shuttle.) Combinations of ground array and space antenna, for "edge-on" and "face-on" orbits, result in Figures IV-7d and 7e. Especially for the latter orbit, the results of such a combination are nearly as good as those for sources at high declinations.

A quantitative comparison of the beams generated by a VLBA alone, by one space antenna and three ground stations, and by the combination of a VLBA and a space antenna is made in Figures IV-8 through IV-13. The first three Figures, IV-8, IV-9, and IV-10 are effectively cross-sections of the beams. These are plots of the maximum absolute value of the beam, evaluated in ten annuli surrounding the central peak. This effectively displays the amplitude of the beam sidelobes as a function of angular distance from the center.

The root-mean-square (i.e., the fluctuation about zero) of the beam as a function of radius from the central peak is plotted in Figures IV-11 through IV-13. For the region outside the central peak we have used the same annuli as above to calculate the fluctuations in the beam for each of the simulations presented in this section. In addition, we have plotted the half-width at half-amplitude of each central peak; both major and minor axes are shown if they differ significantly.

Study of these figures confirms that the combination of a VLBA and a space antenna is superior in resolution and in sidelobe level to a VLBA alone,

while a space antenna and a few ground stations has superior resolution but poorer sidelobe level. The degradation of the performance of a VLBA at low source declination may also be seen by comparing the figures. Finally, they also demonstrate that an optimum VLBA-plus-space antenna combination does not suffer such a fall-off at low source declination.

Figure IV-8. Cross-section in annuli of the absolute maxima of the beams in Figures IV-5a ("Network#13"), IV-5c ("Shuttle + 3 stations"), and IV-5f ("Shuttle + Network #13").

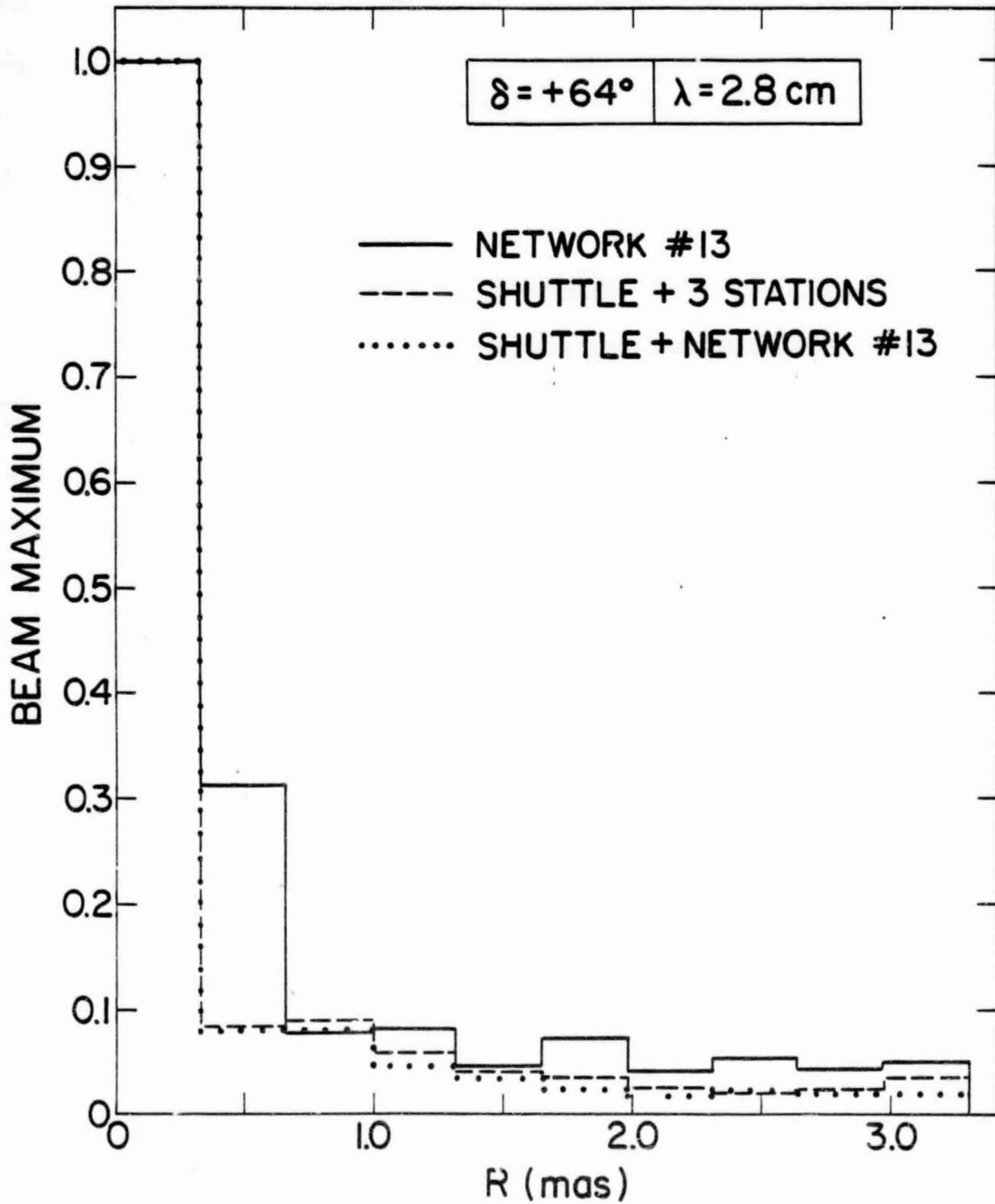


Figure IV-8

Figure IV-9. Cross-section in annuli of the absolute maxima of the beams in Figure IV-6a ("Network#13"), IV-6c ("Shuttle + 3 stations"), and IV-6e ("Shuttle + Network #13").

Figure IV-10. Cross-section in annuli of the absolute maxima of the beams in Figure IV-7a ("Network #13"), IV-7c ("Shuttle + 3 stations"), and IV-7e ("Shuttle + Network #13").

ORIGINAL PAGE IS  
OF POOR QUALITY

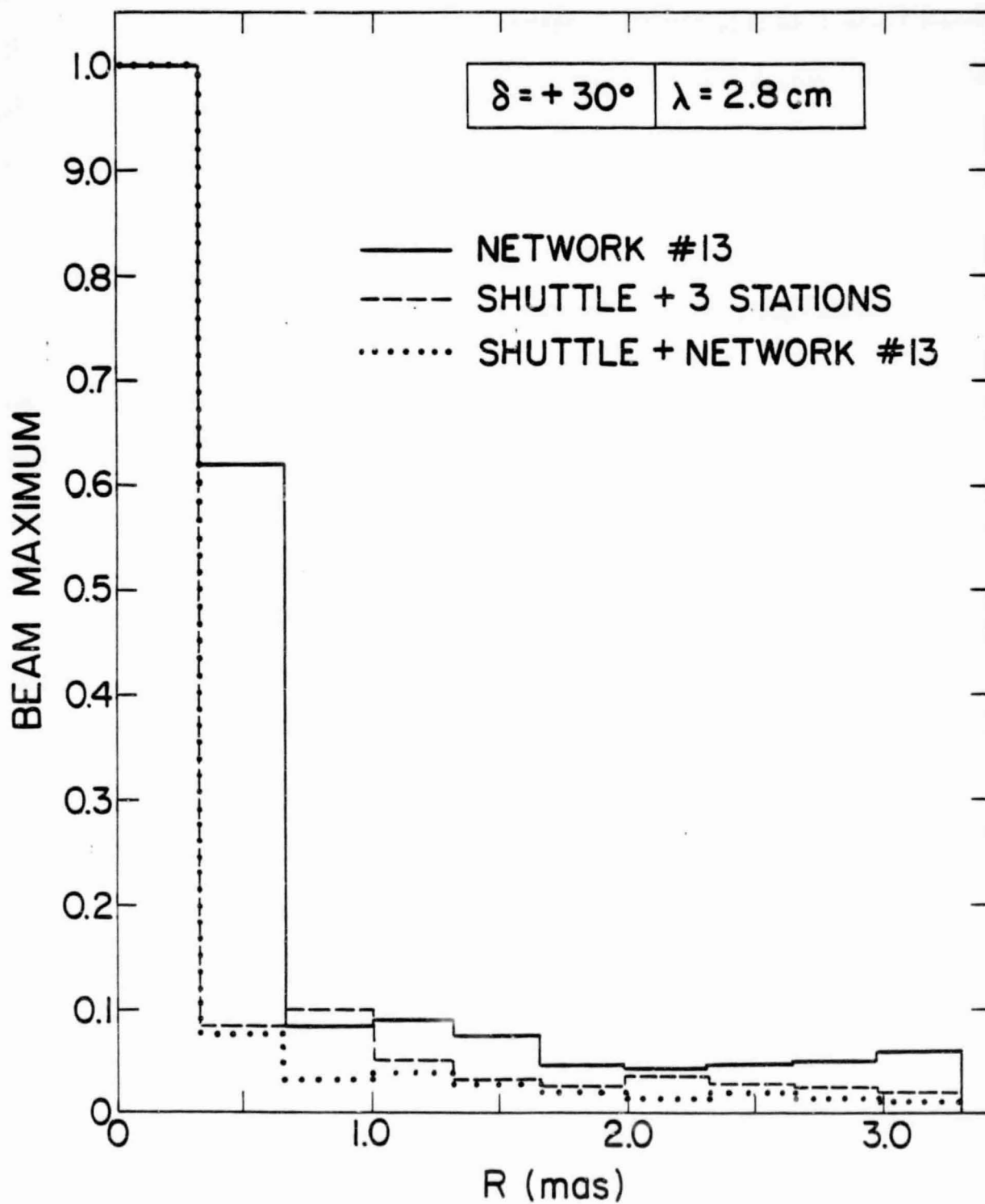


Figure IV-9

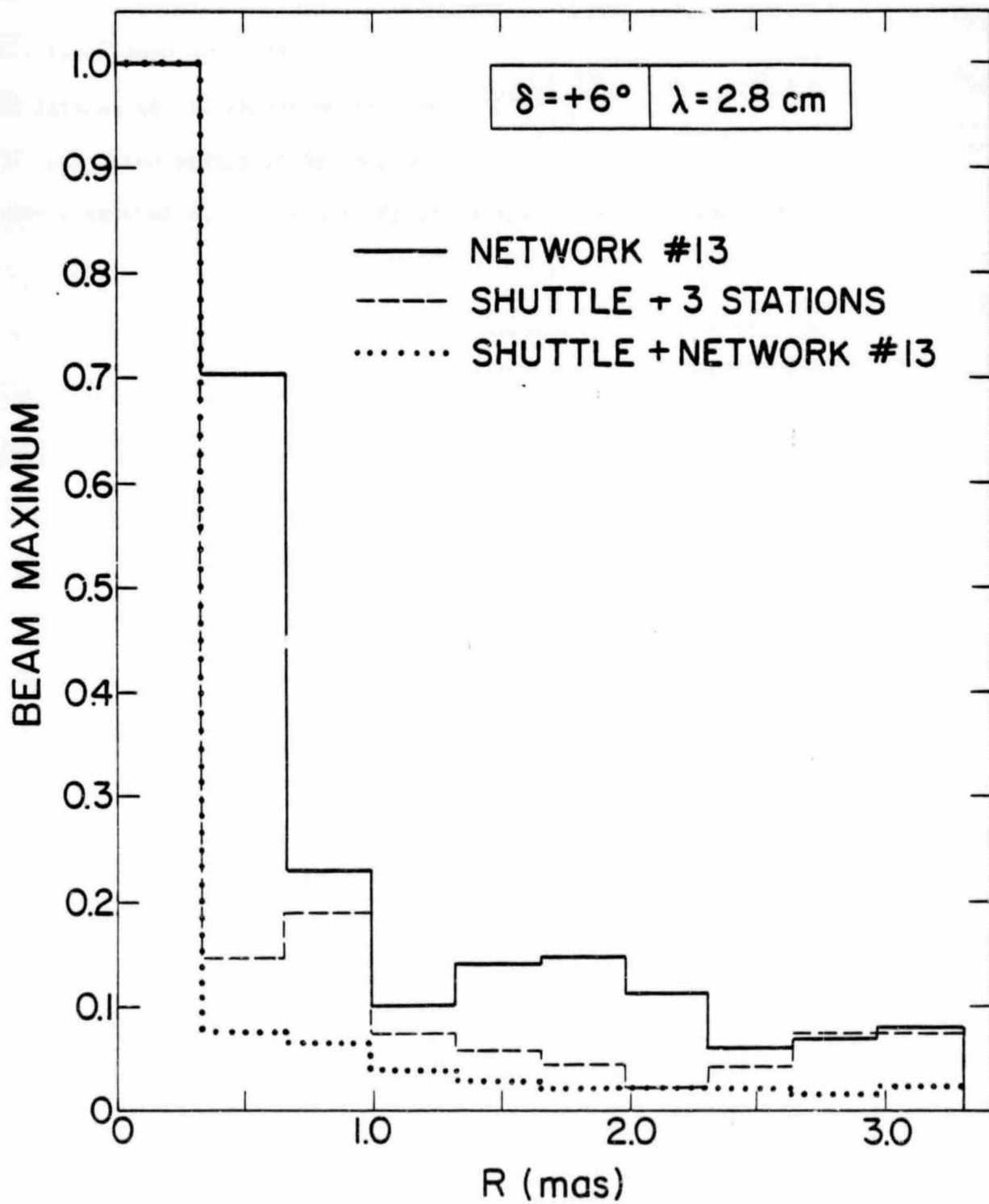


Figure IV-10

Figure IV-11. Root-mean-square beam as a function of the angular distance from the central peak, for the parts of the beam outside the peak for the cases presented in Figures IV-5 ( $\delta = 64^\circ$ ). The horizontal bars with tick marks show the half-width at half-amplitude of the central peaks; where there are two ticks, they correspond to differing major and minor axes. The labels A - F correspond to the Figures IV-5a through IV-5f.

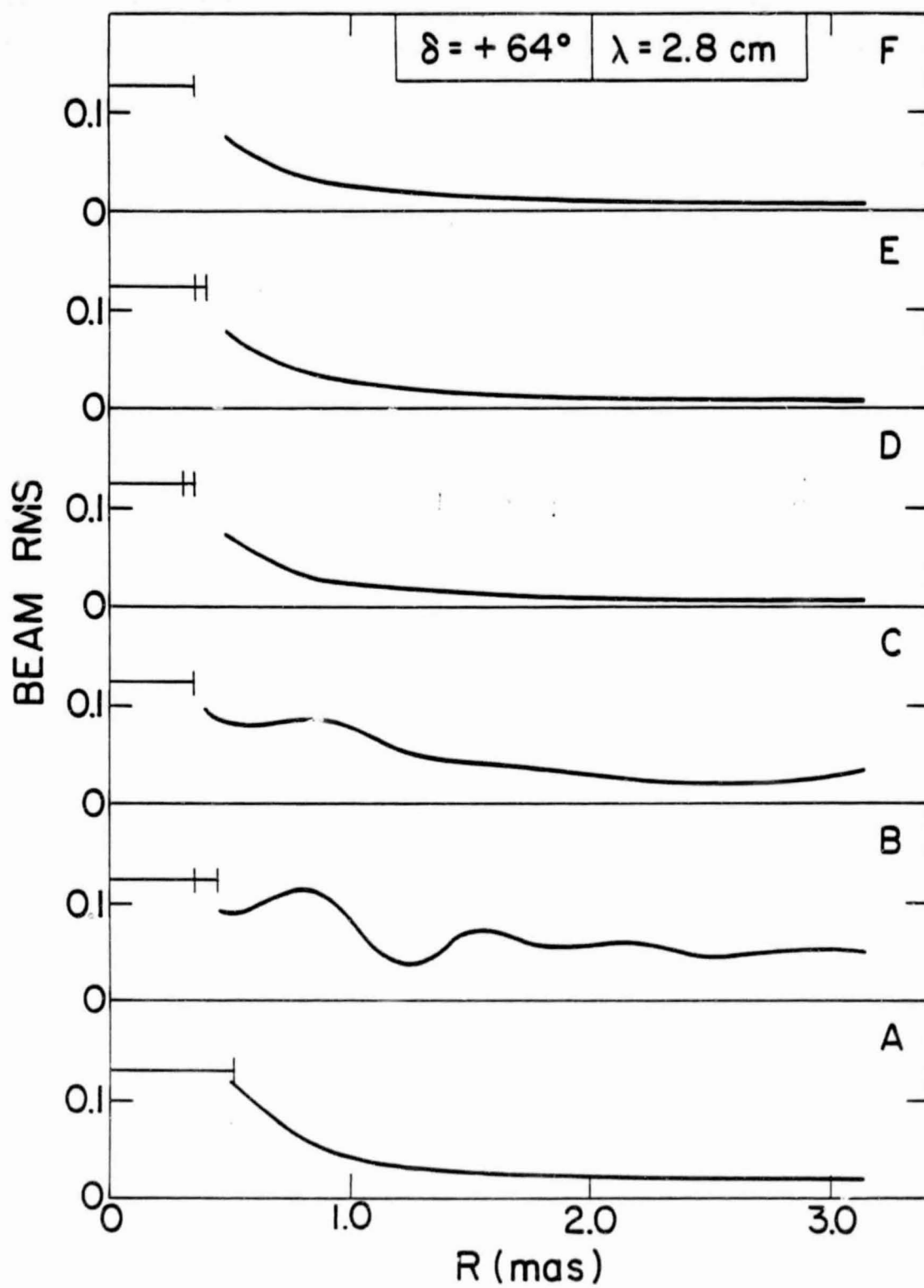


Figure IV-11

Figure IV-12. Root-mean-square beam as a function of the angular distance from the central peak, for the parts of the beam outside the peak in the cases presented in Figures IV-6 ( $\delta = 30^\circ$ ). The horizontal bars with tick marks show the half-width at half-amplitude of the central cores; where there are two ticks, they correspond to differing major and minor axes. The labels A - E correspond to the Figures IV-6a through IV-6e.

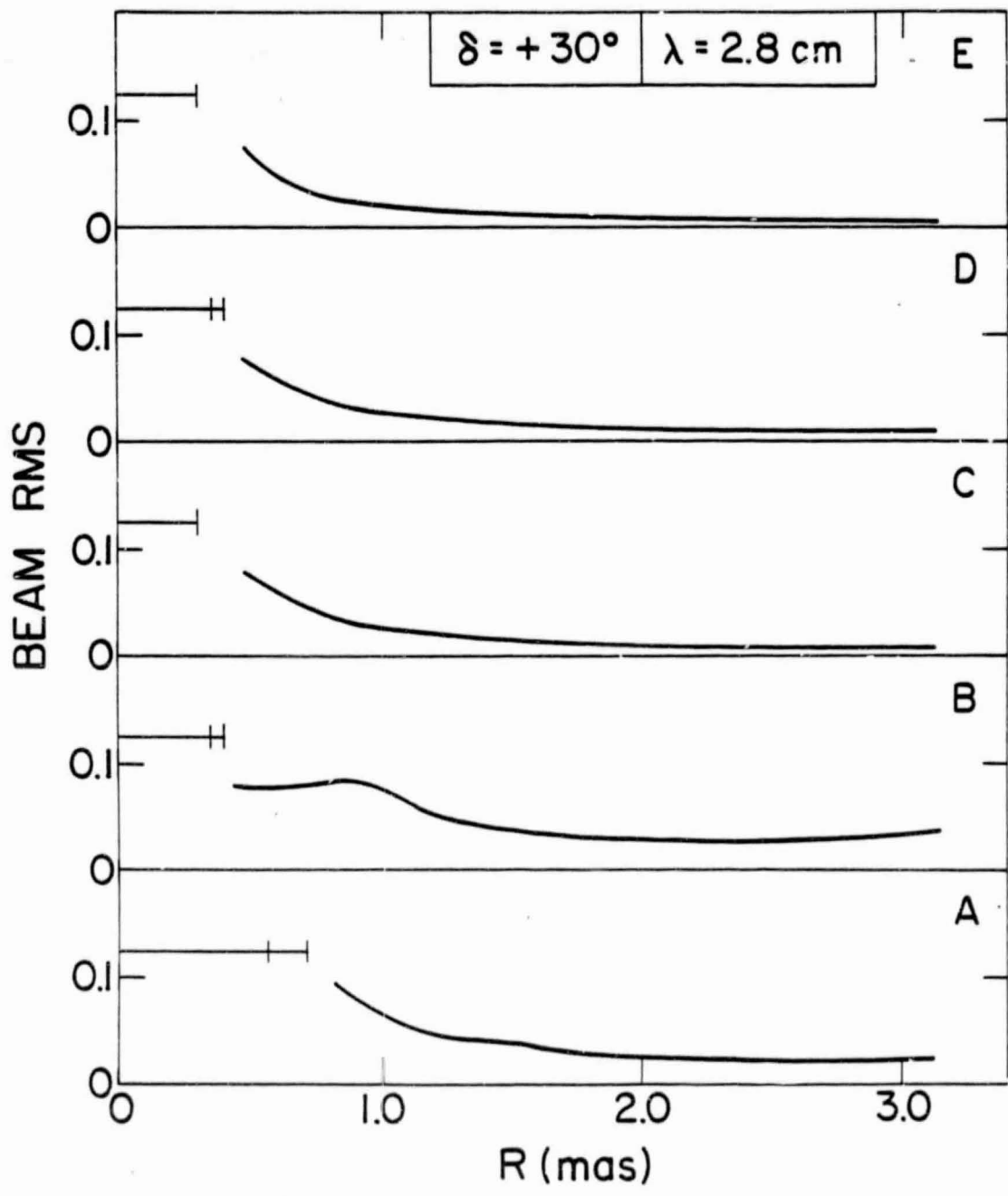


Figure IV-12

Figure IV-13. Root-mean-square beam as a function of the angular distance from the central peak, for the parts of the beam outside the peak in the cases presented in Figures IV-7 ( $\delta = 6^\circ$ ). The horizontal bars with tick marks show the half-width at half-amplitude of the central cores; where there are two ticks, they correspond to differing major and minor axes. The labels A - E correspond to the Figure IV-7a through IV-7e.

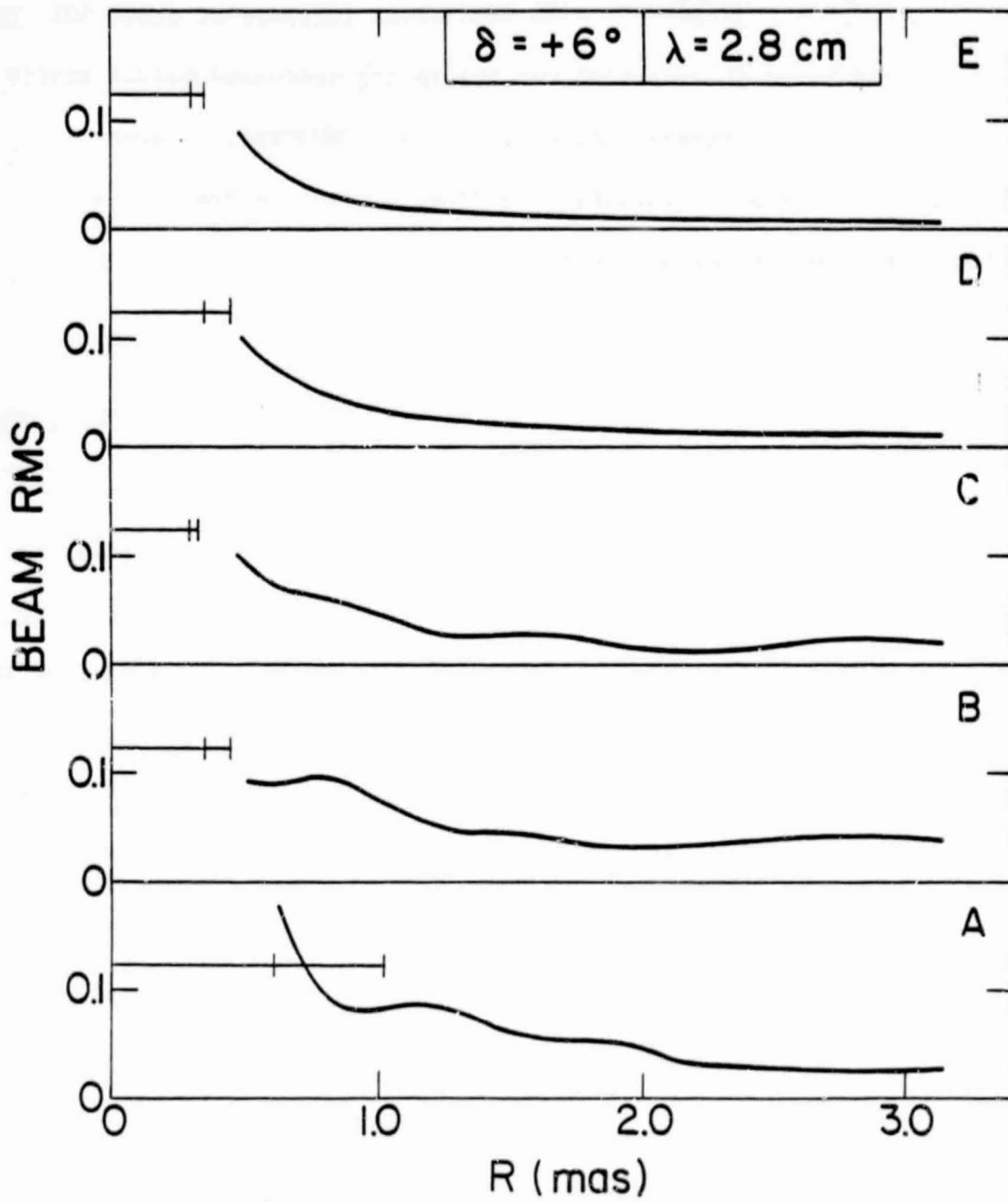


Figure IV-13

## V. SIMULATIONS FOR LARGE ORBITS

In the previous section we demonstrated the ability of a single space antenna in a near-earth orbit to increase the density and extent of the u-v coverage of a VLBI observation. The resolution increase of about 50% over purely ground-based observations was due to the increased mutual source visibility achieved by a space-ground antenna pair. However, in order to produce dramatic increases in resolution we need to consider spacecraft orbits which extend far from the Earth. We saw in §III that interstellar scattering will limit the longest useful baseline, but that even a pessimistic estimate suggests that baselines of several hundred Earth radii will be useful. In this section we examine briefly the properties of a deep-space VLB system involving two or three satellites in highly-elliptical orbits. More than one satellite is necessary because when the orbit size is much greater than an Earth diameter, all Earth-spacecraft baselines are approximately the same, roughly the shape of the orbit itself. Thus filling the u-v plane depends on spacecraft-spacecraft baselines. In order to be able to do so for sources in any direction, the orbits need to be properly oriented. In what follows we study the use of two or three orbits of semi-major axes  $a \approx 100,000$  km [so the longest Earth-spacecraft baseline is  $B_{\max} \approx 2a \approx 30 R_E$ ], oriented so that the spacecraft-spacecraft baselines have reasonable projections perpendicular to any source direction. In all cases the angular scale is appropriate to a wavelength of  $\lambda = 18$  cm.

### A. Two Large Elliptical Orbits

Two spacecraft oriented so that their major axes are both in the celestial equator and are mutually perpendicular are used in the first simulations. One has its minor axis in the plane of the celestial equator, the other has its minor axis perpendicular to this plane. The two semi-major axes are

chosen so that the time  $\Delta T$  required for 10 orbits of the satellite in the smaller orbit corresponds to that for 9 orbits of the other one. Three ground stations spaced roughly around the Earth were used, so that there were almost always two spacecraft-ground baselines. Sources at seven locations around the celestial sphere were "observed" for this time  $\Delta T$ . These simulations are summarized in Table V-1, and the results presented in Figures V-1a through V-1g.

With only two spacecraft, it is not possible to produce good (u-v) coverage for sources at all  $(\alpha, \delta)$ . This is because orbits of high eccentricity, required for practical launches from the near-Earth environment, are "long" in only one direction. Thus two orbits can span a given plane, but sources in that plane will have u or v limited to the minor axis of one of the orbits. This is amply illustrated in Figures V-1a, 1d, and 1f, where sources in the celestial equator are "observed" with two orbits whose major axes lie in that plane. At higher declinations, however, the results are much better, and since such orbits are the energetically least expensive, a high-resolution VLB based on this kind of orbit might well be a good first step away from the Earth.

#### B. Simulations with Three Spacecraft

With the use of three spacecraft, including one whose major axis is highly inclined to the celestial equator, it is possible to get extensive (u-v) coverage for all source directions  $(\alpha, \delta)$ . Simulations based on the three orbits summarized in Table V-1 are presented in Figures V-2a through 2g. The source positions are the same as those used in the two-spacecraft examples. Comparison of the several examples shows that a "major-axis projection" is available in both u and v for all source positions, as expected. Here we have  $\Delta T = 8$  largest-orbit periods  $\approx 9$  middle-orbit periods  $\approx 10$  smallest-orbit periods, so the (u-v) tracks from spacecraft to spacecraft are "closed" and thus repeat

after  $\Delta T$ . However, in a real situation, the orbital periods would be incommensurate, and observation for extended periods would be able to "fill" the (u-v) plane. It should be noted, however, that the time scale is set by  $\Delta T \approx 10(3.3^d) = 33$  days, so such a (u-v) plane filling observations would take several months for orbits with  $a \approx 100,000$  km.

TABLE V-1

Simulations with Two or Three Elliptical Orbits

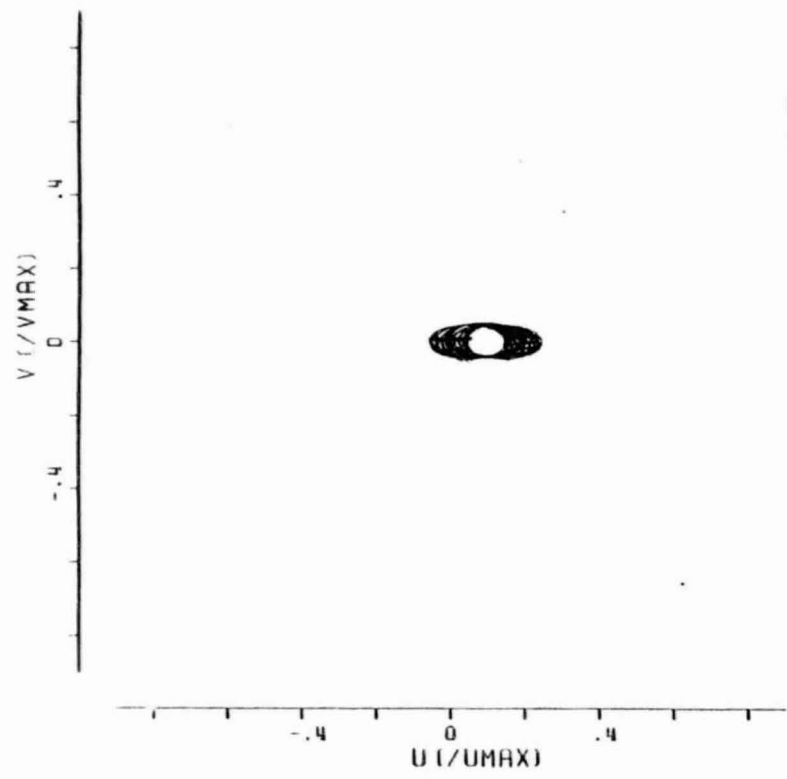
<u>Orbit</u>	<u>a(km)</u>	<u>e</u>	<u>i</u>	<u><math>\omega</math></u>	<u><math>\Omega</math></u>	<u>T(days)</u>
#1	100,000	0.9	0°	0°	0°	3.64
#2	92,000	0.9	90°	0°	90°	3.28

<u>Figure</u> =	<u>V-1a</u>	<u>1b</u>	<u>1c</u>	<u>1d</u>	<u>1e</u>	<u>1f</u>	<u>1g</u>
$\alpha$ (hours)	0	0	0	3	3	6	6
$\delta$ (degrees)	0	45	90	0	45	0	45

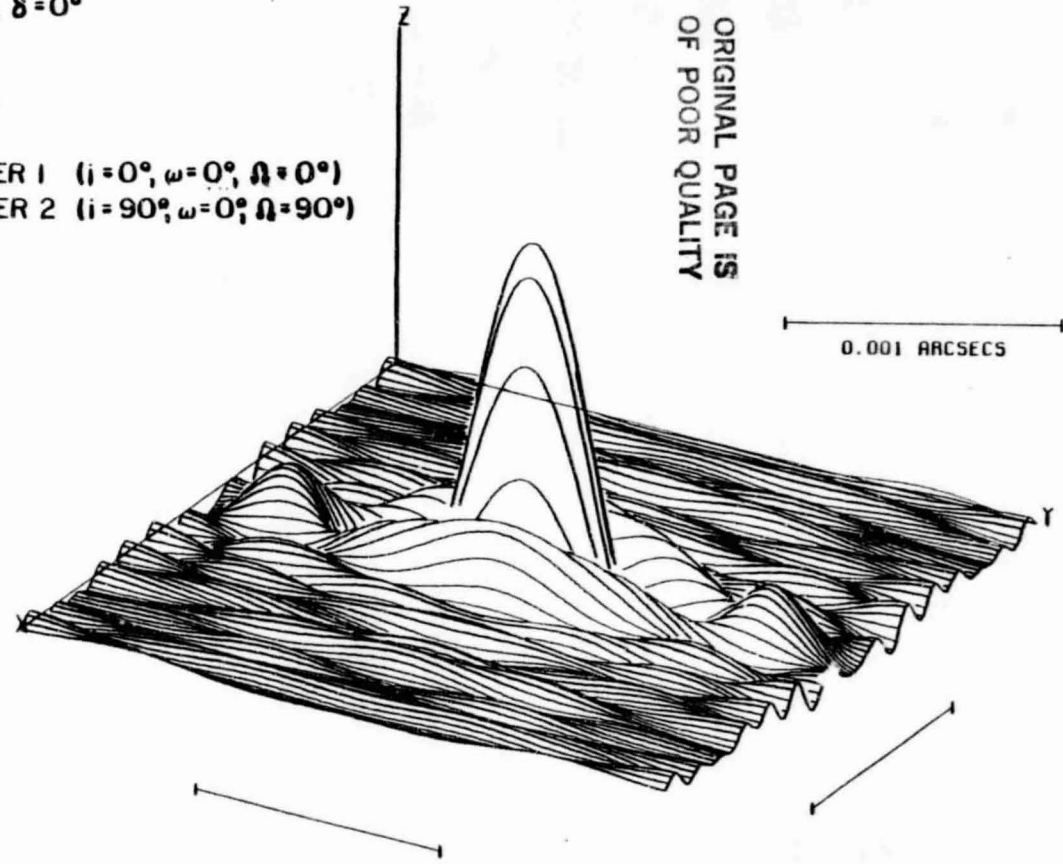
<u>Orbit</u>	<u>a(km)</u>	<u>e</u>	<u>i</u>	<u><math>\omega</math></u>	<u><math>\Omega</math></u>	<u>T(days)</u>
#1	100,000	0.9	0°	0°	0°	3.64
#2	93,200	0.9	0°	0°	90°	3.28
#3	86,200	0.9	90°	270°	0°	2.92

<u>Figure</u> =	<u>V-2a</u>	<u>2b</u>	<u>2c</u>	<u>2d</u>	<u>2e</u>	<u>2f</u>	<u>2g</u>
$\alpha$ (hours)	0	0	0	3	3	6	6
$\delta$ (degrees)	0	45	90	0	45	0	45

Figures V-1. Simulations of VLB observations with two highly-elliptical spacecraft orbits. In all cases the orbits are those described in Table V-1, and the seven source directions are spaced around the celestial equator and into the Northern celestial hemisphere in such a way as to get a good sample of the (u-v) coverage which is generated. The angular scale assumes an observing wavelength of 18 cm ( $\nu = 1.665$  GHz).



$\alpha = 0^h, \delta = 0^\circ$   
 GB  
 GDSTN  
 BONN  
 ORBITER 1 ( $i = 0^\circ, \omega = 0^\circ, \Omega = 0^\circ$ )  
 ORBITER 2 ( $i = 90^\circ, \omega = 0^\circ, \Omega = 90^\circ$ )



ORIGINAL PAGE IS  
 OF POOR QUALITY

Figure V-1a

ORIGINAL PAGE IS  
OF POOR QUALITY

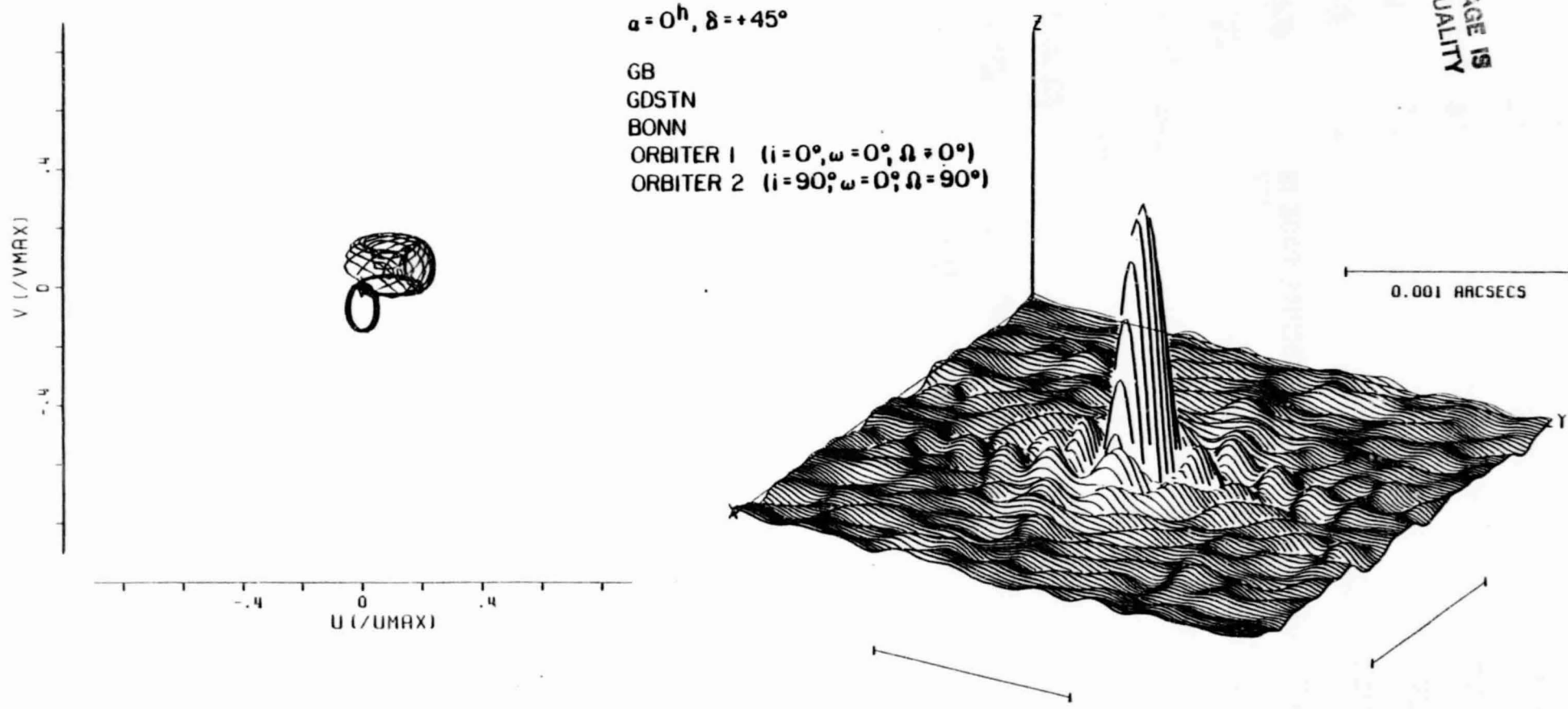
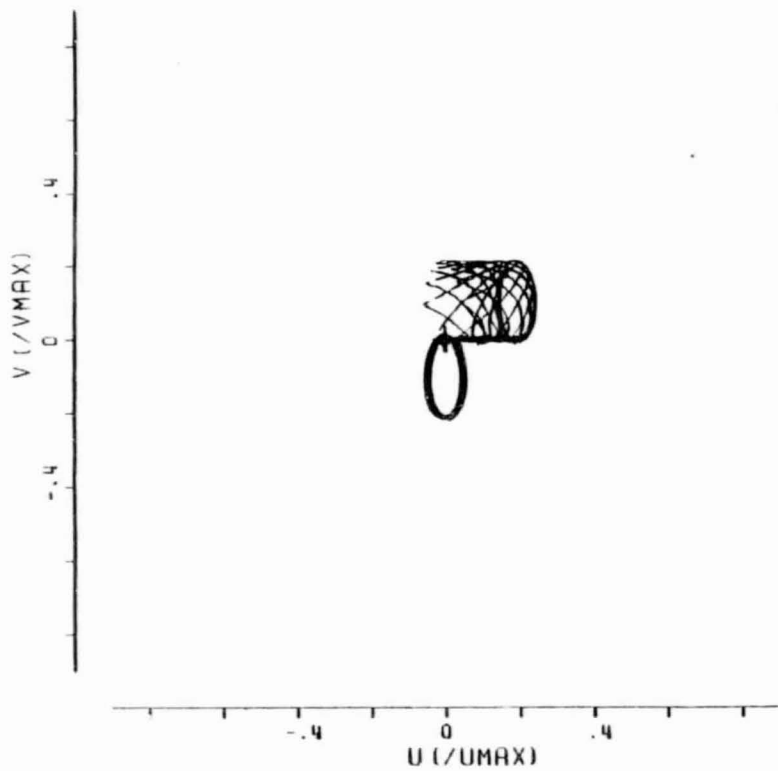


Figure V-1b



$$\alpha = 0^h, \delta = +90^\circ$$

GB

GDSTN

BONN

ORBITER 1 ( $i = 0^\circ, \omega = 0^\circ, \Omega = 0^\circ$ )

ORBITER 2 ( $i = 90^\circ, \omega = 0^\circ, \Omega = 90^\circ$ )

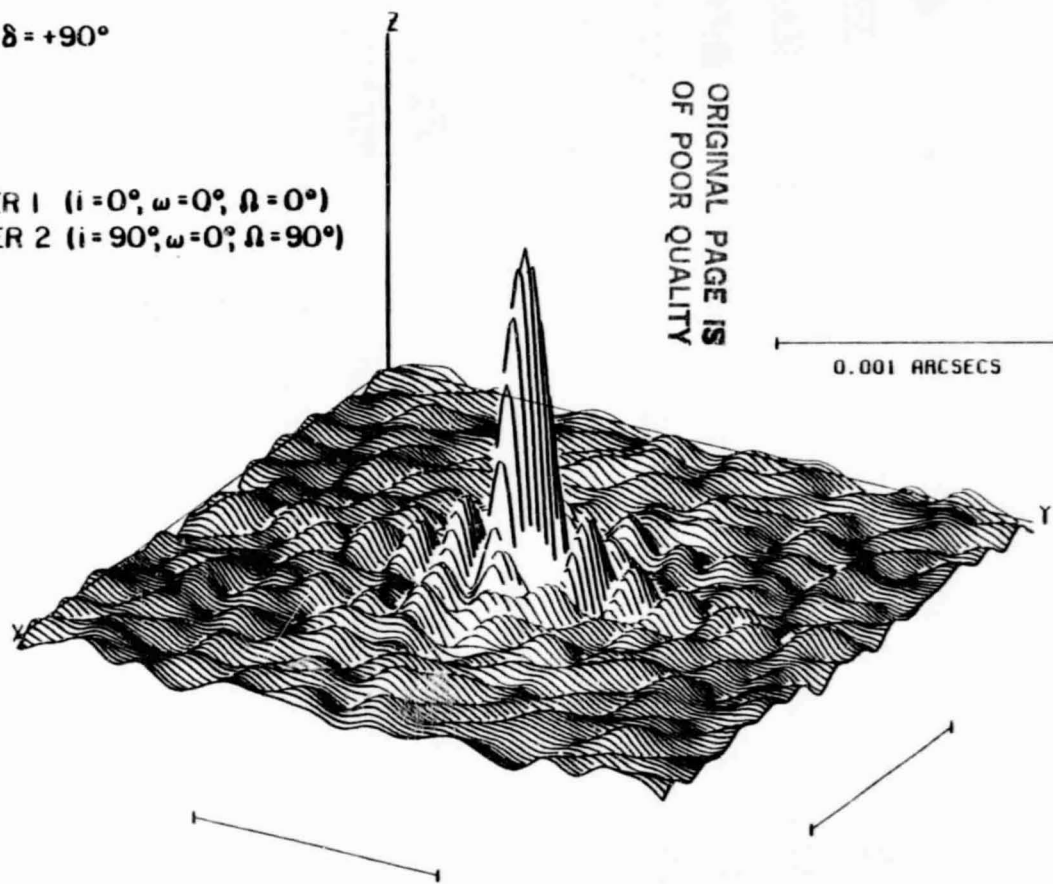
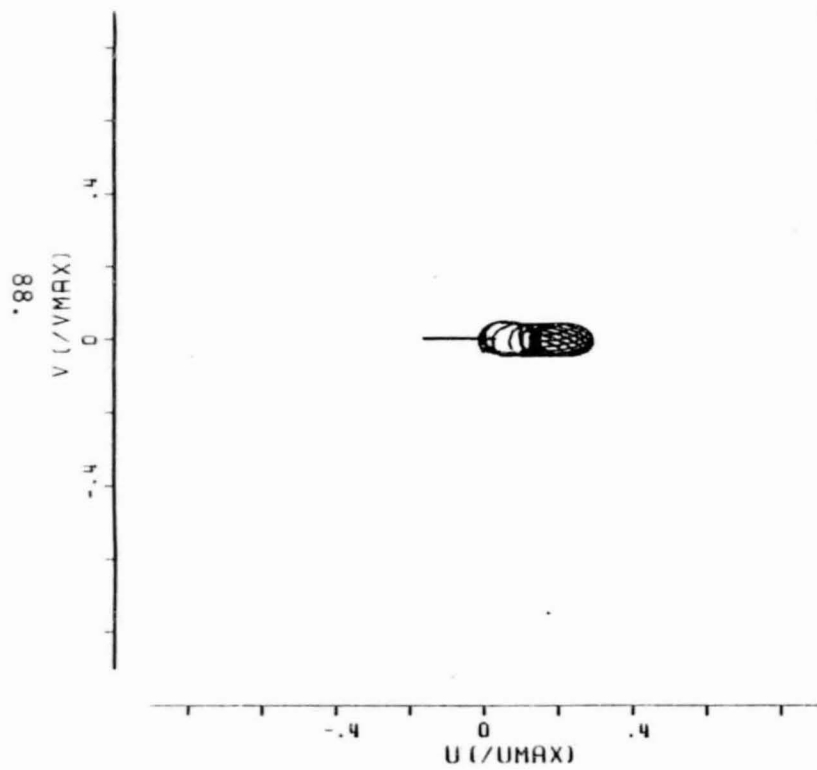


Figure V-1c

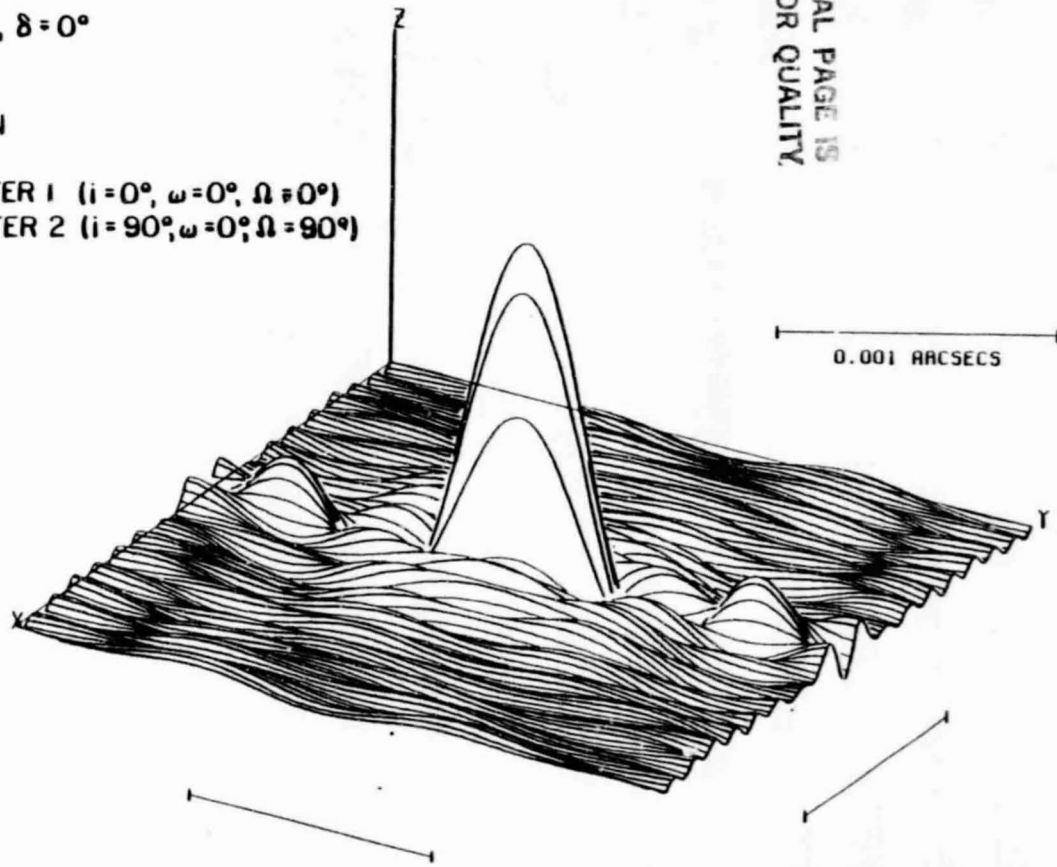


$$\alpha = 3^h, \delta = 0^\circ$$

GB  
GDSTN  
BONN

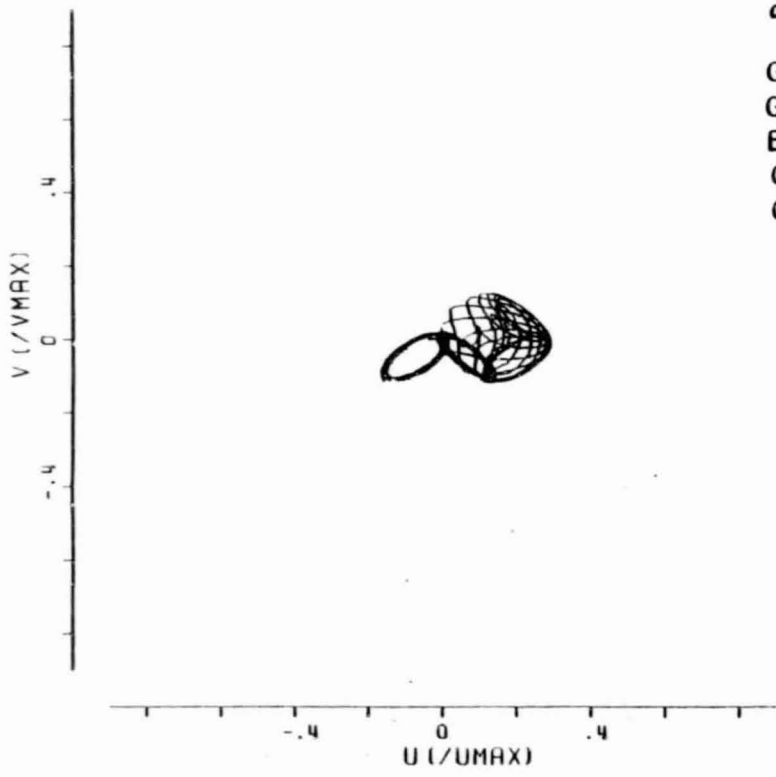
ORBITER 1 ( $i = 0^\circ, \omega = 0^\circ, \Omega = 0^\circ$ )

ORBITER 2 ( $i = 90^\circ, \omega = 0^\circ, \Omega = 90^\circ$ )

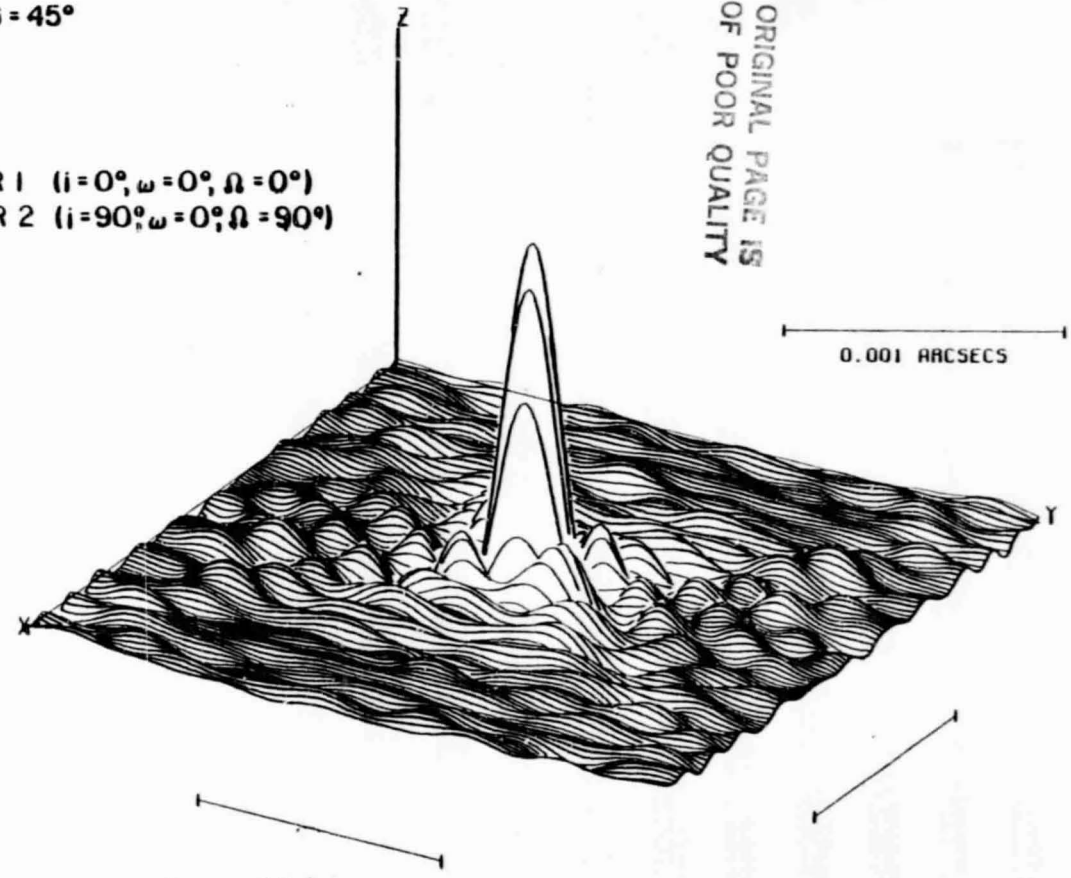


ORIGINAL PAGE IS  
OF POOR QUALITY.

Figure V-1d

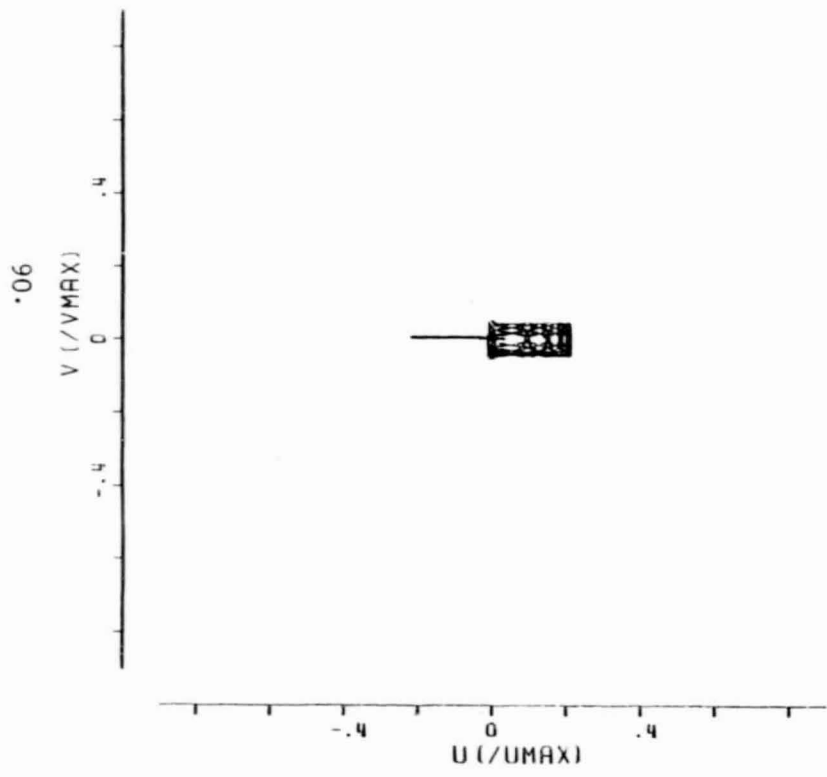


$\alpha = 3^h, \delta = 45^\circ$   
 GB  
 GDSTN  
 BONN  
 ORBITER 1 ( $i = 0^\circ, \omega = 0^\circ, \Omega = 0^\circ$ )  
 ORBITER 2 ( $i = 90^\circ, \omega = 0^\circ, \Omega = 90^\circ$ )

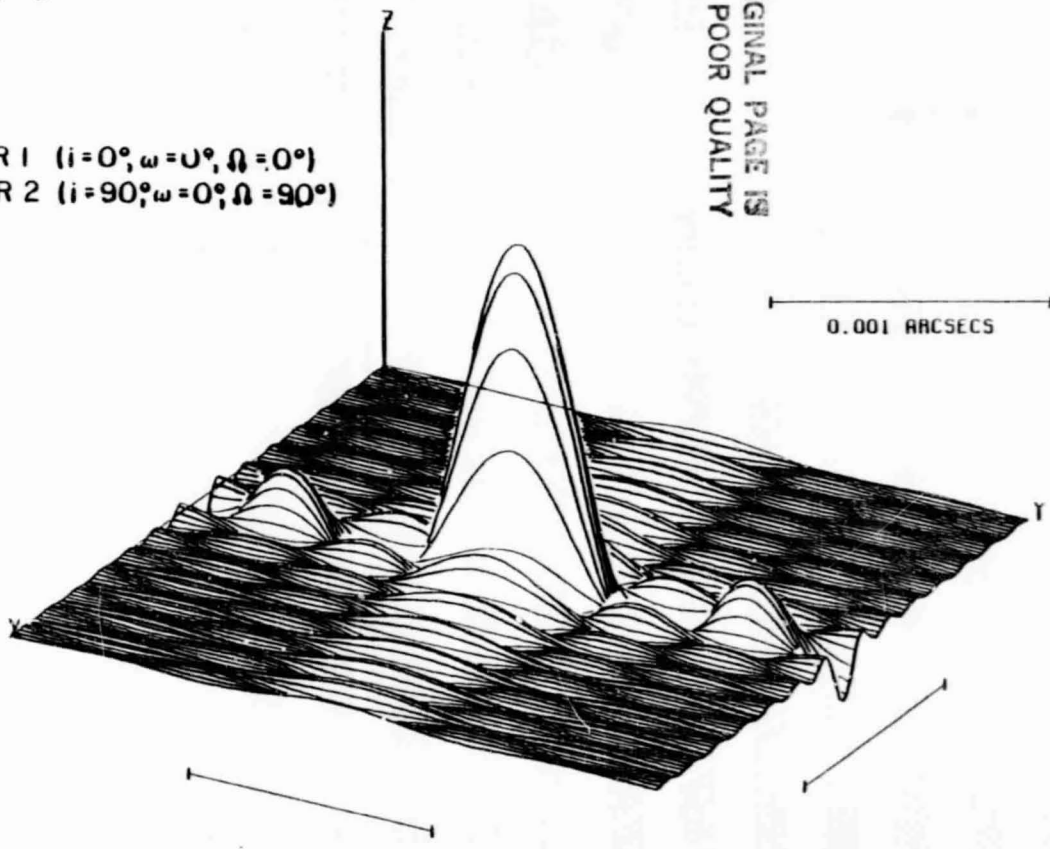


ORIGINAL PAGE IS  
 OF POOR QUALITY

Figure V-1e

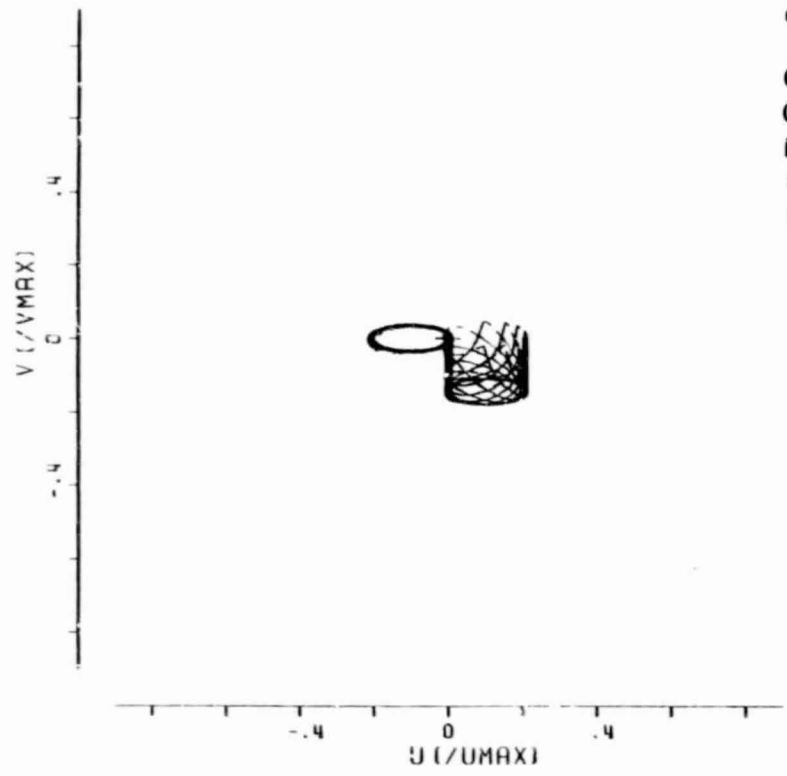


$a = 6h, \delta = 0^\circ$   
 GB  
 GDSTN  
 BONN  
 ORBITER 1 ( $i = 0^\circ, \omega = 0^\circ, \Omega = 0^\circ$ )  
 ORBITER 2 ( $i = 90^\circ, \omega = 0^\circ, \Omega = 90^\circ$ )

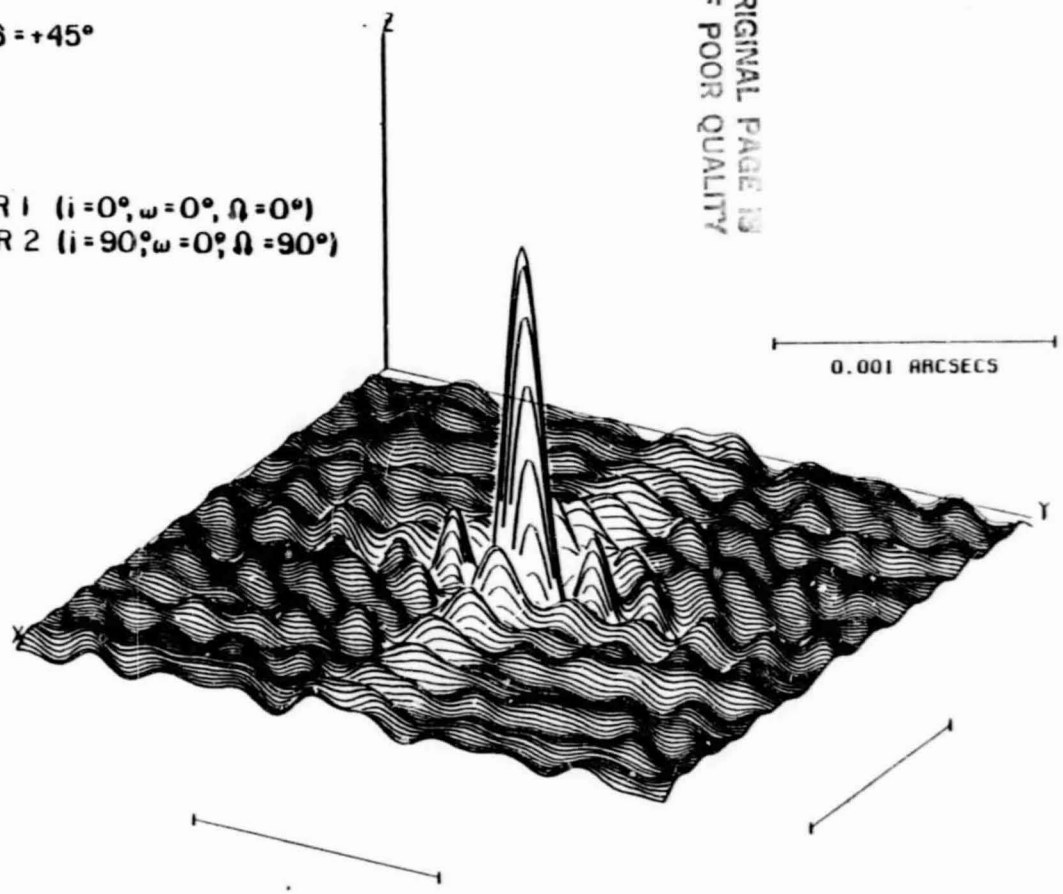


ORIGINAL PAGE IS  
OF POOR QUALITY

Figure V-1f



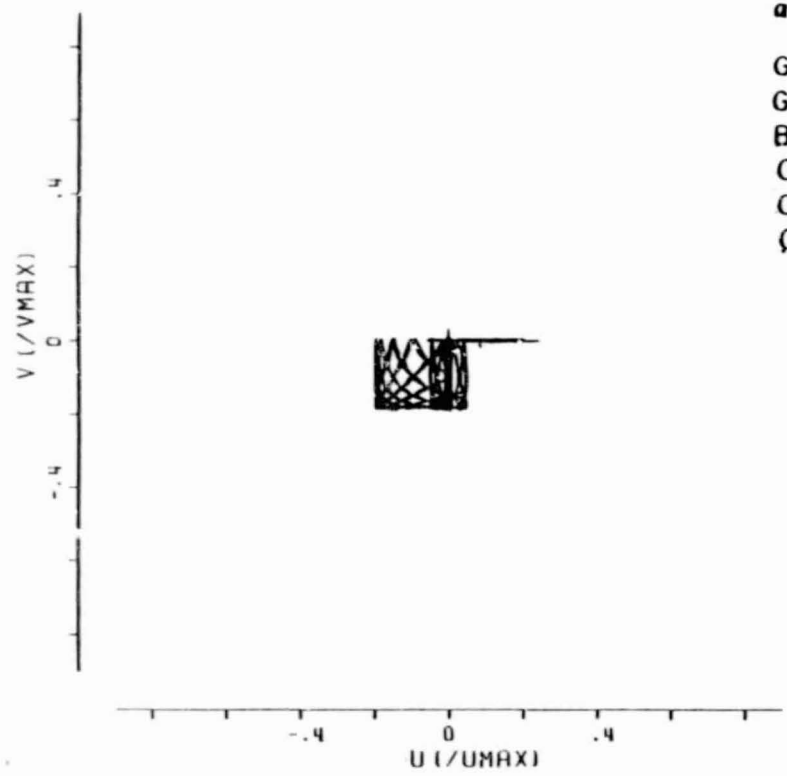
$\alpha = 6^h, \delta = +45^\circ$   
GB  
GDSTN  
BONN  
ORBITER 1 ( $i = 0^\circ, \omega = 0^\circ, \Omega = 0^\circ$ )  
ORBITER 2 ( $i = 90^\circ, \omega = 0^\circ, \Omega = 90^\circ$ )



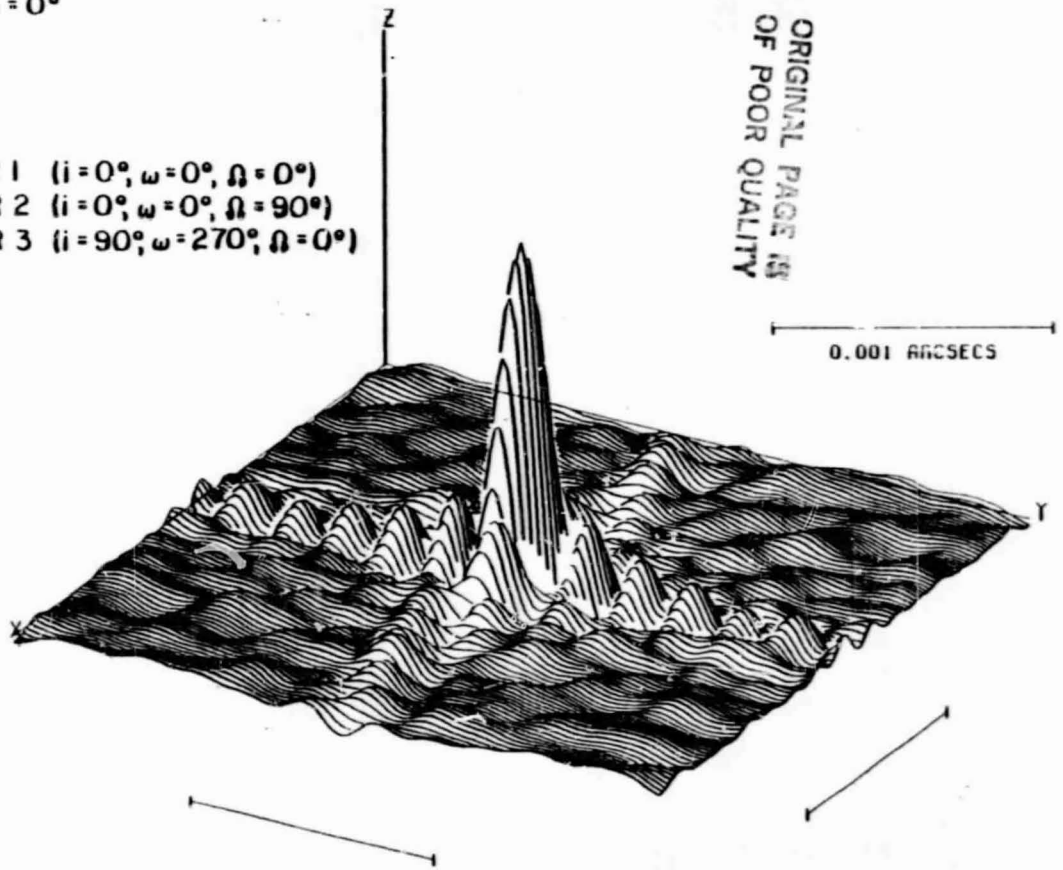
ORIGINAL PAGE IS  
OF POOR QUALITY

Figure V-1g

Figures V-2. Simulations of VLB observations with three highly-elliptical spacecraft orbits. In all cases the orbits are those described in Table V-1, and the seven source directions are spaced around the celestial equator and into the Northern celestial hemisphere in such a way as to get a good sample of the (u-v) coverage which is generated. The angular scale assumes an observing wavelength of 18 cm ( $\nu = 1.665$  GHz).



$\alpha = 0^h, \delta = 0^\circ$   
 GB  
 GDSTN  
 BONN  
 ORBITER 1 ( $i = 0^\circ, \omega = 0^\circ, \Omega = 0^\circ$ )  
 ORBITER 2 ( $i = 0^\circ, \omega = 0^\circ, \Omega = 90^\circ$ )  
 ORBITER 3 ( $i = 90^\circ, \omega = 270^\circ, \Omega = 0^\circ$ )



ORIGINAL PAGE IS  
 OF POOR QUALITY

Figure V-2a

V (/VMAX)

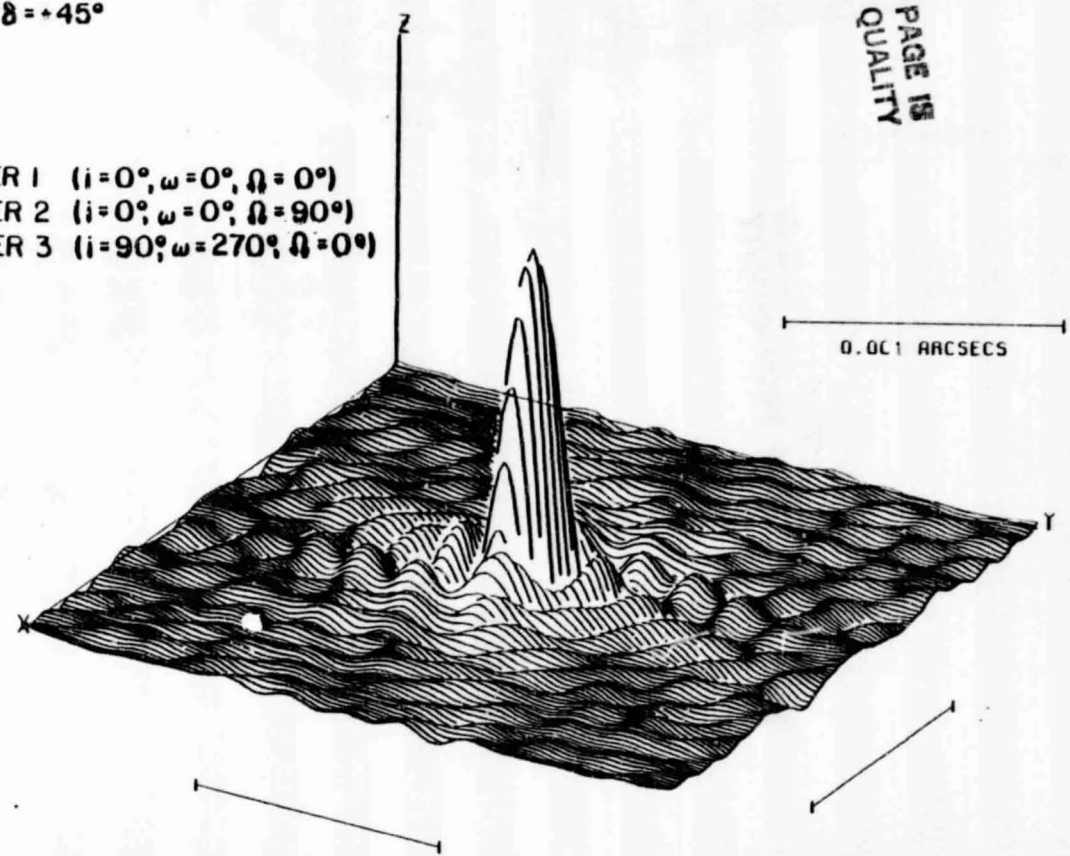
C-2



U (/UMAX)

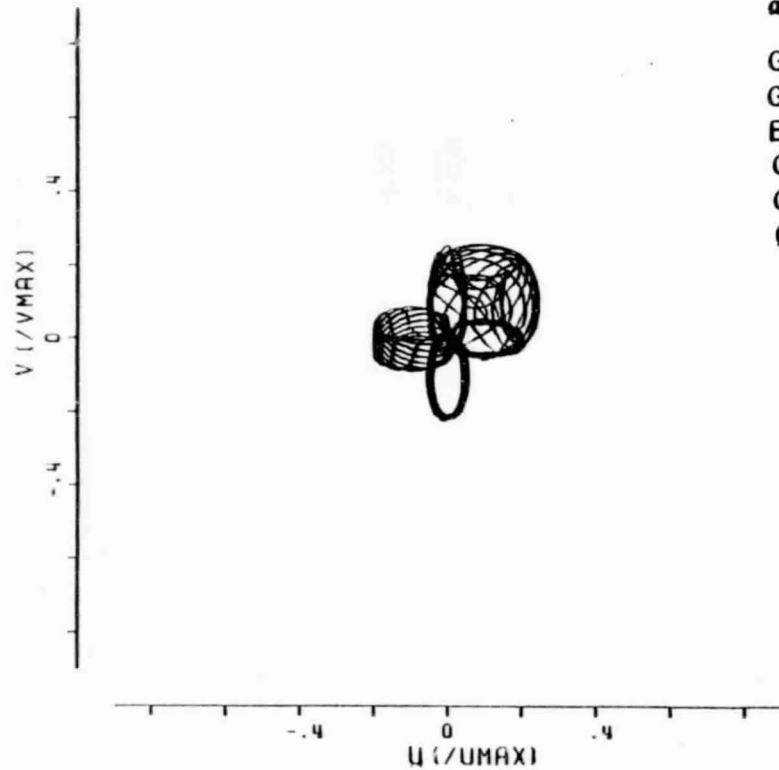
$\alpha = 0^h, \delta = +45^\circ$

- GB
- GDSTN
- BONN
- ORBITER 1 ( $i=0^\circ, \omega=0^\circ, \Omega=0^\circ$ )
- ORBITER 2 ( $i=0^\circ, \omega=0^\circ, \Omega=90^\circ$ )
- ORBITER 3 ( $i=90^\circ, \omega=270^\circ, \Omega=0^\circ$ )



ORIGINAL PAGE IS  
OF POOR QUALITY

Figure V-2b



$$\alpha = 0^h, \delta = +90^\circ$$

GB  
GDSTN  
BONN

ORBITER 1 ( $i = 0^\circ, \omega = 0^\circ, \Omega = 0^\circ$ )  
ORBITER 2 ( $i = 0^\circ, \omega = 0^\circ, \Omega = 90^\circ$ )  
ORBITER 3 ( $i = 90^\circ, \omega = 270^\circ, \Omega = 0^\circ$ )

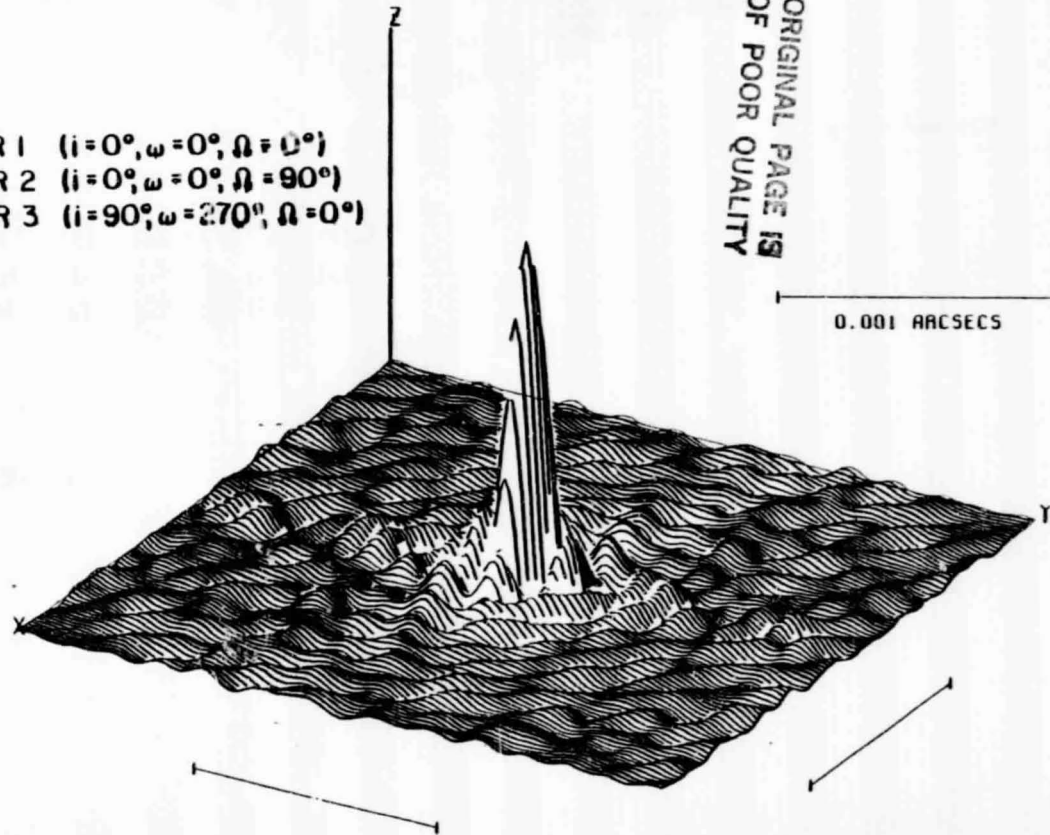
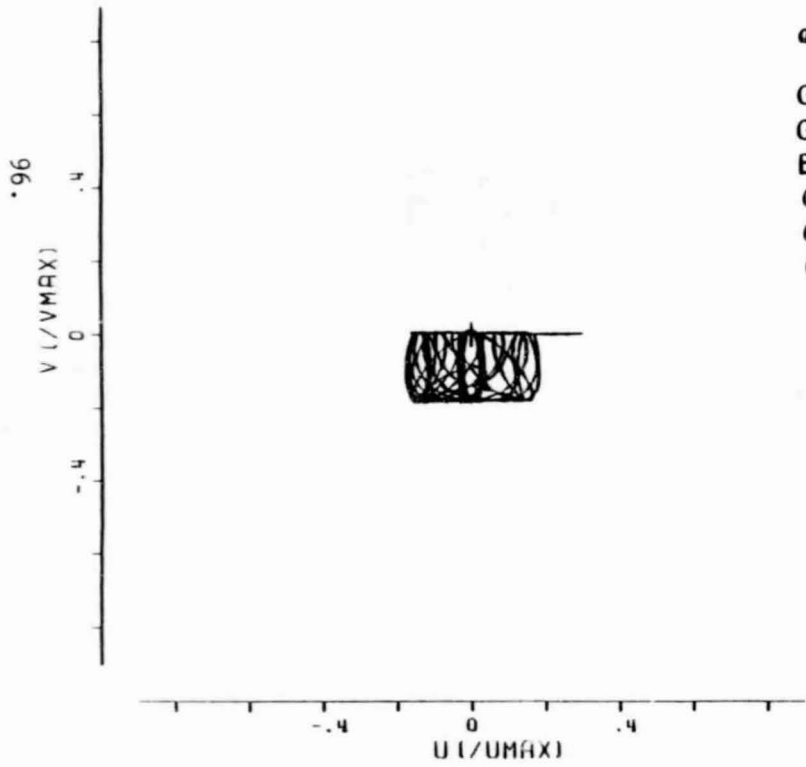


Figure V-2c

ORIGINAL PAGE IS  
OF POOR QUALITY



$$a = 3^h, \delta = 0^\circ$$

GB  
GDSTN  
BONN

- ORBITER 1 ( $i = 0^\circ, \omega = 0^\circ, \Omega = 0^\circ$ )
- ORBITER 2 ( $i = 0^\circ, \omega = 0^\circ, \Omega = 90^\circ$ )
- ORBITER 3 ( $i = 90^\circ, \omega = 270^\circ, \Omega = 0^\circ$ )

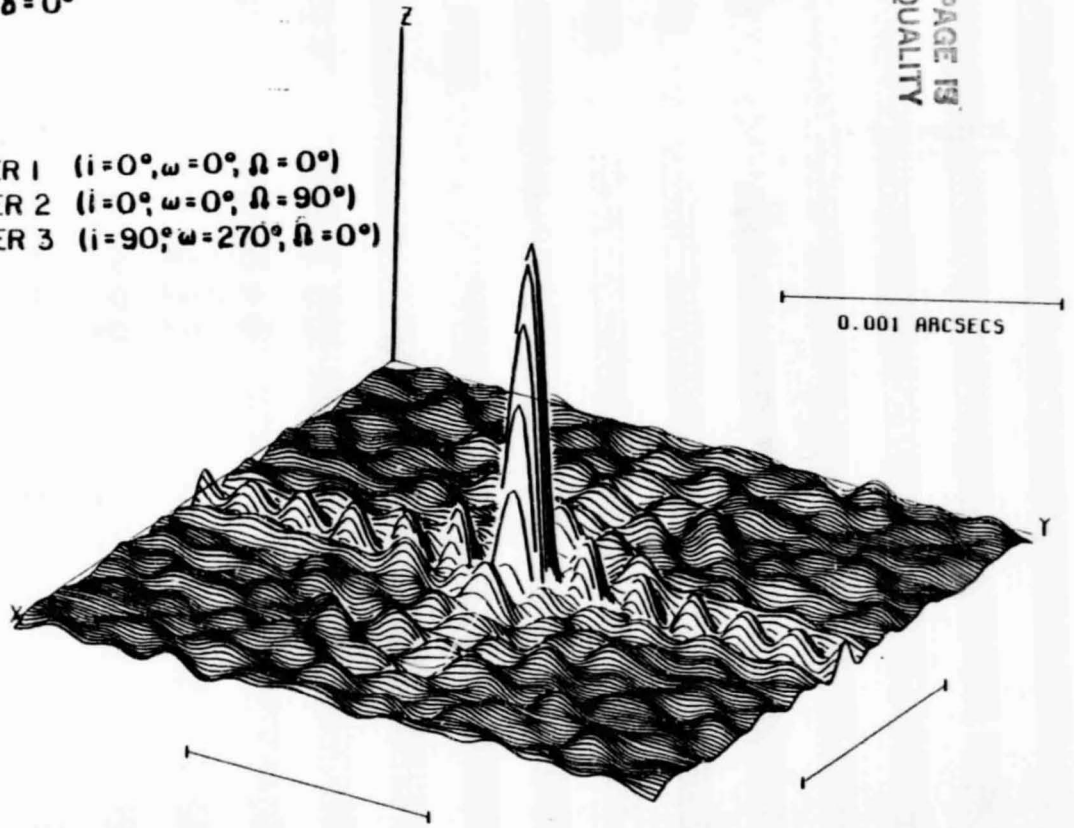


Figure V-2d

ORIGINAL PAGE IS  
OF POOR QUALITY

$$a = 3h, \delta = +45^\circ$$

- GB
- GDSTN
- BQNN
- ORBITER 1 ( $i = 0^\circ, \omega = 0^\circ, \Omega = 0^\circ$ )
- ORBITER 2 ( $i = 0^\circ, \omega = 0^\circ, \Omega = 90^\circ$ )
- ORBITER 3 ( $i = 90^\circ, \omega = 270^\circ, \Omega = 0^\circ$ )

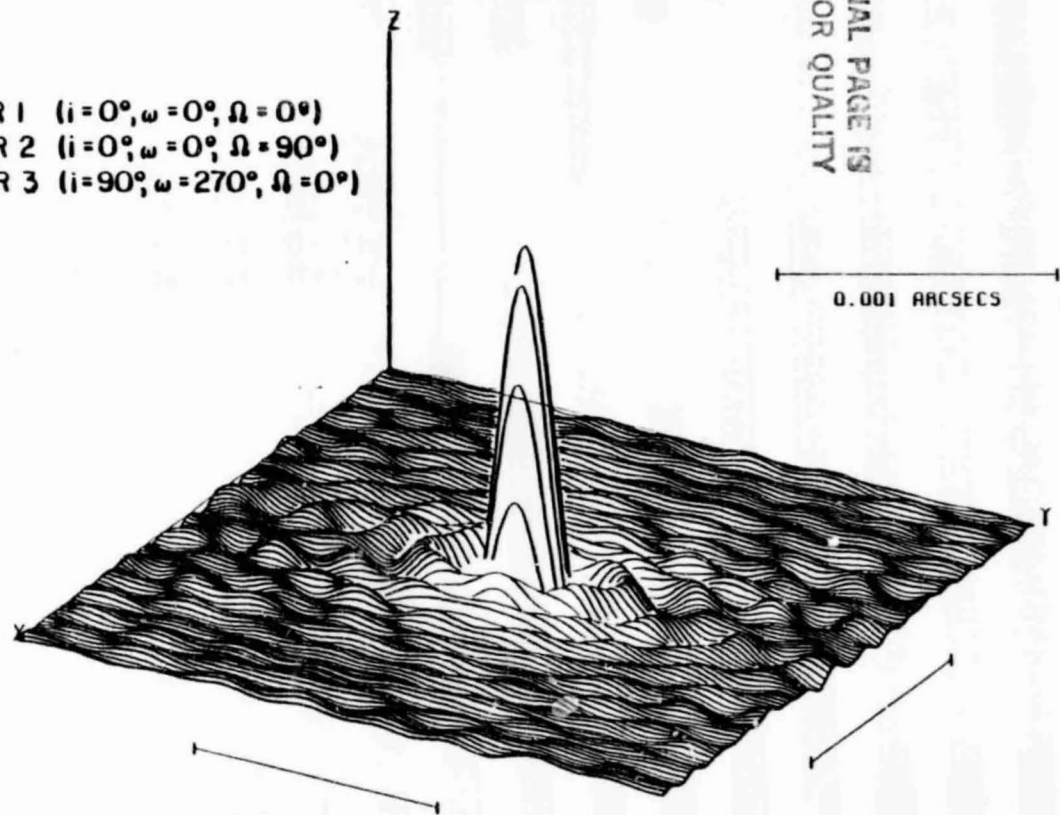
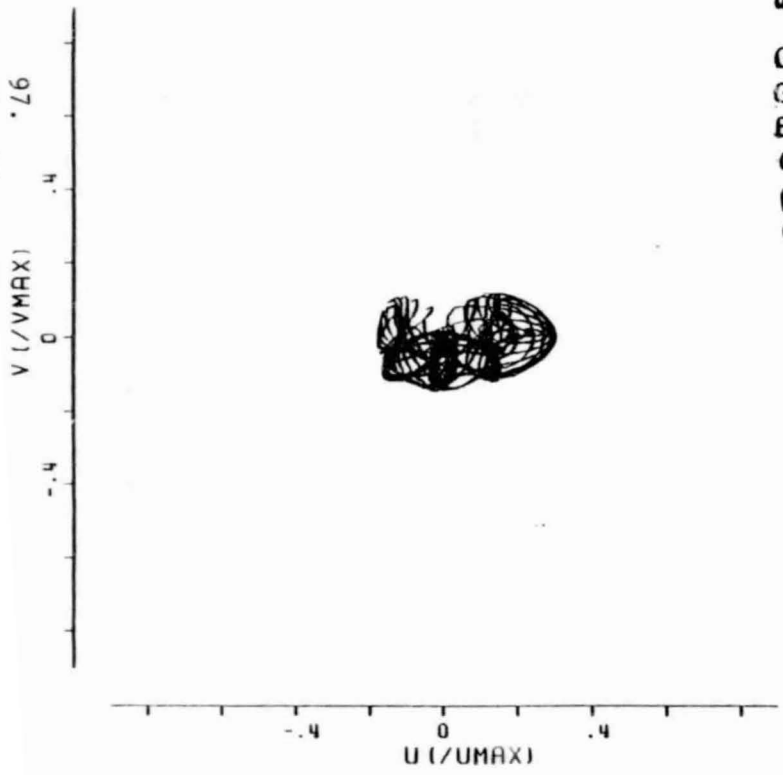
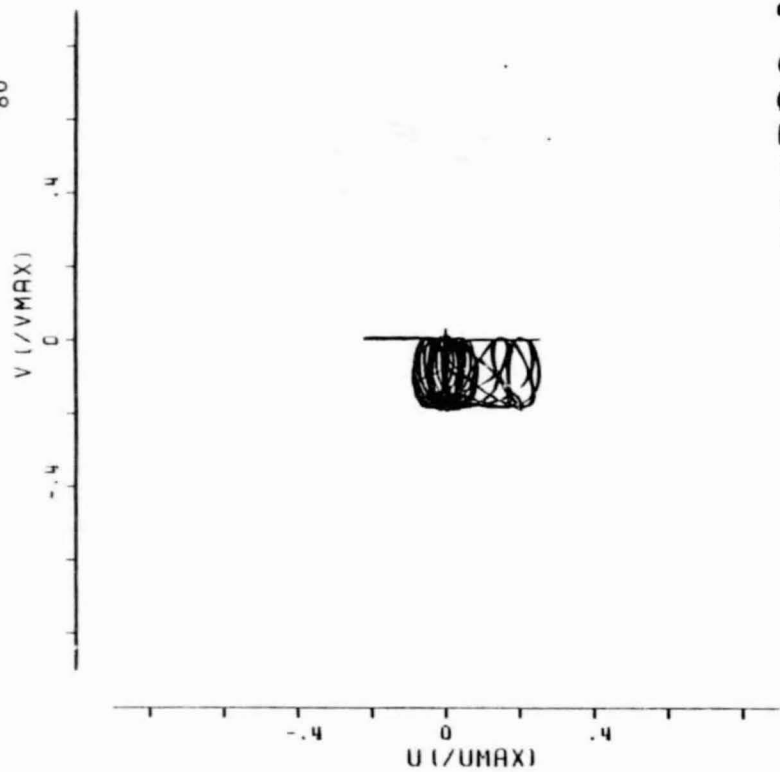


Figure V-2e

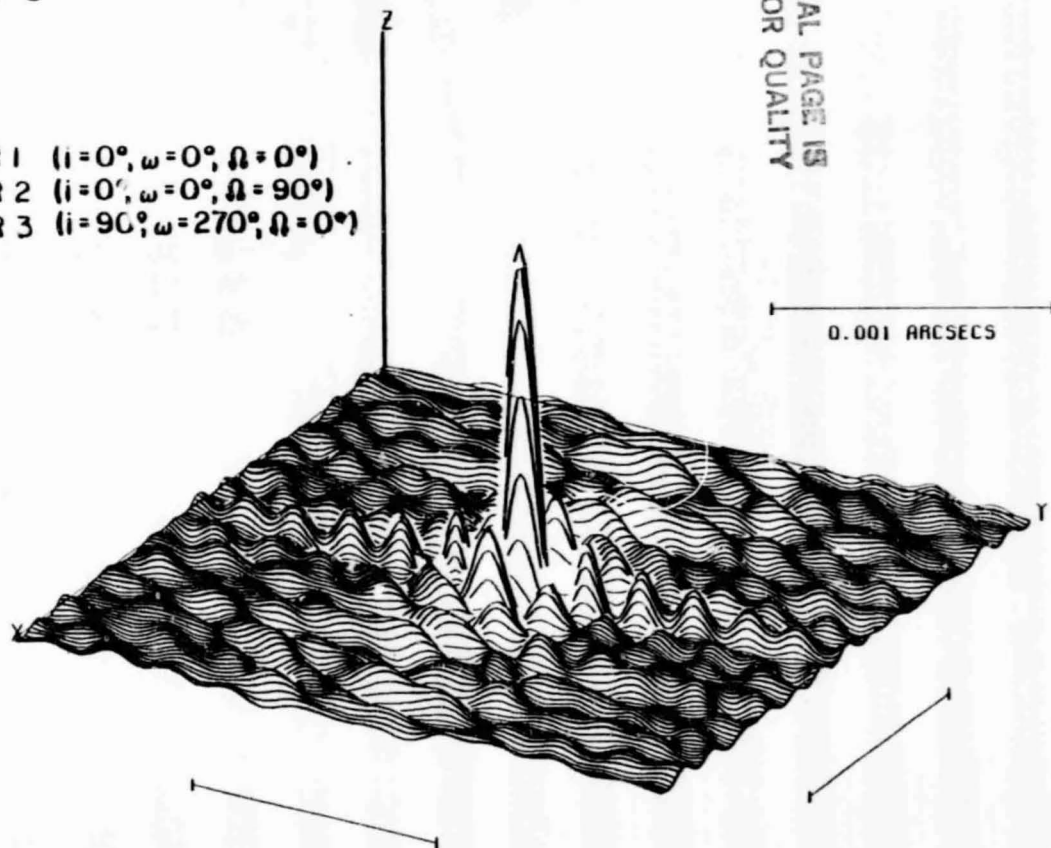


$$\alpha = 6h, \delta = 0^\circ$$

GB

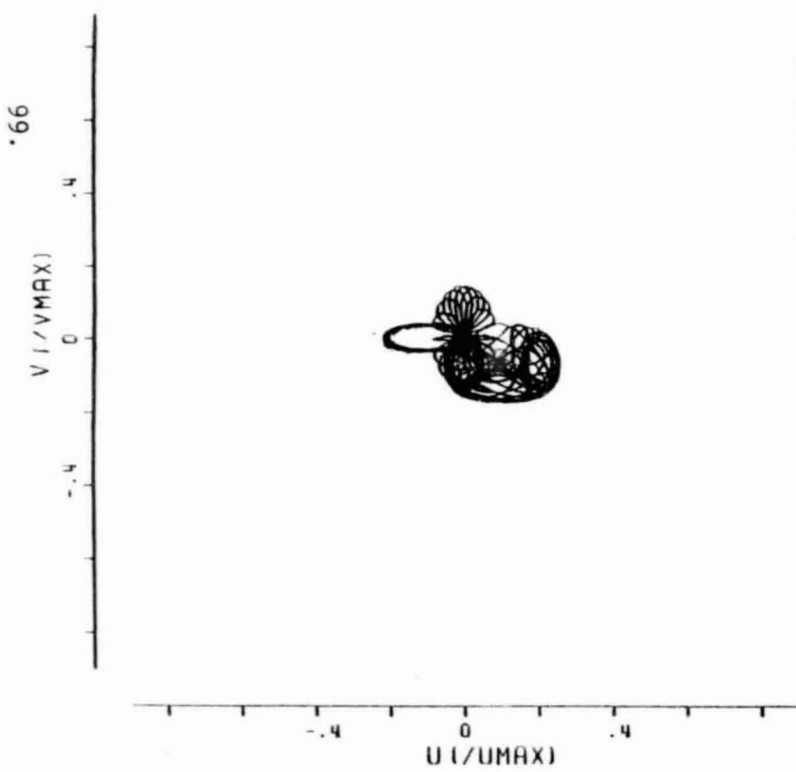
GDSTN

BONN

ORBITER 1 ( $i = 0^\circ, \omega = 0^\circ, \Omega = 0^\circ$ )ORBITER 2 ( $i = 0^\circ, \omega = 0^\circ, \Omega = 90^\circ$ )ORBITER 3 ( $i = 90^\circ, \omega = 270^\circ, \Omega = 0^\circ$ )

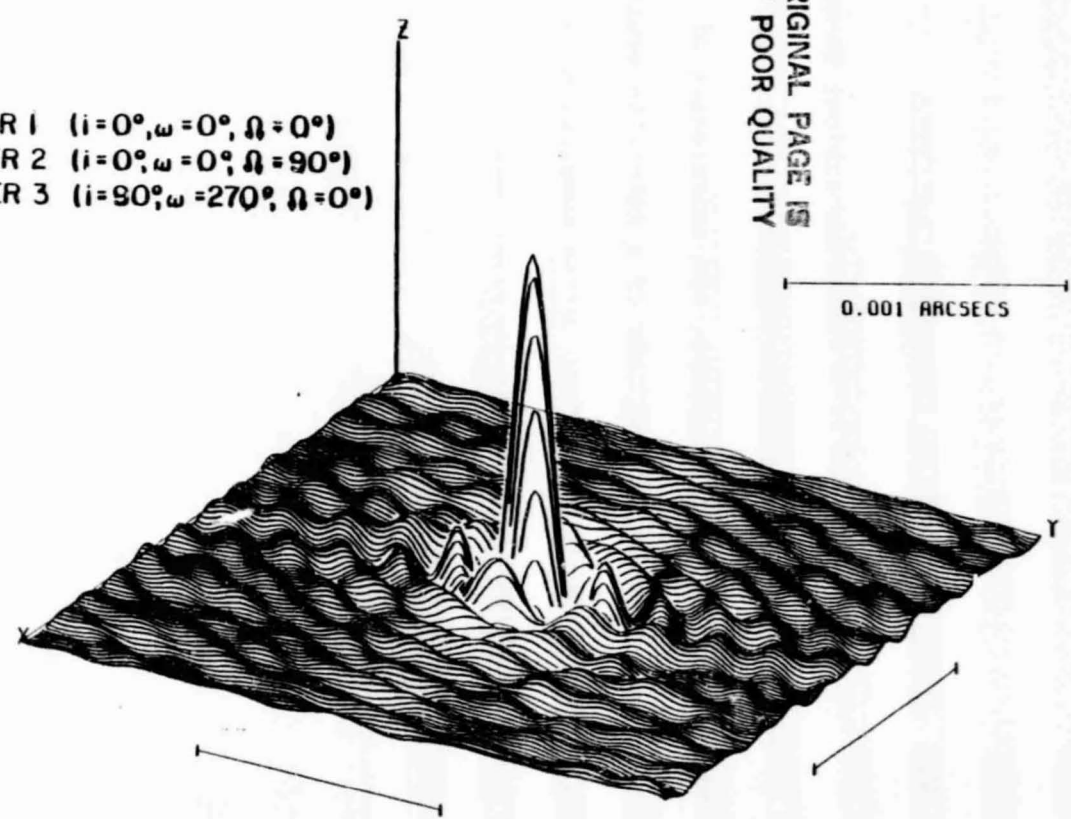
ORIGINAL PAGE IS  
OF POOR QUALITY

Figure V-2f



$\alpha = 6^h, \delta = +45^\circ$

- GB
- GDSTN
- BONN
- ORBITER 1 ( $i=0^\circ, \omega=0^\circ, \Omega=0^\circ$ )
- ORBITER 2 ( $i=0^\circ, \omega=0^\circ, \Omega=90^\circ$ )
- ORBITER 3 ( $i=90^\circ, \omega=270^\circ, \Omega=0^\circ$ )



ORIGINAL PAGE IS  
OF POOR QUALITY

Figure V-2g

## VI. EFFECTS OF ORBITAL PRECESSION AND DECAY

In the ideal case of a satellite subject to only the gravitational attraction of a spherically-symmetric planet, the five elements  $(a, e, \Omega, \omega, i)$  which specify the size, shape, and orientation of its orbit are independent of time. However, in the case of a satellite orbiting the Earth at finite altitude, several additional forces complicate the picture and cause all of these elements to change in time. Here we will be concerned with only two most important forces, (i) the gravitational forces that arise because of the non-sphericity of the Earth and because of the presence of the sun and the moon, and (ii) the aerodynamic forces due to the Earth's upper atmosphere. As we show below, these additional gravitational forces affect  $\Omega$  and  $\omega$ , resulting in very useful slow changes in orbital orientation. The atmospheric drag, on the other hand, results in orbital decay and the eventual reentry of near-Earth satellites, and must therefore be understood and minimized if a long-lasting ( $\geq$  months) mission is anticipated.

The effect of the non-sphericity of the Earth and the attraction of the sun and moon is to produce an effectively non-invers-square-law gravitational force. For near-Earth orbits the effects of the sun and moon are relatively unimportant, resulting in regression of the nodes ( $\dot{\Omega} < 0$ ) and precession of the apsides ( $\dot{\omega} > 0$ ) at these rates:

	Moon	Sun
$\dot{\Omega}$	$-1^{\circ}05/\text{yr}$	$-0^{\circ}43/\text{yr}$
$\dot{\omega}$	$+1^{\circ}32/\text{yr}$	$+0^{\circ}54/\text{yr}$

Although these effects would of course be important for the precise spacecraft tracking and location needed for VLBI, they are of little importance (or utility) for the overall plan of a near-Earth space VLBI mission. The first-order deviation from the sphericity of the Earth, described by its quadrupole moment (dimensionless) of

$$J_2 \approx 1.63 \times 10^{-3},$$

causes regression of the nodes and precession of the apsides at the rates

$$\dot{\Omega} = \frac{-2\pi}{T} J_2 \cos i \left(\frac{R}{a}\right)^2 (1-e^2)^{-2}$$

and

$$\dot{\omega} = \frac{2\pi}{T} \frac{1}{2} J_2 (5\cos^2 i - 1) \left(\frac{R}{a}\right)^2 (1 - e^2)^{-2},$$

where R is the Earth's radius and T the satellite's period. Using Kepler's third law to eliminate T and inserting numerical values these become

$$\dot{\Omega} = -10.2 \left(\frac{R}{a}\right)^{7/2} \cos i (1-e^2)^{-2} \text{ revolutions/year,}$$

$$\dot{\omega} = +5.08 \left(\frac{R}{a}\right)^{7/2} (5\cos^2 i - 1) (1-e^2)^{-2} \text{ revolutions/year.}$$

For a circular orbit  $\dot{\omega}$  is irrelevant (and undefined), but the effect of regression of the nodes is substantial, because it changes the orientation of the orbit with respect to the sky. In Figure VI-1 we have plotted  $\dot{\Omega}$  versus altitude  $h = a - R$  for near-Earth circular orbits of various inclinations. Note that orbits with  $i < 90^\circ$  regress, those with  $i = 90^\circ$  have stationary nodes, and those with  $i > 90^\circ$  (retrograde orbits) precess. The most useful near-Earth orbits for space VLBI have  $i \approx 57^\circ$  (or  $i = 180^\circ - 75^\circ = 123^\circ$ ) in order to optimize the resolution of maps made at all possible declinations (see § VII). Orbits available directly from the Space Shuttle range in inclination from  $28^\circ$  to  $57^\circ$  (for Kennedy launch). The altitudes obtainable depend on payload and on the number of OMS units used (one integral unit plus zero to three additional OMS units), and range from  $\sim 280$  to  $\sim 1000$  km. The maximum payload falls roughly linearly from  $\sim 22000$  kg to zero over this altitude range, and depends weakly on inclination, lower inclinations enabling larger payloads. Over this entire range of orbits the nodal precession ranges from  $-7.8$  revolutions/year ( $h = 270$  km,  $i = 28^\circ$ ) to  $-3.3$  revolutions/year ( $h = 1000$  km,  $i = 57^\circ$ ). Thus any near-Earth mission entails an orbit which precesses a full  $360^\circ$  in between 47 and 111 days, and a nominal one does so in 81 days. This means that the orbit is oriented more or less face-on to every source in the sky several times each year. This is a great advantage for space VLBI, for it means that (1) sources anywhere in the sky can be well observed with any (high-inclination) near-Earth spacecraft orbit, and (2) a given source may be observed with the same optimum uv coverage several times per year. The second point is of great interest, for some of the most fascinating phenomena observed by VLBI involve rapid time variability.

Because of the sensitivity of the nodal precession rate to semi-major axis, orbits substantially larger than the ones observed above do not offer the same advantages. The locus in  $(i, h)$  -space of those circular orbits which precess ( $n > 0$ ) or regress ( $n < 0$ ) times per year,

$$- \cos i = \left( \frac{n}{10.2} \right) \left( 1 + \frac{h}{R} \right)^{7/2} ,$$

is plotted in Figure VI-2 for several values of  $n$ . The curves for  $n = \pm 1$  make a useful demarcation between fast and slow precession. At the inclinations best for VLBI,  $i \approx 57^\circ$  or  $123^\circ$ , such orbits are at an altitude of  $h \approx 0.63 R = 4030$  km. Much larger orbits, such as earth-synchronous ones ( $h \approx 42200$  km), have much slower precession rates ( $\dot{\Omega} \approx$  once per 23 years in the earth-synchronous case). However, there are larger orbits which precess at much faster rates due to the effects of lunar perturbations. The use of such orbits for space VLBI has been considered by the JPL group, and will not be discussed here.

The effect of the Earth's upper atmosphere on satellite orbits is to decrease all three elements  $a$ ,  $e$ , and  $i$ , and therefore also the period  $T$ . Because of the extreme sensitivity of these effects to the upper atmospheric density, and of the latter's large and unpredictable variations with slow conditions, a priori calculation of satellite lifetimes against changes in  $a$ ,  $e$  and  $i$  is not likely to be precise. However, the relevant time scale

behaves roughly as follows:

$$\tau_c \propto \left( \frac{H}{\rho_0} \right) \left( \frac{M}{A} \right) e^{h_0/H} \left( 1 - 2 \frac{h_0}{R} \right)$$

Here  $\tau_c$  is the time for decay to re-entry of a satellite in a circular orbit of initial altitude  $h_0$ ,  $(M/A)$  is the mass-to-area ratio of the satellite, and the atmosphere is assumed to have density scale length  $H$  and ground-level density  $\rho_0$ . If the orbit is initially elliptical, then the first effect will be a circularization of the orbit by decay of the apogee due to energy loss at perigee, a process that always takes longer than the subsequent decay of the circular orbit that results. In addition, a satellite initially inclined at  $|i| > 0$  will suffer a decay toward  $i = 0$ .

The lifetime of a satellite depends very sensitively on its initial altitude. In the range of Space Shuttle orbits the equivalent atmospheric scale height is between 35 and 70 km, so that a change in initial altitude of  $\Delta h_0$  results in an increase of at least a factor of  $e^{\Delta h_0/70 \text{ km}}$  in lifetime. Thus the difference between  $h = 270 \text{ km}$  and  $h = 400 \text{ km}$  is at least a factor of 6 in orbital lifetime. The actual lifetimes would depend on the mass-to-area ratio of the specific satellite, but it seems likely that an orbit in the 400 km range would be suitable for a mission of several months duration. A lifetime of years would require either a higher initial orbit or periodic visits and orbital adjustments by the Space Shuttle.

Figure VI-1. Rate of nodal precession for near-Earth orbits, for various orbital inclinations.

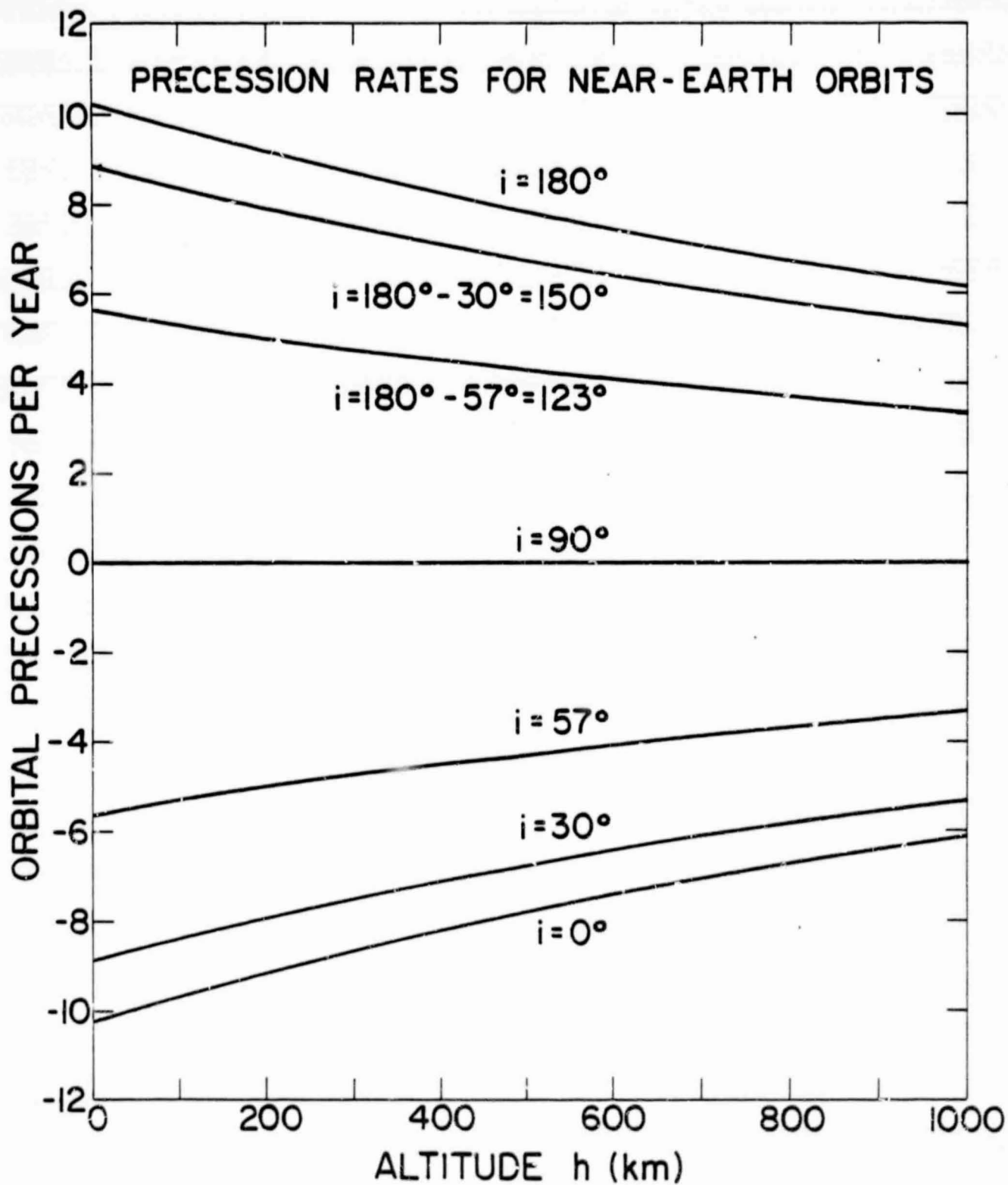


Figure VI-1

Figure VI-2. Number of complete nodal precessions per year ( $n$ ) as a function of orbital altitude ( $h$ ) and inclination ( $i$ ).

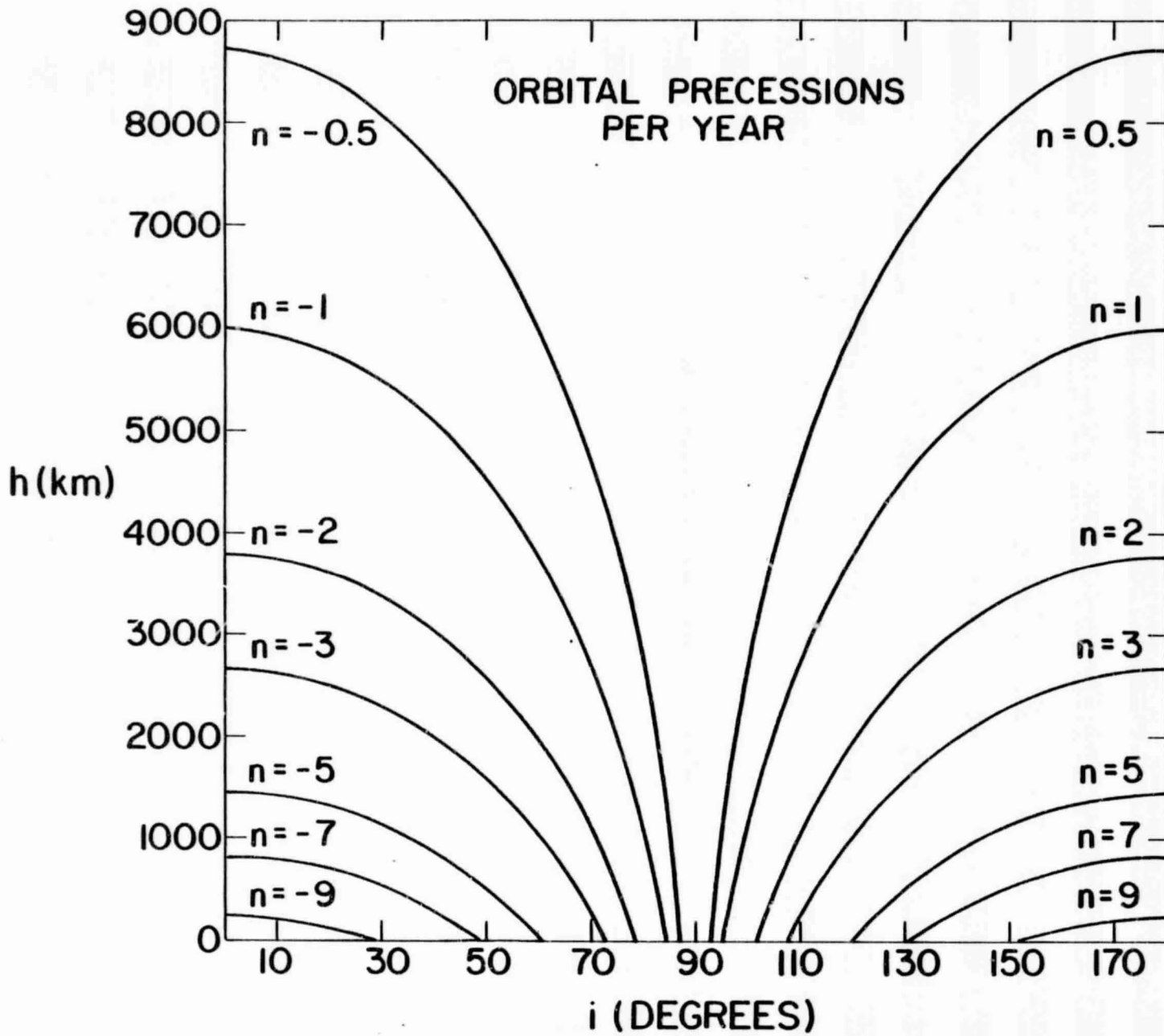


Figure VI-2

## VII. CHOICE OF A "BEST" ORBITAL INCLINATION

In this section we address the question, "Is there a single optimum orbit for a near-Earth orbiting VLBI station?" From the results of §IV we know that for a given source position, an orbit that is face-on to a given source produces the overall superior synthesized beam. In addition, from §VI we know that near-Earth orbits precesses with respect to the stars a few full revolutions per year. This means that the optimum  $\Omega$  for a given source will occur several times each year, and therefore the specification of the initial value  $\Omega_0$  is unimportant for missions lasting a few months or more. Thus the orbital inclination  $i$  is the only degree of freedom, and the question becomes "Is there a single inclination  $i_{opt}$  that produces the "best" overall results for sources at all possible locations?" As we show below, for a very reasonable definition of "best overall results" the answer is in the affirmative, and the value of  $i_{opt}$  that we obtain is surprisingly convenient.

For a source at given coordinates  $(\alpha, \delta)$ , a face-on near-Earth circular orbit has the elements

$$\Omega_{\alpha} = \alpha + \frac{\pi}{2},$$

$$i_{\delta} = \frac{\pi}{2} - \delta.$$

The angle between the normal to this best orbit for this source and the normal to an orbit at inclination  $i$ , at the time when  $\Omega = \Omega_{\alpha}$ , is

$$\eta = i - i_\delta = i + \delta - \frac{\pi}{2}.$$

The result of  $i \neq i_\delta$  is that the North-South extent of the synthesized beam made with such an orbit will increase as the v-orbital projection decreases:

$$\delta\theta_{NS} \propto 1/\cos \eta = 1/\sin(i + \delta).$$

On the other hand, as long as  $\Omega \approx \Omega_\alpha$ , the east-west beam width will not depend on  $i$ . Thus the solid angle of the beam will vary with  $(i, \delta)$  as

$$\delta\Omega \propto \delta\theta_{NS} \propto 1/\sin(i + \delta).$$

If we now define the "quality" of the beam to be inversely proportional to its solid angle,

$$Q_1 \equiv 1/\delta\Omega \propto \sin(i + \delta),$$

so that  $Q_1$  is proportional to the number of beam areas in a synthesized map, we may find an overall optimum inclination  $i_{opt}$  by maximizing the integrated quality of all the possible maps we could make with respect to  $i$ . Since the number of sources of declination  $\delta$  is proportional to the

area of sky at that declination, so that

$$\frac{dn}{d\delta} \propto \cos \delta,$$

the "integral quality" of maps made at all possible directions on the sky is proportional to

$$I_1 = \int_0^{\pi/2} d\delta \frac{dn}{d\delta} Q_1(i, \delta) = \int_0^{\pi/2} d\delta \cos \delta \sin(i + \delta).$$

The condition that there be a single optimum orbital inclination is that

$$\frac{\partial I_1}{\partial i} = 0, \quad \frac{\partial^2 I_1}{\partial i^2} < 0.$$

Using the identity

$$\sin(a + b) = \sin a \cos b + \cos a \sin b,$$

we easily find that

$$\begin{aligned} I_1(i) &= \sin i \int_0^{\pi/2} \cos^2 \delta \, d\delta + \cos i \int_0^{\pi/2} \sin \delta \cos \delta \, d\delta \\ &= \frac{\pi}{4} \sin i + \frac{1}{2} \cos i. \end{aligned}$$

Thus the condition of maximum becomes

$$\left( \frac{\partial I_1}{\partial i} \right)_{i_{\text{opt}}} = \frac{\pi}{4} \cos i_{\text{opt}} - \frac{1}{2} \sin i_{\text{opt}} = 0,$$

or

$$i_{\text{opt}_1} = \tan^{-1} \left( \frac{\pi}{2} \right) \approx 57.52$$

Since

$$\frac{\partial^2 I_1}{\partial i^2} = -\frac{\pi}{4} \sin i - \frac{1}{2} \cos i,$$

it is clear that a maximum is achieved, since

$$\frac{\partial^2 I_1}{\partial i^2} < 0, \quad 0 < i < \frac{\pi}{2}.$$

A most remarkable fact about this result is that such an orbit is just the orbit of largest inclination obtainable from a Florida launch of the Space Shuttle. In addition, and more importantly, the curve  $I_1(i)$  is quite broad about its peak. This is illustrated in Figure VII-1, where we plot  $I_1(i)$ . In fact, any inclination in the range

$$32.0^\circ \leq i \leq 83.5$$

has  $I_1$  within 10% of its maximum value. Thus the "integrated quality" of maps made at all locations on the sky is not very sensitive to orbital inclination, as long as it is above about  $30^\circ$ .

In Figure VII-1 we also plot the ratio of N - S beamwidth for a source of declination  $\delta$  using an orbit of  $i_{opt_1}$  to the possible N - S beamwidth (that obtained at  $i = i_\delta = \pi/2 - \delta$ ),

$$\frac{\Theta_{ns}(i, \delta)}{\Theta_{ns}(i_\delta, \delta)} = \frac{1}{\sin(i + \delta)},$$

as a function of  $\delta$  for several  $i$ . In the case  $i = i_{opt_1} \approx 57^\circ 52'$  the N - S extent of the beam is never more than  $(1 + \frac{\pi^2}{4})^{1/2} \approx 1.86$  times its minimum. At the important region near  $\delta \approx 0^\circ$  the ratio is only  $\frac{2}{\pi} (1 + \frac{\pi^2}{4})^{1/2} \approx 1.19$ . Were we to choose  $i = 45^\circ$ , the maximum increase in N - S beamwidth is  $1/\cos 45^\circ = \sqrt{2} \approx 1.41$  (occurring at  $\delta = 0$  and  $\delta = 90^\circ$ ), and the integrated quality  $I(i = 45^\circ)$  is only 2.4 percent less than the maximum  $I(i = i_{opt})$ . We see that excellent results are obtainable from a wide variety of orbital inclinations.

An alternate definition of quality which weights smaller beams more heavily,

$$Q_2 \propto (\text{solid angle})^{-2} \propto \sin^2(i + \delta),$$

equivalent to the square of the number of picture elements,

leads to

$$I_2(i) = \int_0^{\pi/2} d\delta \cos\delta \sin^2(i + \delta);$$

changing variables to

$$x = i + \delta$$

and using the identity

$$\cos(a-b) = \cos a \cos b + \sin a \sin b$$

we find directly that

$$\frac{\partial I_2}{\partial i}_{\text{opt}} = \int_i^{i+\pi/2} dx \left\{ \cos i [\sin x \cos^2 x] + \sin i [\sin^2 x \cos x] \right\}.$$

The condition  $\partial I / \partial i_{\text{opt}} = 0$  can then be reduced to

$$\frac{3}{2} I_2' = \cos i \sin^3 i + \sin i \cos^3 i + \cos^4 i - \sin^4 i = 0,$$

which is equivalent to

$$\tan^4(i) - \tan^3(i) - \tan(i) - 1 = 0 .$$

The only physical solution of this quartic equation is

$$i_{\text{opt}_2} = \cos^{-1} \left( \frac{5 - \sqrt{5}}{10} \right)^{1/2} \approx 58^\circ 28,$$

which corresponds to a maximum of  $I_2$ . In this case the peak of  $I_2(i)$  is not quite as wide, but  $I$  remains within 10% of its peak value for

$38^\circ 5 \leq i \leq 79^\circ 0$  (see Figure VII-1). The ratio of beamwidth at inclination

$i_{\text{opt}_2}$  to that at the best inclination for a given source is very similar to

that for the other choice of  $Q$ , and has a worst value (at  $\delta = 90^\circ$ ) of only

$$\left( \frac{10}{5 - \sqrt{5}} \right)^{1/2} \approx 1.90, \text{ and an equatorial } (\delta = 0^\circ) \text{ value of } \left( \frac{10}{5 + \sqrt{5}} \right)^{1/2} \approx 1.18.$$

We conclude that any orbit with inclination satisfying

$$40^\circ \leq i \leq 60^\circ,$$

with a slight preference for

$$i \approx 57^\circ,$$

will yield excellent overall results, and will not severely compromise any region of the sky.

Figure VII-1. Integrated "quality" of synthesized maps of sources distributed over the sky, as a function of the orbital inclination  $i$  of the spacecraft VLB terminal. Also shown is the ratio of North-South, to East-West beamwidth for synthesis performed for a source of declination  $\delta$  using various satellite inclinations  $i$ .

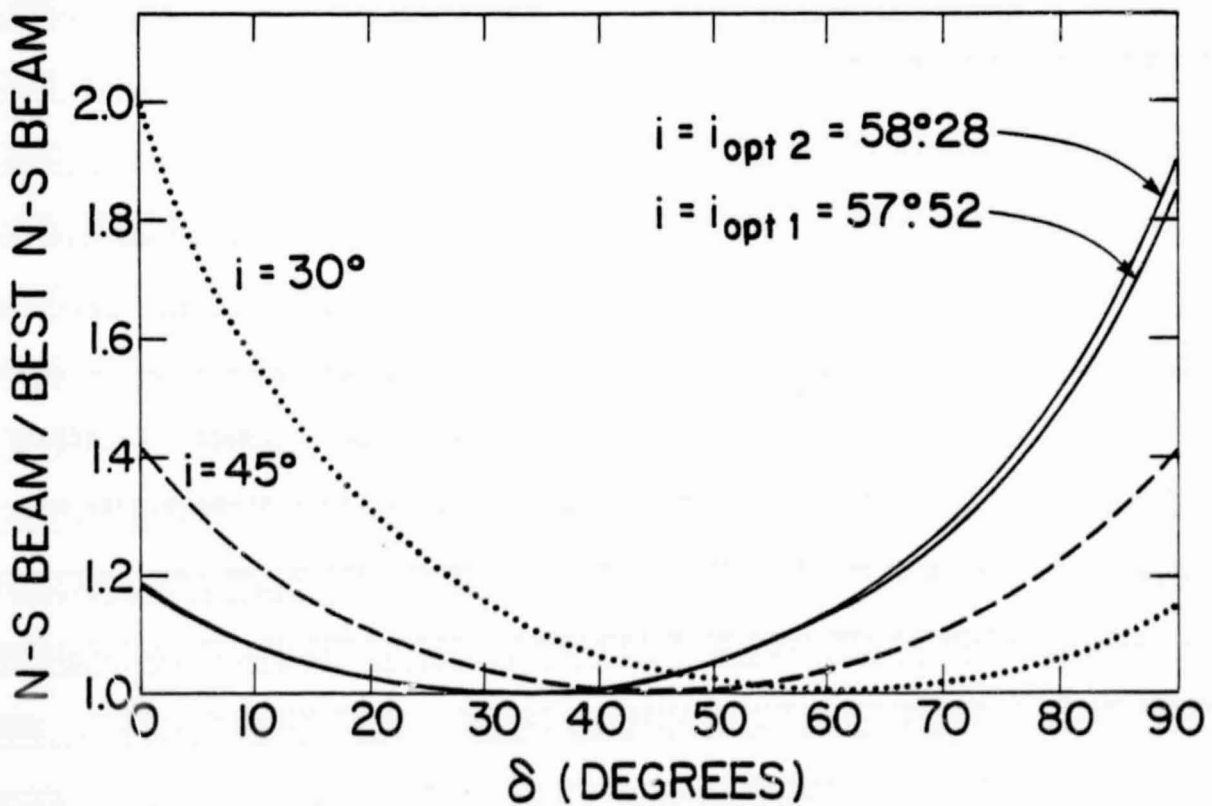
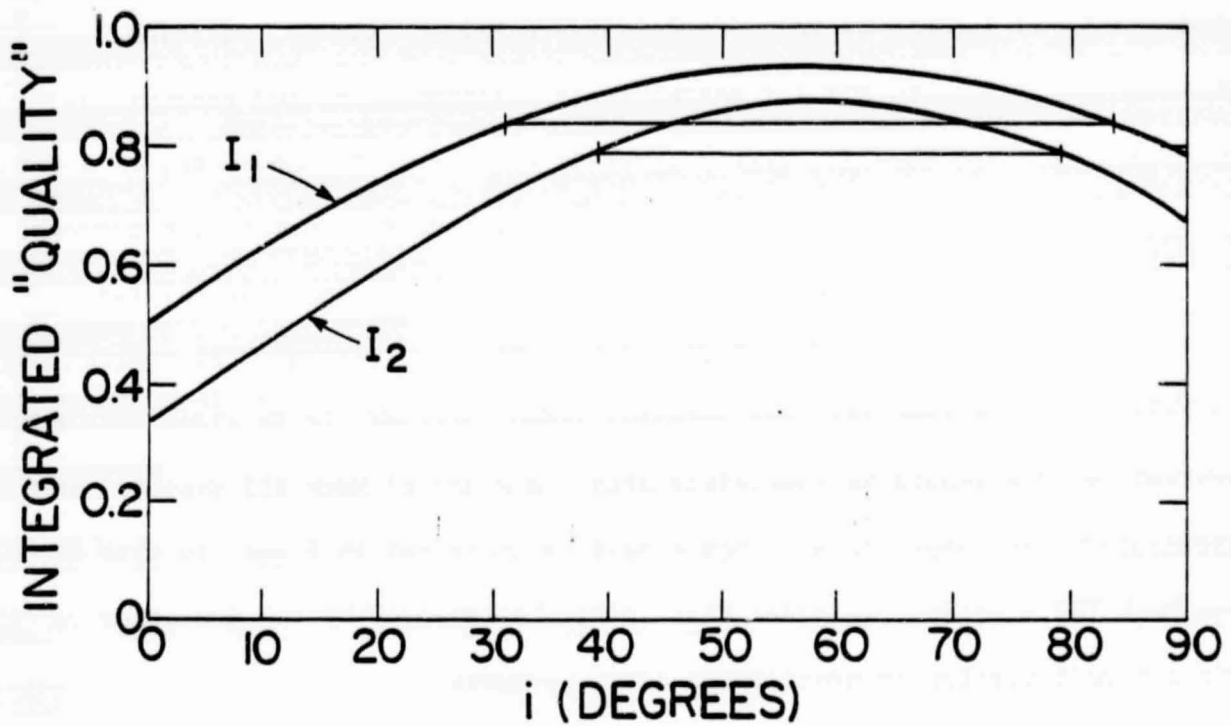


Figure VII-1

## VIII. CONSTRAINTS ON DATA ACQUISITION, HANDLING, AND PROCESSING

### A. Mark III System

The Mark III system is a digital data recording and processing system for VLBI developed jointly by NASA (Goddard Space Flight Center), Haystack Observatory, NRAO, and MIT for astrophysical, astrometric, and geophysical observations. The Mark III system consists of two major components, 1) a set of identical data recording stations, one at each observatory in the network, and 2) a special purpose processor, located at Haystack Observatory, for replaying, correlating, and analyzing data. Since an orbital VLBI station would be used in conjunction with the existing ground systems, it is clear that the orbital station should be compatible with the standard Mark III system. In particular, the output data stream should be identical in format to that of the Mark III stations, in order that it may be replayed by the processor without modification or addition of extra hardware.

### B. Mark III Recording Stations

The Mark III recording stations each contain an IF distributor, 14 video converters, a data formatter, and a 28 track instrumentation tape recorder. At each station the IF distributor is supplied with a stable 5 MHz clock and the IF signal from the telescope. The built-in local oscillators in the converters have a range of 100-500 MHz in 10 kHz steps. Each converter produces an upper and lower sideband output video signal. The video output bandwidth is selectable with 4, 2, 1, .5, .25 and .125 MHz being available. Each video signal is clipped and one-bit sampled at the Nyquist frequency, twice the bandwidth. If the output voltage at the time of a sample is positive the bit is a "1", if negative, a "0".

Each of the 28 digital data streams is then sent to the data formatter. The formatter adds parity bits (1 per byte) and sync blocks. The sync blocks contain words for identification of the blocks, the time of the first sample of the block, and an error checking code for the block. These blocks are inserted in each data channel, insuring that each channel can be analyzed independently. Each channel of data is recorded on one track of the 28 track tape recorder. Because of the addition of a parity bit each byte, the recording rate per track is 9/8 the sampling rate.

### C. Mark III Processor

The data tapes made at each of the recording stations are brought to Haystack Observatory for processing. The Mark III processor consists of a modular special purpose hardware correlator and a host computer which controls the processing. Tapes from three stations can be processed simultaneously. The 28 data streams from each of the 3 tapes are routed in such a way that each of 84 modules receives a baseline-track pair of data streams. In general, the data can be processed at the same rate it was taken. Each module cross-correlates its data streams over relatively short ( $\leq 2$ s) intervals, known as parameter periods, passing the results for each period to a disk file via the host computer. The host computer provides each module with the appropriate input parameters for processing each interval, namely the time delay, delay rate, fringe rate and fringe acceleration. Upon completion of the correlation processing, the output records are searched for fringes by software routines running on the host computer. The correlator processing step reduces the data volume by a factor of  $\sim 10^5$ . The major requirement for a

successful fringe search is that the parameters used by the hardware correlator be sufficiently close to the correct values so that the fringes are not lost due to loss of coherence or to smearing in time.

Figure VIII-1 is a block diagram of a correlator module. Each of the two input data streams is passed through decoders, which remove sync blocks, time tags and parity bits, restoring the data stream to radio source data only. The time tags are used to properly synchronize the two tape drives. The X-data stream then passes through a programmable delay buffer. This buffer, using parameters passed from the host computer, makes the final adjustment in delay between the two streams to compensate for the geometrical delay,  $\tau_g$ , between the two recording stations. Due to the Earth's rotation, the time delay varies during a parameter period. The delay can be incremented or decremented by one data sample interval 15 times per parameter period, with the update intervals specified by the host computer.

The host computer also supplies the fringe rate,  $\dot{\phi}$ , and fringe acceleration  $\ddot{\phi}$ , to the module. These are then used to generate 3-level approximations to sine and cosine functions with periods equal to the fringe period which each multiply the Y data stream. The cosine and sine streams are then cross correlated with the delayed X stream at 8 different lags, resulting in 8 complex cross correlations. These cross correlations are accumulated for a parameter period and the resulting sums are output to the host computer for storage in a disk file. The fringe phase model,  $\phi$  and  $\ddot{\phi}$ , must be sufficiently accurate that the difference between the predicted and actual fringe phase does not change by more than a fraction of a rotation during a parameter period.

#### D. Orbital Stations

An essential requirement for performing useful VLBI observations is motion of the receiving antennae relative to one another. In current observations, this requirement is achieved by the rotation of the Earth on its axis. In VLBI observations involving one or more orbital receiving stations, the relative motions will be primarily a result of the orbital motions of the spacecraft carrying the stations. In general, this will result in higher relative velocities of the antennae, and it must be shown what effect these will have on the taking and analyzing of VLBI data. Furthermore, in order to analyze the data one must know, a priori, the relative motion of the antennae to certain accuracies. It must therefore also be shown that the relative motion of the orbital antennae can be determined to within the required tolerances. These tolerances, to some degree, will reflect the capabilities of the processing hardware and the amount of time that is considered reasonable to devote to analysis of the data. In this section we will discuss these issues with regard to the current capability of the Mark III VLBI Processor at Haystack.

The maximum relative velocity of a pair of antennae on the Earth along the line of sight to a source depends on antenna location and source direction. The worst case maximum relative velocity is 0.92 km/s for a pair of antennae on opposite sides of the Earth, on the equator, observing a source on the celestial equator. Relative velocities  $\leq 1/3$  this value are more typical. The maximum relative velocity that can be obtained with one of the antennae in orbit will depend on the particular orbit chosen for the spacecraft. Spacecraft in circular near Earth orbits (92 min orbital period) have orbital velocities of  $\sim 7.7$  km/s. Spacecraft in synchronous orbits have velocities of  $\sim 3$  km/s. (If a highly eccentric orbit is used, the majority of it will be

at relatively low velocities. When the spacecraft is near the Earth the velocities may be higher, but this portion of the orbit will be less useful for VLBI purposes and could be neglected.) The maximum likely relative velocity is therefore  $\sim 7.7 + .46 \approx 8$  km/s. Again, typical values for the projected line of sight velocities will be substantially smaller, and will average  $\sim 15$  times those obtained during strictly ground based observations.

#### E. Doppler Shift of Bandpass

The observing frequency for each channel is selected by the local oscillator and frequency synthesizer at each station. If the stations are in relative motion along the line of sight then the passband for one station will be Doppler shifted relative to the other. It is necessary to keep the Doppler shift significantly smaller than the bandwidth of the channel, or the correlation between stations will be lost. The Doppler shift is:

$$\Delta\nu = \frac{v}{c} \nu_0$$

where  $\nu_0$  is the nominal observing frequency and  $v$  is the relative line of sight velocity. The Mark III system has six allowable bandwidths,  $B = 4, 2, 1, 0.5, 0.25, 0.125$  MHz, of which 2 MHz is the most commonly used. The band shifts by

$$\Delta\nu = \frac{v}{c} \cdot \frac{c}{\lambda_0}$$

so that

$$\Delta\nu_{\max} \text{ (in MHz)} = 0.8/\lambda \text{ (in cm)}$$

Thus at 18 cm there is clearly no problem as  $\Delta\nu_{\max}$  is only .04 MHz, much smaller than the available bandwidths. At 1 cm, however,  $\Delta\nu_{\max} \sim .8$  MHz, and no longer negligible compared to the largest available bandwidth. This effect could be reduced by varying the local oscillators of the orbital station in order to match a nominal RF passband. This would require somewhat more complicated hardware in the orbital video converters and increase the analysis complexity slightly. It must be emphasized that the sensitivity loss caused by this effect can not be recovered in the post-processing stage, although it could be calibrated out.

#### F. Correlator Parameters/Restrictions

The basic parameters which must be supplied to the correlator hardware are the geometric delay ( $\tau_g$ ), delay rate ( $\dot{\tau}_g$ ), fringe rate ( $\dot{\phi}$ ) and fringe acceleration ( $\ddot{\phi}$ ). Various hardware limitations in the correlator will place restrictions or requirements on each of these quantities.

Delay. The nominal delay time must be provided to the correlator so the two data streams can be aligned within  $1/B$  in order to retain coherence. The complex correlation is computed for 8 lags so the nominal delay must be accurate within  $\pm 4$  data samples. One lag corresponds to the data sample interval,  $\tau_s = 1/2B$ , where  $B$  is the bandwidth, so the required delay accuracy is  $\pm 4/2B = \pm 1.0 \mu\text{s}(2\text{MHz}/B)$ . The uncertainty in delay,  $\Delta\tau$  is entirely due to the uncertainties in the parallel baseline component,  $\Delta\ell_{\parallel}$ , so that  $\Delta\tau = \Delta\ell_{\parallel} / c$ , and the

baseline must be known to an accuracy of

$$\Delta \rho_{\parallel} \lesssim 300 \text{ (2MHz/B) meters.}$$

Since the locations of the ground stations are well determined, this requirement translates into a requirement on knowledge of the absolute spacecraft location. This requirement is independent of observing frequency and the nature of the spacecraft orbit (high or low Earth).

This degree of accuracy should provide no serious difficulty. Spacecraft in high orbits will suffer relatively small disturbance forces and their orbits should be easy to determine. For spacecraft in low earth orbit, use of STDN or TDRSS tracking will be nearly sufficient. The projected errors for STDN and Spacelab are at just the required level. Those for TDRSS and Spacelab are a factor of 2 too large. At worst this might require an extra pass through the data. Once fringes have been found, use of the VLBI system itself with bright calibration sources will determine the orbit extremely accurately.

Delay Rate. As the distance between stations changes the delay must be adjusted by the correlator. The adjustment can only be made in units of single data intervals,  $\tau_s$ . A total of 15 adjustments to the delay  $\pm 1$  sample interval each can be made during a correlator parameter period. This is a restriction imposed by the correlator hardware. The delay rate is proportional to the relative line of sight velocity,

$$\dot{\tau}_g = \frac{d}{dt} \left( \frac{\rho_{\parallel}}{c} \right) = \frac{v_{\parallel}}{c}.$$

The time,  $\tau_u$ , for the delay to change by one sample,  $\tau_s$ , is

$$\tau_u = \frac{\tau_s}{\dot{\tau}_g} = \frac{c}{2Bv_{\parallel}}.$$

Since 15 updates plus the initial value are allowed, the update interval  $\tau_u$  is 1/16 of a parameter period,  $\tau_{pp}$ , so that the parameter period must satisfy

$$\tau_{pp} \lesssim \frac{8c}{Bv_{||}} = 0.15 \left( \frac{2\text{MHz}}{B} \right) \left( \frac{8\text{km/s}}{v_{||}} \right) \text{ sec.}$$

The parameter period is normally chosen as large as possible, 2s, in the processing of standard VLBI data. The primary effect of using a shorter value is to increase the number of parameter periods contained in an observation. Since there are a fixed number of output words per parameter period, this implies that the required disk storage space will increase. The worst case is for  $v_{\text{max}}$ , which yields a factor of 13 increased storage. This should not be a significant problem since the amount of disk space available to the host computer could easily be expanded to more than the ~1 M byte currently available.

A second effect of the shorter parameter period is that the host computer must service each correlator module more frequently. The rate at which the servicing can be done will depend to some extent on the degree of difficulty of the computations used to derive the various model parameters. This could require restructuring the system to process less than the full number of tracks simultaneously. Because of possible restrictions in the data rate from an orbital station, it is not clear how many channels a space system might have, so this may or may not prove to be a concern.

Fringe Rate. The fringe rate must be supplied by the host computer to each correlator module. In order for the fringe search routines to find fringes in longer segments of data, the total phase rotation between the model and actual data must be a small fraction  $\epsilon$  of a rotation over a parameter period. Since the fringe rate is related to the delay rate by

$$\dot{\phi} = \tau_g v_o = \frac{v_{||}}{\lambda} = \frac{8 \times 10^5}{\lambda(\text{cm})} \left( \frac{v_{||}}{8 \text{ km/s}} \right) \text{ Hz},$$

the requirement of small phase rotation over a parameter period,

$$\delta\phi \approx \int_0^{\tau_{pp}} \dot{\phi} dt \approx \frac{\Delta v_{||}}{\lambda} \tau_{pp} \leq \epsilon,$$

means that the difference between true and model parallel velocities must satisfy

$$\Delta v_{||} \leq \epsilon \frac{\lambda}{\tau_{pp}}$$

At 18 cm and  $\tau_{pp} = .15$ , a nominal value of  $\epsilon = 0.5$  requires knowledge of the spacecraft velocity to within  $\sim 6$  m/s. This requirement can be easily met by TDRSS, but misses by about a factor of 2 for STDN. Again, it should not be difficult to obtain the orbit to this precision. In particular, for bright calibration sources, it will be easy to measure fringe rates to better than 10 mHz, which corresponds to  $v \sim 0.2$  cm/s if  $\lambda = 18$  cm and 0.01 cm/s if  $\lambda = 1$  cm. This should result in extremely good orbit determinations.

The maximum fringe rate achievable in the correlator is the recording bandwidth divided by  $K$ , a software-detectable parameter satisfying  $K = 16, 8, 4, 2, 1$  only, or

$$|\dot{\phi}_{\text{correlator}}| \leq 2 \times 10^6 / K \quad \text{Hz}.$$

Thus for the maximum near-Earth fringe rate K must be chosen to satisfy

$$K < 2.5 \lambda_{\text{cm}} (B/2\text{MHz}),$$

so for a 2 MHz recording bandwidth K must be chosen according to:

$\lambda > 6.4\text{cm}$	$\rightarrow$	$K = 16$
$6.4\text{cm} > \lambda > 3.2\text{cm}$		$K = 8$
$3.2\text{cm} > \lambda > 1.6\text{cm}$		$K = 4$
$1.6\text{cm} > \lambda > 0.8\text{cm}$		$K = 2$
$0.8\text{cm} > \lambda > 0.4\text{cm}$		$K = 1$
$0.4\text{cm} > \lambda > 0$	$\rightarrow$	not possible.

The fringe-rate resolution of the correlator is

$$\delta\phi = \frac{\text{sample rate}}{2^{24} K} = \frac{0.238}{K} \left(\frac{B}{2\text{MHz}}\right) \text{ millihertz,}$$

so that the largest possible value of K should be chosen.

Fringe Acceleration. The fringe rate will not be constant; there is a fringe acceleration of

$$\ddot{\phi} \text{ (Hz/s)} = \frac{v_{\parallel}}{\lambda} = \frac{v^2/a}{\lambda} = 990 \left( \frac{92 \text{ min}}{T} \right)^{2/3} \frac{1}{\lambda \text{ (cm)}}$$

In the absence of a fringe acceleration correction a phase error of

$$\frac{1}{2} \ddot{\phi} \tau_{pp}^2 = \frac{11.1}{\lambda \text{ (cm)}} \left( \frac{\tau_{pp}}{0.05 \text{ s}} \right)^2 \text{ rotations}$$

will occur by the end of one parameter period. This amount is intolerable for most VLBI wavelengths. However, the Mark III system has provision for fringe acceleration correction made by the correlator hardware. The fringe phase  $\phi$  is updated every K data samples by an amount  $\Delta\phi$ , which is a 24 bit word that can be between  $2^{-1}$  and  $2^{-23}$  rotations and at either sign. This phase update itself can be updated every L data bytes (8L data samples) by incrementing or decrementing the least significant bit by one. Here L is only integer between zero and one-eighth of the number of data samples in a parameter period. The least significant bit in  $\Delta\phi$  is  $2^{-23}$  rotations, so the fringe acceleration mode is

$$\ddot{\phi}_{\text{correlator}} = \frac{\pm 2^{-23} \text{ rotations}}{(\text{time for K samples}) (\text{time for 8L samples})}$$

or

$$|\ddot{\phi}_{\text{correlator}}| = \frac{2.38 \times 10^5 \text{ Hz/s}}{K L} \left( \frac{f_s}{4\text{MHz}} \right)^2,$$

where  $f_s$  = data sample rate = 2 x bandwidth of one track. Combining this with the required fringe accelerator for near-Earth space VLBI results in a requirement on K and L:

$$K L = 241. \lambda \text{ (cm)} \left( \frac{f_s}{4\text{MHz}} \right)^2$$

Once K is picked to satisfy the size of the fringe rate for a given  $\lambda$  and  $f_s$ , L follows from this equation. For example, at  $\lambda 7.8$  cm; where  $K = 4$  is the best choice, we require that the phase update  $\Delta\phi$  be updated every  $L = 169$  bytes, or a total of 443 times in a 0.15s parameter period. This is easily accomplished by the current Mark III system.

Quantization of the phase update  $\Delta\phi$  and of its update leads to an accumulated phase error over a parameter period. This may be estimated by comparing the quantized "stair-step" approximation to the phase update to the true required phase changes. The absolute level of the stair-step approximation is certainly accurate to within  $\frac{1}{2}$  of the update quantization, i.e., to within  $2^{-24}$  rotations. The slope of the stair-step is accurate to within one step per parameter period. Thus the  $i^{\text{th}}$  update (at time  $t$ ) is in error by no more than

$$2^{-24} + 2^{-23} \frac{t}{\tau_{pp}} = 2^{-24} + \left( \frac{2^{-23}}{\tau_{pp}} \right) i$$

Since this error is added to  $\phi$  every K data intervals, or  $\left( \frac{\tau_{pp} f_s}{K} \right)$  times in a parameter period, the phase error accumulated by the end of the period is  $(f_s \tau_{pp}/K)$

$$\begin{aligned} \sum_{i=1}^{\tau_{pp} f_s / K} \left[ 2^{-24} + \left( \frac{2^{-23} f_s K}{\tau_{pp}} \right) i \right] &= 2^{-24} \left( \frac{\tau_{pp} f_s}{K} \right) + 2^{-23} \left( \frac{f_s K}{\tau_{pp}} \right) \frac{1}{2} \left( \frac{f_s \tau_{pp}}{K} \right)^2 \\ &= 2^{-23} (f_s \tau_{pp}/K) \text{ rotations.} \end{aligned}$$

Inserting numerical values yields a phase error or

$$7.15 \times 10^{-2} \left( \frac{\tau_{PP}}{0.15_s} \right) \left( \frac{f_s}{4\text{MHz}} \right) \frac{1}{K} \text{ rotations.}$$

Even for the minimum value of  $K = 1$  this does not present a problem.